

ABSTRACT

JADOO, NISHITA. Extended Body Motion in General Relativity. (Under the direction of J. David Brown).

In this thesis, we present a numerical framework for modeling solid extended bodies using elasticity theory in general relativity. We assume that the metric is not affected by the stress-energy-momentum tensor of the extended body. The numerical method described can be used to model solid bodies of any shape, for any hyperelastic potential energy model and any spacetime metric. We also describe a method using Fermi frames to extract information from the simulations. We use the framework developed to model the motion of a $0.1 M$ radius hyperelastic sphere in close encounter orbits around a Schwarzschild black hole. We compute the deviation of the center of mass from a geodesic that starts with the same initial conditions as the center of mass and the increase in the spin of the body. We analyse the conserved total energy and angular momentum by splitting them into parts. We obtain detailed information on the normal modes excited in the sphere.

© Copyright 2023 by Nishita Jadoo

All Rights Reserved

Extended Body Motion in General Relativity

by
Nishita Jadoo

A dissertation submitted to the Graduate Faculty of
North Carolina State University
in partial fulfillment of the
requirements for the Degree of
Doctor of Philosophy

Physics

Raleigh, North Carolina
2023

APPROVED BY:

Charles R. Evans

Zhilin Li

James Kneller

J. David Brown
Chair of Advisory Committee

DEDICATION

To my parents.

BIOGRAPHY

Nishita Jadoo was born in Mauritius. She studied for a bachelor degree in physics at the University of Mauritius. She worked for some time as a software developer before travelling to the US to pursue graduate physics education at the University of Georgia, then at the North Carolina State University.

ACKNOWLEDGEMENTS

I am indebted to my advisor Dr. J. David Brown for his excellent guidance and for the project on extended body motion in general relativity. I would like to thank him for his understanding of general relativity, patience and for his insightful teaching of the general relativity course.

I would like to thank Dr Charles R. Evans for his many contributions and helpful explanations. I would like to thank Dr Zhilin Li for his teaching of finite element methods which has been invaluable. I would like to thank Dr James Kneller for teaching astrophysics. I would like to thank the committee members for their support for postdoctoral applications.

I would like to thank Dr Lisa L. Lowe for her suggestions for writing Fortran code and using Linux and MPI. I would like to thank XSEDE for the workshop on high performance computing. I would like to acknowledge the computing resources provided by North Carolina State University High Performance Computing Services Core Facility.

I would like to thank Rhonda Bennett for her kindness and invaluable help. I would like to thank Dr David Aspnes for his excellent teaching of electromagnetic theory. I would like to thank the physics department at North Carolina State University for supporting me as a graduate student. I would like to thank group members for sharing their research updates and friends in the physics department at North Carolina State University.

I would like to thank Dr M. Howard Lee who taught statistical mechanics at the University of Georgia for his kindness as well as his understanding of statistical mechanics. I would like to thank professors in the physics department at the University of Mauritius, including Dr Shailendra Oree, Dr Mono Runjun Bunwaree and Dr Kis-sion King.

I owe many thanks to my parents for their unconditional love and support.

TABLE OF CONTENTS

List of Figures	vii
Chapter 1 Introduction	1
Chapter 2 Nonrelativistic elasticity theory	4
2.1 Overview	4
2.2 Configuration and deformation gradient	5
2.3 Mass conservation, Newton's 2 nd law and stress tensors	5
2.3.1 Mass conservation	6
2.3.2 Newton's 2 nd law	6
2.3.3 Stress tensors	7
2.4 Hyperelastic energy models	7
2.5 Linear elasticity	9
2.5.1 Dynamical solution for normal modes of a sphere	11
2.5.2 Static solution for a sphere under tidal forces	16
Chapter 3 General relativistic elasticity theory	17
3.1 Overview	17
3.2 Worldtube, radar metric	18
3.3 Action	19
3.4 Gauge invariance of the action	20
3.5 Stress–energy–momentum tensor	23
Chapter 4 Numerical method	26
4.1 Overview	26
4.2 Matter space discretization	27
4.3 Semi-discretized action	27
4.4 Code validation	32
Chapter 5 Fermi frames	37
5.1 Overview	37
5.2 Numerical evaluation of Fermi coordinates and velocities	38
5.2.1 Choosing the fiducial node	39
5.2.2 Choosing the initial spacelike legs of the tetrads	39
5.2.3 Fermi-Walker transport of the spatial legs of the tetrads	40
5.2.4 Computing Fermi coordinates from spacetime coordinates on discrete $t = \text{const}$ time slices	40
5.2.5 Fermi four-velocity of the nodes	42
5.3 Center of mass and spin	43
5.3.1 Flat spacetime	43
5.3.2 Curved spacetime	44

5.3.3	Road map for finding the deviation of the center of mass in the geodesic Fermi frame	45
Chapter 6	Conservation laws	47
6.1	Overview	47
6.2	Rest energy	48
6.3	Spacetime with symmetry	49
6.3.1	Conservation of energy	49
6.3.2	Conservation of angular momentum	52
Chapter 7	Motion of a hyperelastic sphere in Schwarzschild spacetime	54
7.1	Overview	54
7.2	Initial data	56
7.3	Deformation of sphere as seen in the Fermi frame	57
7.4	Deviation of the center of mass	58
7.5	Energy	58
7.6	Angular momentum	64
7.7	Decomposition into normal modes	69
7.7.1	$n = 0, \ell = 0$ and $n = 0, \ell = 2, m = [0, \pm 2]$	70
7.7.2	$n = 1, \ell = 0$ and $n = 1, \ell = 2, m = [0, \pm 2]$	72
7.7.3	$\tilde{R}_p = [9.5, 10, 10.5]$	73
Chapter 8	Conclusions	76
8.1	Summary	76
8.2	Future work	77
References	78

LIST OF FIGURES

Figure 2.1	The radial dependence of $f_{n\ell}(r)$ and $g_{n\ell}(r)$ for $\ell = 2$ and different values of n . The surface of the sphere is at $r = 0.1$	15
Figure 3.1	$X^\mu(\lambda, \zeta)$ maps a material point with coordinates ζ^i in \mathcal{S} and a real parameter λ to the spacetime event x^μ inside the world tube in four-dimensional spacetime, \mathcal{M}	19
Figure 4.1	Here we are depicting a two-dimensional triangular mesh instead of a tetrahedral mesh for clarity. This figure shows node labels, $n = \{1, 2, \dots, 10\}$ and element labels $E = \{1, 2, \dots, 11\}$ (boxed). The set of nodes in element, $E = 4$, is $\mathcal{N}(4) = \{4, 5, 8\}$. The ring of node, $n = 5$, is $\mathcal{R}(5) = \{3, 4, 6, 7, 8, 9\}$	28
Figure 4.2	A general tetrahedral element \mathcal{S}_E is transformed into a unit trirectangular tetrahedron \mathcal{T}	29
Figure 4.3	Analytical and numerical displacements and velocities for a node as a function of time for $h_{\max} = a/8$	34
Figure 4.4	Analytical and numerical displacements and velocities for a node as a function of time for $h_{\max} = a/16$	35
Figure 4.5	Convergence of the algorithm measured in terms of the L2-norm of the error in the coordinates and velocities.	36
Figure 5.1	$t = \text{const}$ slices. Geodesic at \mathcal{P} orthogonal to the observer's worldline crosses the generic nodes's worldline at \mathcal{Q}	41
Figure 5.2	The worldline of the center of mass. The event \bar{x}_ϕ^μ does not lie on the $\bar{t} = \text{const}$ slice.	43
Figure 7.1	Schwarzschild coordinates of the center of mass of the hyperelastic sphere for $\tilde{R}_p = [9.5, 10, 10.5]$. The orbits are anticlockwise in the equatorial plane.	55
Figure 7.2	Worldline of point C which is a geodesic and of two generic nodes, Fermi $\bar{t} = \text{const}$ slices and a $t = \text{const}$ slice that crosses the worldline of the generic nodes.	57
Figure 7.3	Points along the orbit at which the spatial Fermi coordinates of the sphere are plotted. The Fermi frame directions are also shown.	59
Figure 7.4	Top view in the Fermi frame. (1) to (6) correspond to successive points marked along the orbit. (2) to (5) are at constant intervals of t . The period of $n = 0, \ell = 2$ analytical normal modes is $41.2M$. Between (5) and (6), the sphere undergoes about 12 oscillations. The arrow shows the direction to the black hole.	59
Figure 7.5	Angle of two nodes in the fiducial Fermi frame for the $\tilde{R}_p = 9.5$ orbit.	60

Figure 7.6	Deflection of the center of mass in the \bar{x}^1 and \bar{x}^2 directions in the geodesic Fermi frame for $\tilde{R}_p = [9.5, 10, 10.5]$	61
Figure 7.7	The rest energy, E_{rest} , is conserved to 9 orders of magnitude close to periastron and 13 orders of magnitude far from the black hole for $\tilde{R}_p = 9.5$ and for the mesh refinement $h_{\text{max}} = a/16$	62
Figure 7.8	The total energy, E_{tot} , (using Equation 6.12), is conserved to 9 orders of magnitude at the end of the simulation. This shows the result for $\tilde{R}_p = 9.5$ and for the mesh refinement $h_{\text{max}} = a/16$	62
Figure 7.9	The fractional change in the theoretically conserved total energy, E_{tot} , from initial time for three different mesh refinements. This is a plot zoom to focus on the behaviour away from periastron.	63
Figure 7.10	The fractional change in the theoretically conserved energy, $E_{\text{tot}} - E_{\text{rest}}$, from initial time for $h_{\text{max}} = a/16$	63
Figure 7.11	Separation of the conserved energy, $E_{\text{tot}} - E_{\text{rest}}$, into three parts for the $\tilde{R}_p = 9.5$ orbit.	64
Figure 7.12	First way of computing the orbital energies of the elastic sphere as $\sum(T_{\text{orb}} + U_{\text{orb}})$ and subtracting $\sum(T_{\text{orb}} + U_{\text{orb}})$ from $\sum(T_{\text{orb}} + T_{\text{int}} + U_{\text{orb}})$ to obtain the internal kinetic energy. The plot shows the results for $\tilde{R}_p = 9.5$	65
Figure 7.13	Second way of computing the orbital energies of the elastic sphere as $\sum(T_{\text{cm}} + U_{\text{cm}})$ and subtracting $\sum(T_{\text{cm}} + U_{\text{cm}})$ from $\sum(T_{\text{orb}} + T_{\text{int}} + U_{\text{orb}})$ to obtain the internal kinetic energy. The plot shows the results for $\tilde{R}_p = 9.5$	65
Figure 7.14	Third way of computing the orbital energies of the elastic sphere as $\sum(T_p + U_p)$ and subtracting $\sum(T_p + U_p)$ from $\sum(T_{\text{orb}} + T_{\text{int}} + U_{\text{orb}})$ to obtain the internal kinetic energy. The plot shows the results for $\tilde{R}_p = 9.5$	66
Figure 7.15	The total angular momentum J_{tot} (using Equation 6.26) computed in the center of mass Fermi frame is conserved to 7 orders of magnitude. This shows the result for the $\tilde{R}_p = 9.5$ orbit and for the mesh refinement $h_{\text{max}} = a/16$	67
Figure 7.16	The fractional change in the total angular momentum, J_{tot} , from initial time for three different mesh refinements. This is a plot zoom to focus on the behaviour away from periastron.	68
Figure 7.17	Parts of the conserved angular momentum computed in the center of mass Fermi frame for the $\tilde{R}_p = 9.5$ orbit. For J_{orbit} , we plot the change from the initial value.	69
Figure 7.18	Decomposition coefficient as a function of proper time of the fiducial node, $\tilde{R}_p = 9.5$, $n = 0, \ell = 0$ and $n = 0, \ell = 2, m = [0, \pm 2]$	71
Figure 7.19	Decomposition coefficient as a function of proper time of the fiducial node, $\tilde{R}_p = 9.5$, $n = 1, \ell = 0$ and $n = 1, \ell = 2, m = [0, \pm 2]$	72
Figure 7.20	Decomposition coefficient for $n = 0, \ell = 2, m = -2$ as a function of proper time of the fiducial node for the three orbits, $\tilde{R}_p = [9.5, 10, 10.5]$	73

Figure 7.21 Decomposition coefficient for $n = 1, \ell = 2, m = -2$ as a function of proper time of the fiducial node for the three orbits, $\tilde{R}_p = [9.5, 10, 10.5]$. 74

Figure 7.22 Decomposition coefficient for $n = 0, \ell = 3, m = -3$ as a function of proper time of the fiducial node for $\tilde{R}_p = [9.5, 10, 10.5]$ 75

CHAPTER

1

INTRODUCTION

The problem of motion in general relativity has a long history. Einstein was interested in whether the laws of motion of material points can be derived from the vacuum Einstein field equations. Einstein and Grommer (1927) showed that if a point particle is treated as a singularity in spacetime, it follows a geodesic. This only gives the motion of point particles and not extended bodies. The first paper to describe an extended body in general relativity is Mathisson (1937). Mathisson defines a multipole expansion of the body using the body's stress-energy-momentum (SEM) tensor with the single pole defining the mass and the dipole and quadrupole defining the "rotation moment". Subsequently, many others have worked on this problem following a similar method, including Papapetrou (1951) who gives the equations of motion of spinning particles to dipole order, Pirani (1956), Tulczyjew (1959) and Madore (1969). The works differ in the way they define the multipole moments. A series of papers (Dixon and Bondi (1970), Dixon and Hewish (1970) and Dixon and Hewish (1974)) provide a more thorough definition of the multipole moments. The equations describing the motion of pole-dipole particles are commonly known as the Mathisson-Papapetrou-Dixon (MPD) equations. In general, the analysis leaves the equation of motion of the quadrupole moment unspecified.

Even in the pole-dipole case, additional equations to define the center of mass are

needed called spin supplementary conditions to have a complete system of equations. Several different spin supplementary conditions have been proposed which lead to different worldlines for the representative point on the body, however for the pole-dipole they are shown to lie within the minimal worldtube (Kyrian and Semerák (2007)). Kyrian and Semerák (2007) give a list of known spin supplementary conditions and what they imply for conserved quantities for the pole-dipole particle. Costa and Natário (2015) give an in-depth discussion of different spin supplementary conditions.

In this thesis, we consider extended bodies in general relativity as elastic bodies. This is closer to physical reality than, for example, rigid bodies. There is difficulty in defining a rigid body in curved spacetime. If a rigid body is defined as one that has zero deformation, it would be unphysical because it would imply the speed of sound to be greater than the speed of light. Also, stresses generated in the body might be important and contribute to the SEM tensor. In general, it is perhaps simpler to treat extended bodies as elastic. If one wants to model stiff bodies, then the material properties of the body could be set so that the speed of sound is close to the speed of light.

Furthermore, the deformation of extended bodies in general relativity is an important aspect to be modeled. The quadrupole deformation of the neutron stars in binary inspirals can be detected from the observed gravitational waves (Abbott et al. (2017), De et al. (2018)) and provides crucial insight into the nuclear equation of state of these objects. The deformation and other internal structure of small bodies in extreme mass ratio inspirals will have an effect on the gravitational waves emitted (Steinhoff and Puetzfeld (2012)) which the planned space interferometer LISA will be able to detect. The spin of the small body is expected to have a next-to-leading order effect in the phase of these gravitational waves (Witzany et al. (2019)). Except for specific cases, the deformation cannot be modeled accurately as proportional to the tidal field. For example, the small body could be spinning faster than it takes to respond to tidal forces.

Astrophysical compact objects are usually modeled as fluids in general relativistic settings. However, it is known that neutron star crusts are solid (Chamel and Haensel (2008)). A class of astrophysical objects known as ultra-massive white dwarfs have up to ninety-nine per cent crystallized mass (Camisassa, María E. et al. (2019)). As a natural alternative to fluids, elasticity can be used in such cases which allows for shear stresses. Alho et al. (2022) used general relativistic elasticity to study spherically symmetric elastic stars and proposed that elasticity might be an important factor for modeling exotic compact objects.

Numerical works on general relativistic elasticity are not as abundant as numerical

works on general relativistic hydrodynamics. One such work is by Gundlach et al. (2011) who propose an Eulerian formulation of general relativistic elasticity that can be used for numerical modeling and can capture shocks. They test their framework on Riemann problems in Minkowski spacetime. Other works include a set of papers (Karlovini and Samuelsson (2003), Karlovini et al. (2004), Karlovini and Samuelsson (2004), Karlovini and Samuelsson (2007)) that propose a coherent framework for accurately modeling the solid crust within neutron stars.

In this thesis, we are interested in accurately modeling an extended body in general relativity. We want to obtain both its orbit and changes to internal structure including deformation and spin. As a first step, for this work we assume that the extended body's SEM tensor does not affect the spacetime curvature. In other words, we ignore self-gravity.

We start by reviewing nonrelativistic elasticity in Chapter 2. We then describe general relativistic elasticity as formulated by Brown (2021), which is the theory we use for modeling an extended body, in Chapter 3. We explain the numerical method used in Chapter 4. We detail how we construct Fermi frames and compute an approximate center of mass in Chapter 5. We look at the conservation of rest energy and of total energy and angular momentum for spacetimes with symmetries in Chapter 6. We present the results of the simulation of a hyperelastic sphere in close encounter orbits around a Schwarzschild black hole in Chapter 7. We summarize the work in this thesis and specify future work in Chapter 8.

CHAPTER

2

NONRELATIVISTIC ELASTICITY THEORY

In this chapter we give a brief review of elasticity theory in the nonrelativistic domain. In this chapter, we assume that the physical space (defined shortly) is three-dimensional flat space. Except when specified, we will assume general curvilinear coordinates and for example lower the index on a vector using the metric.

2.1 Overview

Elasticity theory is the study of deformable bodies under stresses and has a long history and many applications. Love (1892) gives a detailed account of the history of elasticity. An important historical development in elasticity theory was the formulation of finite element methods to specifically solve problems in elasticity. In this thesis we make use of the exact solution for a sphere in static equilibrium under tidal forces found in Love (1892) for obtaining initial data and Lamb's early work on the vibrations of an elastic sphere (Lamb (1881)) to decompose the deformation of a sphere into normal modes. We also make use of the techniques from finite element methods for spatial discretization.

We will start by giving definitions and theorems in nonlinear elasticity, however we will

not go into the details of the proofs of these theorems which can be found in Marsden and Hughes (1994). Proof of various theorems in elasticity have been worked out assuming the physical space is three-dimensional flat space and using Cartesian coordinates. For general Riemannian manifolds, it is assumed that the theorems are still valid since they refer to a small portion of the space which locally looks flat (Frankel (2011)).

We will then describe linear elasticity. A large body of works make use of linear elasticity for which exact solutions are known in some cases. We will look at exact solutions for solid isotropic homogeneous elastic spheres.

2.2 Configuration and deformation gradient

The “matter space”, \mathcal{S} , is defined as the three-dimensional space of material points with coordinates ζ^i , for $i = 1, 2, 3$. A configuration (also sometimes referred to as a deformation), X^a , where $a = 1, 2, 3$, is a map from \mathcal{S} and for dynamical problems a parameter t to three-dimensional physical space, \mathcal{M} . The coordinates on \mathcal{M} are denoted by x^a for $a = 1, 2, 3$ and the metric on \mathcal{M} is g_{ab} . The “reference configuration” is the map X_R^a from \mathcal{S} to the three-dimensional space \mathcal{M} in which the body is in a relaxed state. Let overdot mean $\partial/\partial t$ and “ $_{,i}$ ” mean $\partial/\partial \zeta^i$. The relaxed metric, $\epsilon_{ij} = X_{R,i}^a g_{ab} X_{R,i}^b$, gives distances between material points when the body is in relaxed state. The deformation gradient is defined as

$$F_{ai} = g_{ab} X_{,i}^b \quad (2.1)$$

The right Cauchy-Green deformation tensor represents the amount of strain in the deformed body and is defined by

$$f_{ij} = X_{,i}^a g_{ab} X_{,j}^b \quad (2.2)$$

2.3 Mass conservation, Newton’s 2nd law and stress tensors

For a continuous body, we look at mass conservation and Newton’s 2nd law for a small piece of the body which leads to the definition of the Cauchy stress tensor. Let \mathcal{S}_E be an open set of \mathcal{S} and let $X^a(\zeta, t)$ be the map from \mathcal{S}_E and a real parameter t to \mathcal{M}_E .

2.3.1 Mass conservation

Let $\rho_0(\zeta)$ be the mass density per unit volume of \mathcal{S} when the body is relaxed in physical space and let $\rho(x, t)$ be the mass density per unit volume of \mathcal{M} of the deformed body at some time t . Since mass is conserved,

$$\int_{\mathcal{S}_E} d^3\zeta \sqrt{\epsilon} \rho_0(\zeta) = \int_{\mathcal{M}_E} d^3x \sqrt{h} \rho(x, t) \quad (2.3)$$

$$= \int_{\mathcal{S}_E} d^3\zeta |\det(X_{,i}^a)| \sqrt{h} \rho(x, t) \quad (2.4)$$

where $\epsilon = \det(\epsilon_{ij})$, $h = \det(g_{ab})$ and $|\det(X_{,i}^a)|$ is the Jacobian of the transformation between x^a and ζ^i . Since \mathcal{S}_E is arbitrary, this leads to $|\det(X_{,i}^a)| (\sqrt{h}/\sqrt{\epsilon}) \rho = \rho_0$. The factor $|\det(X_{,i}^a)|$ can be analysed as in Brown (2021). Eq. (2.2) is

$$f_{ij} = X_{,i}^a g_{ab} X_{,j}^b. \quad (2.5)$$

Taking determinant on both sides,

$$\begin{aligned} f &= \det(X_{,i}^a) h \det(X_{,j}^b) \\ \det(X_{,i}^a) &= \frac{\sqrt{f}}{\sqrt{h}} \end{aligned} \quad (2.6)$$

Therefore, $J\rho = \rho_0$ where

$$J = \sqrt{f}/\sqrt{\epsilon} \quad (2.7)$$

is the ratio of the deformed volume element to the undeformed volume element. The mass current is

$$\rho \dot{X}^a \equiv (\rho_0/J) \dot{X}^a. \quad (2.8)$$

2.3.2 Newton's 2nd law

We apply Newton's 2nd law to a small piece of the body in three-dimensional flat physical space. The elastic body may be subject to applied body forces such as gravity which acts on volume elements, applied surface forces on area elements on the boundary also referred to as traction and it additionally has internal surface forces on area elements on any surface

due to internal stresses. Applying Newton's 2nd law for \mathcal{M}_E :

$$\frac{d}{dt} \int_{\mathcal{M}_E} d^3x \sqrt{h} \rho \dot{X}^a = \int_{\partial \mathcal{M}_E} d^2x \sqrt{\sigma} t^a(x^b, t, n^b) + \int_{\mathcal{M}_E} d^3x \sqrt{h} \rho b^a \quad (2.9)$$

where $d^2x \sqrt{\sigma}$ is the surface element on $\partial \mathcal{M}_E$, $t^a(x^b, t, n^b)$ is the force per unit deformed area at position x^b and time t across a surface element with unit normal n^b from the material surrounding it and b^a is a body force acting per unit mass.

2.3.3 Stress tensors

According to Cauchy's theorem (Marsden and Hughes (1994)), if Eq. (2.9) holds, then t^a depends linearly on n^b and there is a tensor, σ^{ab} , called the Cauchy stress tensor such that $t^a = \sigma^{ab} g_{bc} n^c$. σ^{ab} is the force per unit of deformed area acting across a surface element in the deformed body with unit normal n_a . The Cauchy stress tensor can be obtained from the second Piola stress tensor, S^{ij} (defined later), which represents the force in the undeformed body per unit undeformed area across surface elements using Brown (2021):

$$\sigma^{ab} = \frac{1}{J} X_{,i}^a S^{ij} X_{,j}^b \quad (2.10)$$

where $J = \sqrt{f}/\sqrt{\epsilon}$ and $f = \det(f_{ij})$ and $\epsilon = \det(\epsilon_{ij})$. The first Piola stress tensor is obtained from the second Piola stress tensor by

$$P_a^i = g_{ab} X_{,j}^b S^{ij}. \quad (2.11)$$

2.4 Hyperelastic energy models

Elastic materials are materials for which the stress can be written in terms of the strain at a particular time. Hyperelastic materials are materials for which the work done by stresses during the deformation process depends only on the initial and final configurations. Homogeneous materials are materials for which portions of the elastic material have the same mechanical behaviour. Isotropic materials are materials for which the potential energy function, W , only depends on the deformation gradient only through f_{ij} and ϵ_{ij} . Lagrangian strain E_{ij} given by

$$E_{ij} = (f_{ij} - \epsilon_{ij})/2. \quad (2.12)$$

The second Piola stress tensor is given by $S^{ij} = \partial W / \partial E_{ij}$.

Examples of different energy models for isotropic hyperelastic materials include the Saint Venant-Kirchhoff, the Mooney-Rivlin, the neo-Hookean and the Ogden models. In the Saint Venant-Kirchhoff model, the potential energy function is obtained from Lagrangian strain by

$$W(E) = \frac{\lambda}{2} (\epsilon^{ij} E_{ij})^2 + \mu (\epsilon^{ik} \epsilon^{jl} E_{ij} E_{kl}) \quad (2.13)$$

where ϵ^{ij} is the inverse of ϵ_{ij} and λ and μ are the Lamé constants. The bulk modulus, $K = \lambda + 2\mu/3$, measures resistance to volume changes. For the Saint Venant-Kirchhoff model, the second Piola stress tensor is

$$S^{ij} = \lambda (\epsilon^{kl} E_{kl}) \epsilon^{ij} + 2\mu \epsilon^{ik} \epsilon^{jl} E_{kl}. \quad (2.14)$$

It is often mentioned in literature that the Saint Venant-Kirchhoff model is not valid for large strains in which case the model softens under compression.

Invariants of a tensor are scalar functions of the tensor components which do not change under a change of coordinates. In literature, hyperelastic isotropic models are often described in terms of the invariants of $\epsilon^{ik} f_{kj}$ called the stress invariants, I_1 , I_2 and I_3 or the square root of the eigenvalues of $\epsilon^{ik} f_{kj}$ called the principle stretches λ_1 , λ_2 and λ_3 . The stress invariants are

$$I_1 \equiv \epsilon^{ij} f_{ij} \quad (2.15)$$

$$I_2 \equiv \frac{1}{2} [(\epsilon^{ij} f_{ij})^2 - \epsilon^{ik} \epsilon^{jl} f_{ij} f_{kl}] \quad (2.16)$$

$$I_3 \equiv \det(\epsilon^{ik} f_{kj}) = f/\epsilon. \quad (2.17)$$

It should be noted that $I_3 = J^2$. The stress invariants are related to the principle stretches by

$$I_1 = \lambda_1^2 + \lambda_2^2 + \lambda_3^2 \quad (2.18)$$

$$I_2 = \lambda_1^2 \lambda_2^2 + \lambda_2^2 \lambda_3^2 + \lambda_3^2 \lambda_1^2 \quad (2.19)$$

$$I_3 = \lambda_1^2 \lambda_2^2 \lambda_3^2. \quad (2.20)$$

In the Mooney-Rivlin model the, potential energy is given by:

$$W(E) = \frac{\mu_1}{2} (\bar{I}_1 - 3) + \frac{\mu_2}{2} (\bar{I}_2 - 3) + \frac{\kappa}{2} (J - 1)^2. \quad (2.21)$$

where $\bar{I}_1 = I_1/J^{(2/3)}$ and $\bar{I}_2 = I_2/J^{(4/3)}$. In the limit of small deformations, κ is equal to the bulk modulus and $\mu_1 + \mu_2$ is equal to the shear modulus. For $\mu_2 = 0$, the model is known as the neo-Hookean model. In the Ogden model, the potential energy is given by

$$W(E) = \sum_{p=1}^N \frac{\mu_p}{\alpha_p} \left(\lambda_1^{\alpha_p} + \lambda_2^{\alpha_p} + \lambda_3^{\alpha_p} - 3 \right) \quad (2.22)$$

The Ogden model has been developed to model materials such as rubbers, polymers and biological tissue. In all these constitutive models, the material parameters and the validity of the model are determined by fitting to experimental data. A perfect fluid can be considered a special case of an elastic material in which the potential energy is a function of J only (Brown (2021)).

2.5 Linear elasticity

The material in this section is drawn from Brown (nd). Linear elasticity is used when the deformation is the result of small displacements from the reference configuration. Linear elasticity can be obtained from nonlinear elasticity by writing

$$X^a(\zeta, t) = X_R^a(\zeta) + \xi^a(\zeta, t) \quad (2.23)$$

where $\xi^a(\zeta, t)$ is assumed to be small and there is no rotation.

\dot{X}^a and $X_{,i}^a$ are then:

$$\dot{X}^a(\zeta, t) = \dot{\xi}^a(\zeta, t) \quad (2.24)$$

$$X_{,i}^a(\zeta, t) = X_{R,i}^a(\zeta) + \xi_{,i}^a(\zeta, t) \quad (2.25)$$

$\xi_{,i}^a(\zeta, t)$ is also assumed to be small. Assuming flat space and Cartesian coordinates, the right Cauchy-Green deformation and matter space metric are:

$$f_{ij} = X_{,i}^a \delta_{ab} X_{,j}^b = (X_{R,i}^a + \xi_{,i}^a) \delta_{ab} (X_{R,j}^b + \xi_{,j}^b), \quad (2.26)$$

$$\epsilon_{ij} = X_{R,i}^a \delta_{ab} X_{R,j}^b. \quad (2.27)$$

We have the map

$$x^a = X_R^a(\zeta) \quad (2.28)$$

and we define the inverse map that takes the a point in physical space where the body is in the relaxed state to the matter space label:

$$\zeta^i = Z_R^i(x). \quad (2.29)$$

Taking derivatives with respect to ζ , the following useful relations are obtained:

$$X_{R,i}^a Z_{R,a}^j = \delta_i^j, \quad (2.30)$$

$$X_{R,i}^a Z_{R,b}^i = \delta_b^a. \quad (2.31)$$

The following formulas for the inverse metric and metric in the matter space and reference configuration hold:

$$\epsilon^{ij} = Z_{R,a}^i \delta^{ab} Z_{R,b}^j, \quad (2.32)$$

$$\delta^{ab} = X_{R,i}^a \epsilon^{ij} X_{R,j}^b, \quad (2.33)$$

$$\delta_{ab} = Z_{R,a}^i \epsilon_{ij} Z_{R,b}^j. \quad (2.34)$$

We verify that they are correct by computing $\epsilon^{ij} \epsilon_{jk}$ and $\delta^{ab} \delta_{bc}$:

$$\epsilon^{ij} \epsilon_{jk} = Z_{R,a}^i \delta^{ab} Z_{R,b}^j X_{R,c}^k \delta_{cd} X_{R,k}^d \quad (2.35)$$

$$= Z_{R,a}^i \delta^{ab} \delta_b^c \delta_{cd} X_{R,k}^d \quad (2.36)$$

$$= Z_{R,a}^i X_{R,k}^a \quad (2.37)$$

$$= \delta_k^i \quad (2.38)$$

$$\delta^{ab} \delta_{bc} = X_{R,i}^a \epsilon^{ij} X_{R,j}^b Z_{R,b}^k \epsilon_{kl} Z_{R,c}^l \quad (2.39)$$

$$= X_{R,i}^a \epsilon^{ij} \delta_j^k \epsilon_{kl} Z_{R,c}^l \quad (2.40)$$

$$= X_{R,i}^a \epsilon^{ij} \epsilon_{jl} Z_{R,c}^l \quad (2.41)$$

$$= X_{R,i}^a \delta_l^i Z_{R,c}^l \quad (2.42)$$

$$= X_{R,i}^a Z_{R,c}^i \quad (2.43)$$

$$= \delta_c^a \quad (2.44)$$

The potential energy function in the Saint Venant-Kirchhoff, $W(E) = \lambda/2(\epsilon^{ij} E_{ij})^2 + \mu(\epsilon^{ik} \epsilon^{jl} E_{ij} E_{kl})$, is needed to second order in ζ_a^i . We first compute the Lagrangian strain

tensor $E_{ij} = (f_{ij} - \epsilon_{ij})/2$.

$$E_{ij} = \frac{1}{2}[X_{R,i}^a \delta_{ab} X_{R,j}^b + \xi_{,i}^a \delta_{ab} X_{R,j}^b + X_{R,i}^a \delta_{ab} \xi_{,j}^b - X_{R,i}^a \delta_{ab} X_{R,j}^b] + \mathcal{O}^2(\xi_{,i}^a) \quad (2.45)$$

$$= \frac{1}{2}[\xi_{,i}^a \delta_{ab} X_{R,j}^b + X_{R,i}^a \delta_{ab} \xi_{,j}^b] + \mathcal{O}^2(\xi_{,i}^a) \quad (2.46)$$

We also need to compute $\epsilon^{ij} E_{ij}$ and $\epsilon^{ik} \epsilon^{jl} E_{ij} E_{kl}$.

$$\epsilon^{ij} E_{ij} = \frac{1}{2} Z_{R,c}^i \delta^{cd} Z_{R,d}^j [\xi_{,i}^a \delta_{ab} X_{R,j}^b + X_{R,i}^a \delta_{ab} \xi_{,j}^b] + \mathcal{O}^2(\xi_{,i}^a) \quad (2.47)$$

$$= \frac{1}{2} [Z_{R,a}^i \xi_{,i}^a + Z_{R,b}^j \xi_{,j}^b] + \mathcal{O}^2(\xi_{,i}^a) \quad (2.48)$$

$$= Z_{R,a}^i \xi_{,i}^a + \mathcal{O}^2(\xi_{,i}^a) \quad (2.49)$$

$$= \xi_{,a}^a + \mathcal{O}^2(\xi_{,i}^a) \quad (2.50)$$

In the last step, we use the shorthand notation $Z_{R,a}^i \xi_{,i}^a \equiv \xi_{,a}^a$.

$$\begin{aligned} \epsilon^{ik} \epsilon^{jl} E_{ij} E_{kl} &= \frac{1}{4} Z_{R,c}^i \delta^{cd} Z_{R,d}^k [\xi_{,i}^a \delta_{ab} X_{R,j}^b + X_{R,i}^a \delta_{ab} \xi_{,j}^b] \\ &\quad Z_{R,e}^j \delta^{ef} Z_{R,f}^l [\xi_{,k}^a \delta_{ab} X_{R,l}^b + X_{R,k}^a \delta_{ab} \xi_{,l}^b] + \mathcal{O}^4(\xi_{,i}^a) \\ &= \frac{1}{4} \delta^{cd} [Z_{R,c}^i \xi_{,i}^a \delta_{ab} Z_{R,e}^j X_{R,j}^b + Z_{R,c}^i X_{R,i}^a \delta_{ab} Z_{R,e}^j \xi_{,j}^b] \\ &\quad \delta^{ef} [Z_{R,d}^k \xi_{,k}^a \delta_{ab} Z_{R,f}^l X_{R,l}^b + Z_{R,d}^k X_{R,k}^a \delta_{ab} Z_{R,f}^l \xi_{,l}^b] + \mathcal{O}^4(\xi_{,i}^a) \\ &= \frac{1}{4} \delta^{cd} [\xi_{,c}^a \delta_{ab} \delta_e^b + \delta_c^a \delta_{ab} \xi_{,e}^b] \delta^{ef} [\xi_{,d}^a \delta_{ab} \delta_f^b + \delta_d^a \delta_{ab} \xi_{,f}^b] + \mathcal{O}^4(\xi_{,i}^a) \\ &= \frac{1}{2} [\xi_{,e}^d \xi_{,d}^e + \xi_{,e}^d \xi_{d,e}^e] + \mathcal{O}^4(\xi_{,i}^a) \end{aligned} \quad (2.51)$$

Hence to second order in $\xi_{,i}^a$,

$$W(E) = \frac{\lambda}{2} (\xi_{,a}^a)^2 + \frac{\mu}{2} (\xi_{,e}^d \xi_{,d}^e + \xi_{,e}^d \xi_{d,e}^e). \quad (2.52)$$

2.5.1 Dynamical solution for normal modes of a sphere

The action for a free solid elastic body in nonlinear elasticity can be written as

$$S[X] = \int_{t_i}^{t_f} dt \int_{\mathcal{S}} d^3 \zeta \sqrt{\epsilon} \left[\frac{1}{2} \rho_0 \dot{X}^a g_{ab} \dot{X}^b - W(E) \right]. \quad (2.53)$$

Replacing the expressions for the kinetic energy and the potential energy for the Saint Venant-Kirchhoff model in linear elasticity in the action (Eq. (2.53) and using Cartesian coordinates with $g_{ab} = \delta_{ab}$,

$$S[\xi] = \int_{t_i}^{t_f} dt \int_{\mathcal{S}} d^3\zeta \sqrt{\epsilon} \left[\frac{1}{2} \rho_0 \dot{\xi}^a \delta_{ab} \dot{\xi}^b - \frac{\lambda}{2} (\xi^a_{,a})^2 - \frac{\mu}{2} (\xi^d_{,e} \xi^e_{,d} + \xi^d_{,e} \xi^e_{,d}) \right]. \quad (2.54)$$

We can transform the integral over $d^3\zeta$ to an integral over d^3x using the Jacobian of the transformation $|\det(X^a_{R,i})| = 1/\sqrt{\epsilon}$. The action becomes

$$S[\xi] = \int_{t_i}^{t_f} dt \int_{\mathcal{R}} d^3x \left[\frac{1}{2} \rho_0 \dot{\xi}^a \delta_{ab} \dot{\xi}^b - \frac{\lambda}{2} (\xi^a_{,a})^2 - \frac{\mu}{2} (\xi^d_{,e} \xi^e_{,d} + \xi^d_{,e} \xi^e_{,d}) \right] \quad (2.55)$$

where \mathcal{R} is the spatial extent of the undeformed body. The variation of the action is

$$\delta S = \int_{t_i}^{t_f} dt \int_{\mathcal{R}} d^3x \left[\rho_0 \dot{\xi}^a \delta_{ac} \delta \dot{\xi}^c - [\lambda \xi^a_{,a} \delta_c^d + \mu (\xi^d_{,c} + \xi_{c,d}^d)] \delta \xi^c \right]. \quad (2.56)$$

We integrate by parts to remove the derivatives on $\delta \xi^a$ and use the fact that variations vanish at t_i and t_f ,

$$\begin{aligned} \delta S = & \int_{t_i}^{t_f} dt \int_{\mathcal{R}} d^3x \left[-\rho_0 \ddot{\xi}^a \delta_{ac} + \lambda \xi^a_{,a,d} \delta_c^d + \mu (\xi^d_{,c,d} + \xi_{c,d}^d) \right] \delta \xi^c \\ & - \int_{t_i}^{t_f} dt \int_{\partial \mathcal{R}} d^3x \left[\lambda \xi^a_{,a} \delta_c^d + \mu (\xi^d_{,c} + \xi_{c,d}^d) \right] \delta \xi^c n_d \end{aligned} \quad (2.57)$$

where n_c is the normal to the boundary. Setting $\delta S = 0$, gives the equations on the bulk,

$$-\rho_0 \ddot{\xi}^c + \lambda \xi^a_{,a,c} + \mu (\xi^d_{,c,d} + \xi_{c,d}^d) = 0 \quad (2.58)$$

and on the boundary,

$$\lambda \xi^a_{,a} n_c + \mu (\xi^d_{,c} + \xi_{c,d}^d) n_d = 0. \quad (2.59)$$

Since the physical space is flat three-dimensional space, we generalize these results by replacing partial derivatives with covariant derivatives. The bulk equation becomes

$$\rho_0 \ddot{\xi}^c = \lambda \nabla^c \nabla_a \xi^a + \mu (\nabla_d \nabla^c \xi^d + \nabla_d \nabla^d \xi^c) = 0. \quad (2.60)$$

Simplifying,

$$\ddot{\xi}^c = \left(\frac{\lambda + \mu}{\rho_0} \right) \nabla^c \nabla_a \xi^a + \frac{\mu}{\rho_0} \nabla_d \nabla^d \xi^c = 0. \quad (2.61)$$

The boundary equation becomes

$$\lambda \nabla_a \xi^a n^c + \mu (\nabla^c \xi^d + \nabla^d \xi^c) n_d = 0. \quad (2.62)$$

The nonrelativistic normal mode vibrations of solid elastic sphere are described in the classic paper by Lamb (1881) and also later in Love (1892). These normal modes can be separated into two classes, the spheroidal and torsional modes. In this thesis, we focus on the spheroidal modes since we do not expect torsional modes to be excited due to the symmetry of the problem we simulate. The subset of the spheroidal modes with $\ell = 0$ are called the radial modes. Spherical coordinates, $\zeta^i = \{r, \theta, \phi\}$ are used to simplify the problem. From Thorne and Blandford (2017), the general spheroidal mode solution satisfying Eqs. (2.61) and (2.62) is

$$\vec{\xi}_{nlm}(t, r, \theta, \phi) = A_{nlm} \vec{\Xi}_{nlm}(r, \theta, \phi) \cos(\omega_{nl} t + \phi_{nlm}) \quad (2.63)$$

where A_{nlm} is the amplitude, ϕ_{nlm} is the phase and ω_{nl} is the angular frequency. The vector field $\vec{\Xi}_{nlm}$ is given by

$$\vec{\Xi}_{nlm}(r, \theta, \phi) = f_{nl}(r) Y_{\ell m} \hat{r} + g_{nl}(r) \left[\frac{\partial Y_{\ell m}}{\partial \theta} \hat{\theta} + \frac{1}{\sin \theta} \frac{\partial Y_{\ell m}}{\partial \phi} \hat{\phi} \right] \quad (2.64)$$

where $Y_{\ell m}$ are the real spherical harmonics defined by

$$Y_{\ell m} = \begin{cases} (-1)^m \sqrt{2} \sqrt{\frac{2\ell+1}{4\pi} \frac{(\ell-|m|)!}{(\ell+|m|)!}} P_\ell^{|m|}(\cos \theta) \sin(|m|\phi) & \text{if } m < 0 \\ \sqrt{\frac{2\ell+1}{4\pi}} P_\ell^m(\cos \theta) & \text{if } m = 0 \\ (-1)^m \sqrt{2} \sqrt{\frac{2\ell+1}{4\pi} \frac{(\ell-m)!}{(\ell+m)!}} P_\ell^m(\cos \theta) \cos(m\phi) & \text{if } m > 0 \end{cases} \quad (2.65)$$

where P_ℓ^m are the associated Legendre polynomials. The functions, $f_{nl}(r)$ and $g_{nl}(r)$ are

$$f_{nl}(r) = \frac{\alpha_{nl}}{k_{Lnl}} j'_\ell(k_{Lnl} r) + \frac{\beta_{nl}}{k_{Tnl}} l(l+1) \frac{j_\ell(k_{Tnl} r)}{k_{Tnl} r}, \quad (2.66)$$

$$g_{nl}(r) = \frac{\alpha_{nl}}{k_{Lnl}} \frac{j_\ell(k_{Lnl} r)}{k_{Lnl} r} + \frac{\beta_{nl}}{k_{Tnl}} \left[\frac{j_\ell(k_{Tnl} r)}{k_{Tnl}} + r j'_\ell(k_{Tnl} r) \right] \quad (2.67)$$

where $j_\ell(x)$ is the spherical Bessel function, $j'_\ell(x) \equiv \partial j_\ell(x)/\partial x$ and

$$k_{Ln\ell} \equiv \frac{\omega_{n\ell}}{C_L} \quad (2.68)$$

$$k_{Tn\ell} \equiv \frac{\omega_{n\ell}}{C_T}. \quad (2.69)$$

C_L and C_T are the longitudinal and transverse sound speeds:

$$C_L = \sqrt{\frac{\lambda + 2\mu}{\rho_0}}, \quad (2.70)$$

$$C_T = \sqrt{\frac{\mu}{\rho_0}}. \quad (2.71)$$

$\alpha_{n\ell}$ and $\beta_{n\ell}$ determine the weights of the longitudinal and transverse parts. Inserting the normal mode solution $\xi_{n\ell m}^z$ evaluated at the surface $r = a$ where a is the undeformed radius of the sphere and the unit normal $\hat{n} = \hat{r}$ in the boundary equation (2.62) results in two equations,

$$\alpha_{n\ell} [2j''_\ell(k_{Ln\ell}a) - ((k_{Tn\ell}/k_{Ln\ell})^2 - 2)j_\ell(k_{Ln\ell}a)] + \beta_{n\ell} [2\ell(\ell+1)f_1(k_{Tn\ell}a)] = 0 \quad (2.72)$$

$$\alpha_{n\ell} [2f_1(k_{Ln\ell}a)] + \beta_{n\ell} [j''_\ell(k_{Tn\ell}a) + (\ell(\ell+1) - 2)f_0(k_{Tn\ell}a)] = 0 \quad (2.73)$$

where $f_0(x) \equiv j_\ell(x)/x^2$ and $f_1(x) \equiv \partial(j_\ell(x)/x)/\partial x$. The simultaneous equations for $\alpha_{n\ell}$ and $\beta_{n\ell}$ have a solution if the determinant is zero,

$$\begin{aligned} & [2j''_\ell(k_{Ln\ell}a) - ((k_{Tn\ell}/k_{Ln\ell})^2 - 2)j_\ell(k_{Ln\ell}a)] [j''_\ell(k_{Tn\ell}a) + (\ell(\ell+1) - 2)f_0(k_{Tn\ell}a)] \\ & - [2f_1(k_{Ln\ell}a)] [2\ell(\ell+1)f_1(k_{Tn\ell}a)] = 0. \end{aligned} \quad (2.74)$$

Using $k_{Tn\ell}/k_{Ln\ell} = C_L/C_T$, Eq. (2.74) is expressed in terms of $k_{Tn\ell}$. The roots of Eq. (2.74) can be obtained numerically. The first root corresponds to the first value of n and so on.

For $C_L/C_T = \sqrt{3}$, $\ell = 2$, the solutions for the first four n values are

$$\begin{aligned} \frac{k_{Tn2}a}{\pi} = \{ & 0.840296489389027, 1.5486644471166677 \\ & , 2.651265258574347, 3.113122717920612, \dots \}. \end{aligned} \quad (2.75)$$

The dependence of the functions, $f_{n\ell}(r)$ and $g_{n\ell}(r)$, on r for $\ell = 2$, and $n = 0, 1, 2$ is shown in Figure 2.1.

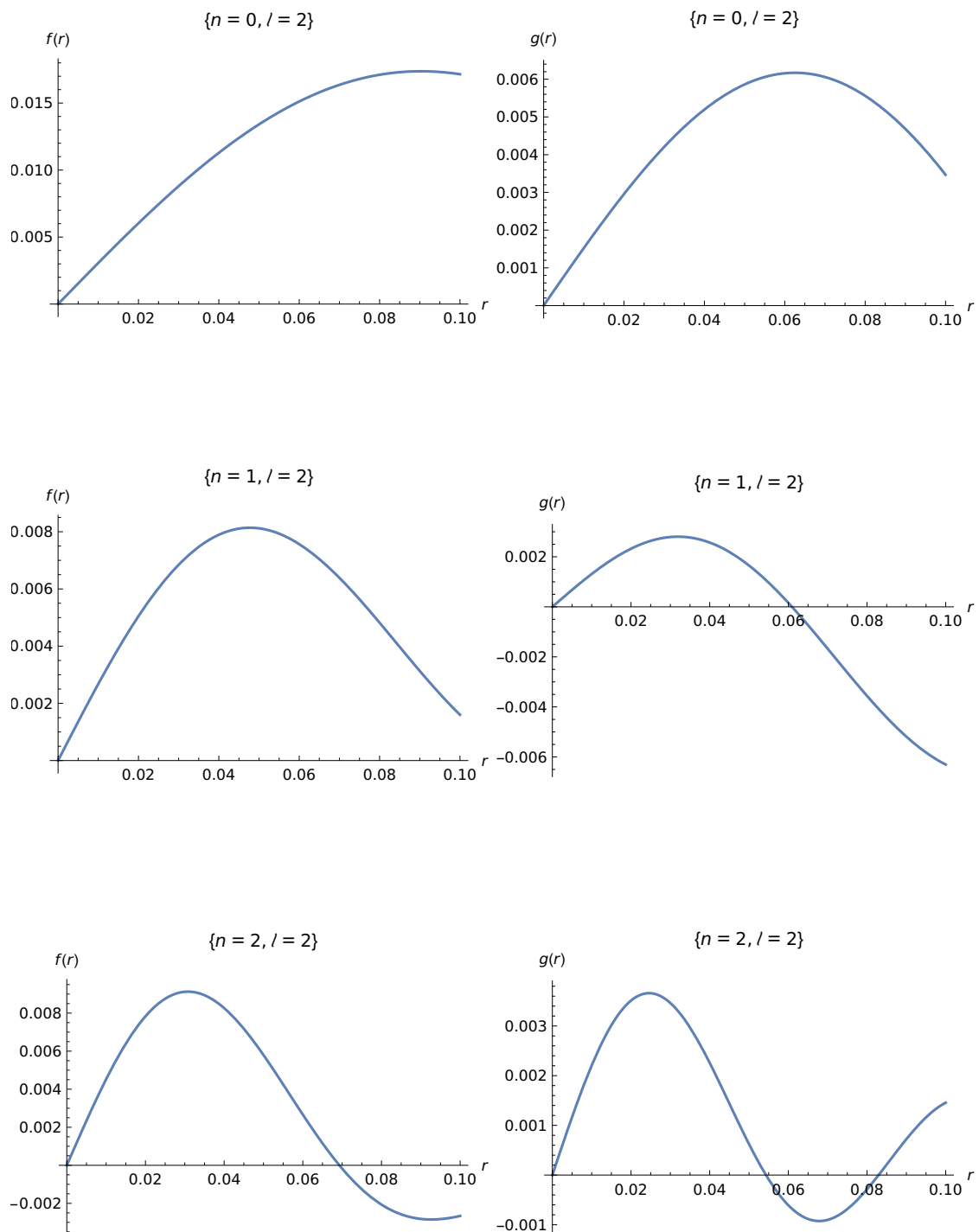


Figure 2.1: The radial dependence of $f_{n\ell}(r)$ and $g_{n\ell}(r)$ for $\ell = 2$ and different values of n . The surface of the sphere is at $r = 0.1$.

2.5.2 Static solution for a sphere under tidal forces

Love (1892) has solved the problem of a solid homogeneous elastic sphere in static equilibrium under the action of a potential that can be expressed in terms of spherical harmonics. The deformation of the sphere is assumed to be small. In the bulk, the static equilibrium equation is:

$$(\lambda + \mu) \nabla^a \nabla_b \xi^b + \mu \nabla^b \nabla_b \xi^a - \rho_0 \nabla^a \Phi_{\text{ext}} = 0 \quad (2.76)$$

The boundary equation is still Eq. (2.62).

The Newtonian tidal potential of a black hole of mass M can be expanded in terms of spherical harmonics (Press and Teukolsky (1977)). If we assume that the geometric center of the sphere lies on the z -axis and the central mass is at the origin, the tidal potential considering only the lowest ℓ term is

$$\Phi_{\text{ext}} = -\sqrt{4\pi/5}(M/R^3)r^2 Y_{20} \quad (2.77)$$

where R is the areal radius of the geometric center of the elastic sphere and r is the radial distance of an element of the elastic body from the geometric center of the elastic body. The solution, $\vec{\xi}_s$, satisfying Eqs. (2.76) and (2.62) for Φ_{ext} in Eq. (2.77) is obtained from Section 181 in Love (1892) by setting $g = 0$ and $\omega = 0$ for zero self-gravity and for the sphere to be nonrotating. We verified that the solution satisfies the bulk and boundary equations. The static solution is

$$\vec{\xi}_s = f_s(r) Y_{20} \hat{r} + g_s(r) \frac{\partial Y_{20}}{\partial \theta} \hat{\theta} \quad (2.78)$$

where

$$f_s(r) = \frac{k\rho_0}{70(\lambda + 2\mu)} \left[-20r^3 + 14a^2 r \frac{(\lambda + 3\mu)}{\mu} + \frac{(7\lambda + 6\mu)}{\mu(19\lambda + 14\mu)} \left[42r(a^2 - r^2)(\lambda + \mu) + 6r^3(2\lambda + 7\mu) \right] \right], \quad (2.79)$$

$$g_s(r) = \frac{k\rho_0}{70(\lambda + 2\mu)} \left[-5r^3 + 7a^2 r \frac{(\lambda + 3\mu)}{\mu} + \frac{(7\lambda + 6\mu)}{\mu(19\lambda + 14\mu)} \left[21r(a^2 - r^2)(\lambda + \mu) - 2r^3(2\lambda + 7\mu) \right] \right] \quad (2.80)$$

and $k = \sqrt{4\pi/5}(M/R^3)$ and a is the undeformed radius of the sphere.

CHAPTER

3

GENERAL RELATIVISTIC ELASTICITY THEORY

In this chapter, we give a brief review of elasticity theory in general relativity using a Lagrangian formulation as developed by Brown (2021). We focus on the action, gauge invariance of the action and the stress-energy-momentum tensor as derived in Brown (2021). In this chapter and the rest of this thesis, except when describing nonrelativistic elasticity, we use the sign conventions of Misner et al. (1973) and geometrical units in which $c = G = 1$.

3.1 Overview

The earliest work on generalizing elasticity theory to work with special relativity is by Herglotz (1911). Subsequently, DeWitt (1962) extended Herglotz formulation of relativistic elasticity theory to the general relativistic domain to describe a “stiff elastic medium” as an additional structure to physical spacetime to aid the formulation of a theory of quantum gravity. Later works on general relativistic elasticity theory include Carter and Quintana (1972), Kijowski and Magli (1992), Beig and Schmidt (2017) and Gundlach et al. (2011).

Some of these works favor an Eulerian formulation where the matter space is absent while the others use a Lagrangian approach. From the Lagrangian approach one can obtain the Eulerian picture. In the Lagrangian picture the focus is on the maps from matter space and a time parameter to physical spacetime while in the Eulerian picture the focus is on the inverse maps that take a spacetime event to the material point in matter space. The advantage of the Lagrangian formulation for numerical modeling is that it is easier to implement boundary conditions such as natural boundary conditions (Lanczos (1949)) where the surface is free to move whereas in the Eulerian formulation the surface is not clearly defined. Also, in the Lagrangian approach, only the equations of motion of the material points have to be numerically solved whereas in the Eulerian approach usually the numerical solution of fields over a large grid covering the relevant part of spacetime is needed.

Relativistic hydrodynamics is a very successful theory and is widely used to model fluids in strong gravity and at high Lorentz factors. A major difference between relativistic hydrodynamics and general relativistic elasticity is that shear stresses are absent in relativistic hydrodynamics.

3.2 Worldtube, radar metric

Let four-dimensional spacetime manifold be denoted by \mathcal{M} . Let the spacetime coordinates on \mathcal{M} be denoted by x^μ where $\mu = 0, 1, 2, 3$ and let the metric on \mathcal{M} be denoted by $g_{\mu\nu}$. Let λ be a real parameter. The matter space, \mathcal{S} , is the space of material points with coordinates ζ^i for $i = 1, 2, 3$. It should be noted that there is no predefined notion of distance on \mathcal{S} . The functions $X^\mu(\lambda, \zeta)$ are maps from $\mathfrak{R} \times \mathcal{S}$ to \mathcal{M} . As λ is continuously varied, $X^\mu(\lambda, \zeta)$ evaluated at a material point ζ^i traces the timelike worldline of the material point. The collection of all worldlines corresponding to the material points of the body is called the world tube. Let “ $_{,\mu}$ ” denote $\partial/\partial x^\mu$, “ $_{,i}$ ” denote $\partial/\partial \zeta^i$ and overdot denote $\partial/\partial \lambda$. The four-velocity of a material point is

$$U^\mu = \frac{\dot{X}^\mu}{\alpha} \quad (3.1)$$

where

$$\alpha = \sqrt{-\dot{X}^\mu \dot{X}_\mu} \quad (3.2)$$

is known as the material lapse function.

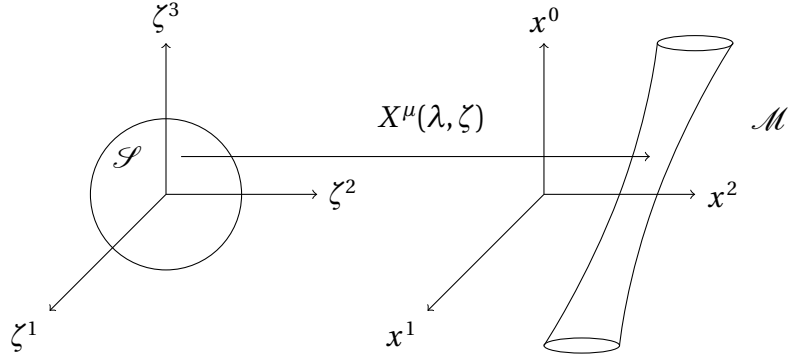


Figure 3.1: $X^\mu(\lambda, \zeta)$ maps a material point with coordinates ζ^i in \mathcal{S} and a real parameter λ to the spacetime event x^μ inside the world tube in four-dimensional spacetime, \mathcal{M} .

The radar metric, $f_{\mu\nu}$, defined inside the worldtube is

$$f_{\mu\nu} = g_{\mu\nu} + U_\mu U_\nu. \quad (3.3)$$

The name “radar” comes from Landau and Lifshitz (1951) who used light signals to find the “spatial” distance between two infinitesimally separated events in general relativity. It is easy to see that $f_{\mu\nu}U^\mu = 0$ and that $f_\mu^\nu V^\mu$ is orthogonal to U^μ for any vector V^ν . Hence, $f_{\mu\nu}$ is a “projection tensor” that projects V^μ into the space orthogonal to U^μ . The radar metric can be mapped back to the matter space,

$$f_{ij} = X_{,i}^\mu f_{\mu\nu} X_{,j}^\nu. \quad (3.4)$$

The radar metric in the matter space gives distances between infinitesimally separated material points such that the distance is measured in the rest frame of the material points in physical space, \mathcal{M} . That is, $ds^2 = f_{ij}d\zeta^i d\zeta^j$, is proper distance between material points. The Lagrangian strain tensor can be obtained the same way as in nonrelativistic elasticity using f_{ij} and the relaxed metric, ϵ_{ij} ,

$$E_{ij} = (f_{ij} - \epsilon_{ij})/2. \quad (3.5)$$

3.3 Action

As mentioned in Chapter 2, for a hyperelastic body, a stored energy function can be defined. For example, the stored energy can be specified in terms of the Lagrangian strain E_{ij} as

in the Saint Venant-Kirchhoff hyperelastic energy model. The energy density per unit of undeformed volume is denoted by $\rho(E)$ and is function of E_{ij} and ϵ_{ij} and can also depend on ζ if the material is not uniform. The dependence on ϵ_{ij} and ζ has been omitted in the notation to make it more compact. The relativistic action of a hyperelastic body is (DeWitt (1962), Brown and Marolf (1996), Brown (2021)),

$$S[X, g] = - \int_{\lambda_i}^{\lambda_f} d\lambda \int_{\mathcal{S}} d^3\zeta \sqrt{\epsilon} \alpha \rho(E). \quad (3.6)$$

The relativistic action for a point particle of rest mass, m , is (Landau and Lifshitz (1951)),

$$S_{\text{particle}}[X] = -m \int_{\lambda_i}^{\lambda_f} d\lambda \alpha. \quad (3.7)$$

The action for the hyperelastic body is an extension of the action of a continuum of dust particles that do not interact. The interaction energy of the hyperelastic body is obtained by using distances computed in the rest frames of elements of the hyperelastic body. The energy density can be written as

$$\rho(E) = \rho_0 + W(E) \quad (3.8)$$

where ρ_0 is the rest mass per unit undeformed volume and W is the potential energy per unit undeformed volume.

3.4 Gauge invariance of the action

Similar to the action of the relativistic particle, the action of the hyperelastic body is invariant under a change in the worldline parameter λ . Consider a history described by two different parametrizations. Let the worldlines of the material points be obtained by the new mapping $\tilde{X}^\mu(\lambda, \zeta)$. The new mapping is related to the old mapping by

$$\tilde{X}^\mu(\lambda, \zeta) = X^\mu(\Lambda(\lambda, \zeta), \zeta). \quad (3.9)$$

It should be noted that the new parameter is allowed to be a function of ζ . The action with the new mapping, $\tilde{X}^\mu(\lambda, \zeta)$, is

$$\bar{S}[\tilde{X}] = - \int_{\lambda_i}^{\lambda_f} d\lambda \int_{\mathcal{S}} d^3\zeta \sqrt{\epsilon} \tilde{\alpha} \left(\tilde{X}(\lambda, \zeta), \frac{\partial \tilde{X}(\lambda, \zeta)}{\partial \lambda} \right) \tilde{\rho} \left(\tilde{X}(\lambda, \zeta), \frac{\partial \tilde{X}(\lambda, \zeta)}{\partial \lambda}, \frac{\partial \tilde{X}(\lambda, \zeta)}{\partial \zeta} \right). \quad (3.10)$$

The partial derivatives of $\tilde{X}^\mu(\lambda, \zeta)$ are related to the partial derivatives of $X^\mu(\lambda, \zeta)$ by

$$\frac{\partial \tilde{X}^\mu}{\partial \lambda} = \frac{\partial X^\mu}{\partial \lambda} \Big|_{\lambda=\Lambda} \frac{\partial \Lambda}{\partial \lambda} \quad (3.11)$$

$$\frac{\partial \tilde{X}^\mu}{\partial \zeta^i} = \frac{\partial X^\mu}{\partial \lambda} \Big|_{\lambda=\Lambda} \frac{\partial \Lambda}{\partial \zeta^i} + \frac{\partial X^\mu}{\partial \zeta^i} \Big|_{\lambda=\Lambda} \quad (3.12)$$

where $\Lambda = \Lambda(\lambda, \zeta)$. We can express $\tilde{\alpha}$ and $\tilde{\rho}$ in the action in terms of α and ρ . If $\tilde{\alpha}$ and $\tilde{\rho}$ only depended on \tilde{X}^μ , that would be easily written using Eq. (3.9). However, since they also contain partial derivatives of \tilde{X} , we need Eqs. (3.11) and (3.12),

$$\tilde{\alpha} = \sqrt{-\frac{\partial \tilde{X}^\mu}{\partial \lambda} \frac{\partial \tilde{X}_\mu}{\partial \lambda}} \quad (3.13)$$

$$= \frac{\partial \Lambda}{\partial \lambda} \sqrt{-\frac{\partial X^\mu}{\partial \lambda} \Big|_{\lambda=\Lambda} \frac{\partial X_\mu}{\partial \lambda} \Big|_{\lambda=\Lambda}} \quad (3.14)$$

$$= \frac{\partial \Lambda}{\partial \lambda} \alpha \Big|_{\lambda=\Lambda} \quad (3.15)$$

The dependence of $\tilde{\rho}$ on \tilde{X} is through \tilde{f}_{ij} ,

$$\tilde{f}_{ij} = \frac{\partial \tilde{X}^\mu}{\partial \zeta^i} (\tilde{g}_{\mu\nu} + \tilde{U}_\mu \tilde{U}_\nu) \frac{\partial \tilde{X}^\nu}{\partial \zeta^j}. \quad (3.16)$$

We look at the parts of \tilde{f}_{ij} .

$$\begin{aligned} \frac{\partial \tilde{X}^\mu}{\partial \zeta^i} \tilde{g}_{\mu\nu} \frac{\partial \tilde{X}^\nu}{\partial \zeta^j} &= -\alpha^2 \Big|_{\Lambda=\lambda} \frac{\partial \Lambda}{\partial \zeta^i} \frac{\partial \Lambda}{\partial \zeta^j} \\ &+ \alpha U^\mu g_{\mu\nu} \frac{\partial X^\nu}{\partial \zeta^j} \Big|_{\lambda=\Lambda} \frac{\partial \Lambda}{\partial \zeta^i} + \alpha U^\nu g_{\mu\nu} \frac{\partial X^\mu}{\partial \zeta^i} \Big|_{\lambda=\Lambda} \frac{\partial \Lambda}{\partial \zeta^j} \\ &+ \frac{\partial X^\mu}{\partial \zeta^i} g_{\mu\nu} \frac{\partial X^\nu}{\partial \zeta^j} \Big|_{\lambda=\Lambda} \end{aligned} \quad (3.17)$$

$$\tilde{U}_\mu = \frac{1}{\tilde{\alpha}} \frac{\partial \tilde{X}_\mu}{\partial \lambda} \quad (3.18)$$

$$= \frac{1}{\alpha} \frac{\partial X_\mu}{\partial \lambda} \Big|_{\lambda=\Lambda} \quad (3.19)$$

$$= U_\mu|_{\lambda=\Lambda} \quad (3.20)$$

$$\frac{\partial \tilde{X}^\mu}{\partial \zeta^i} \tilde{U}_\mu = -\alpha|_{\lambda=\Lambda} \frac{\partial \Lambda}{\partial \zeta^i} + U_\mu \frac{\partial X^\mu}{\partial \zeta^i} \Big|_{\lambda=\Lambda} \quad (3.21)$$

where $|_{\lambda=\Lambda}$ applies to all the functions before it. We find that

$$\tilde{\rho} = \rho|_{\lambda=\Lambda}. \quad (3.22)$$

Using the results above, the action (3.10) is

$$\tilde{S}[\tilde{X}] = - \int_{\lambda_i}^{\lambda_f} d\lambda \int_{\mathcal{S}} d^3\zeta \frac{\partial \Lambda(\lambda, \zeta)}{\partial \lambda} \sqrt{\epsilon} \alpha \rho|_{\lambda=\Lambda}. \quad (3.23)$$

Let $\Lambda(\lambda_i, \zeta) = \lambda_i$ and $\Lambda(\lambda_f, \zeta) = \lambda_f$. We can change integration variables to $d\Lambda d^3\zeta = d\lambda d^3\zeta (\partial \Lambda / \partial \lambda)$ and find that $\tilde{S}[\tilde{X}] = S[X]$. The action is gauge invariant.

Because of the gauge invariance of the action, we can freely choose the worldline parameter λ . For example, we can choose λ to be equal to proper time. In that case, $\alpha = 1$. However, we can only set λ to proper time after varying the action since if we set λ equal to proper time before varying the action, then the variations with endpoints, λ_i and λ_f , all have the same change in proper time.

Let $x^0 = \text{const}$ correspond to spacelike hypersurfaces and let $x^\mu \equiv \{t, x^a\}$ where $a = 1, 2, 3$. Then, the coordinate basis vectors $\partial / \partial x^a$ are spacelike. If $t = \text{const}$ are spacelike, we can choose the parameterization $\lambda = x^0 \equiv t$. Then, $\dot{X}^0 = 1$ and $X_{,i}^0 = 0$ and the action in the $\lambda = t$ gauge can be written as

$$S[X] = \int_{t'}^{t''} dt \int_{\mathcal{S}} d^3\zeta \mathcal{L}(X, \dot{X}, X_{,i}, t) \quad (3.24)$$

where the Lagrangian density is $\mathcal{L}(X, \dot{X}, X_{,i}, t) = -\sqrt{\epsilon} \alpha \rho(E)$. The action is a functional of $X^a(t, \zeta)$.

3.5 Stress–energy–momentum tensor

The stress–energy–momentum (SEM) tensor for matter fields is obtained from the functional derivative of the matter action with respect to the metric,

$$T^{\mu\nu}(x) = \frac{2}{\sqrt{-g}} \frac{\delta S_{\text{matter}}}{\delta g_{\mu\nu}(x)}. \quad (3.25)$$

In the above definition, $T^{\mu\nu}$ is defined in terms of the functional derivative of the matter action with respect to the metric at spacetime points, x . Therefore, we write the matter action as an integral over spacetime,

$$S[X, g] = - \int d^4x \int_{\lambda_i}^{\lambda_f} d\lambda \int_{\mathcal{S}} d^3\zeta \sqrt{\epsilon} \alpha \rho \delta^4(x - X(\lambda, \zeta)). \quad (3.26)$$

Then, the functional derivative is given by

$$\frac{\delta S}{\delta g_{\mu\nu}(x)} = - \int_{\lambda_i}^{\lambda_f} d\lambda \int_{\mathcal{S}} d^3\zeta \sqrt{\epsilon} \left(\frac{\partial \alpha}{\partial g_{\mu\nu}} \rho + \frac{\alpha}{2} S^{ij} \frac{\partial f_{ij}}{\partial g_{\mu\nu}} \right) \delta^4(x - X(\lambda, \zeta)) \quad (3.27)$$

where $S^{ij} = \partial \rho / \partial E_{ij}$. We need the partial derivative of α and f_{ij} with respect to the metric:

$$\frac{\partial \alpha}{\partial g_{\mu\nu}} = -\frac{1}{2} \alpha U^\mu U^\nu \quad (3.28)$$

$$\frac{\partial f_{ij}}{\partial g_{\mu\nu}} = F_i^\mu F_j^\nu \quad (3.29)$$

where $F_i^\mu = f_{\nu}^\mu X_{,i}^\nu$. The SEM tensor is

$$T^{\mu\nu}(x) = \int_{\lambda_i}^{\lambda_f} d\lambda \int_{\mathcal{S}} d^3\zeta \frac{\alpha \sqrt{\epsilon}}{\sqrt{-g}} [\rho U^\mu U^\nu + S^{ij} F_i^\mu F_j^\nu] \delta^4(x - X(\lambda, \zeta)). \quad (3.30)$$

We evaluate $T^{\mu\nu}$ at the spacetime event, $x = X^\mu(\bar{\lambda}, \bar{\zeta})$, and convert the delta function from a function of X to a function of λ and ζ ,

$$\delta^4(X(\bar{\lambda}, \bar{\zeta}) - X(\lambda, \zeta)) = \frac{1}{|\det(X_{, \cdot})|} \delta(\bar{\lambda} - \lambda) \delta^3(\bar{\zeta} - \zeta) \quad (3.31)$$

where $\det(X; \cdot)$ is the determinant of the Jacobian of $X(\lambda, \zeta)$ with respect to λ and ζ . The SEM tensor is then,

$$T^{\mu\nu}(X(\bar{\lambda}, \bar{\zeta})) = \frac{\alpha\sqrt{\epsilon}}{\sqrt{-g}|\det(X; \cdot)|} [\rho U^\mu U^\nu + S^{ij} F_i^\mu F_j^\nu]. \quad (3.32)$$

The factor $\det(X; \cdot)$ can be analyzed by viewing $x^{\mu'} = (\lambda, \zeta^i)$ as new coordinates on \mathcal{M} which are related to the old coordinates by $x^\mu = X^\mu(x^{\mu'})$. The metric components in the primed coordinate system is related to the unprimed coordinate system by

$$g'_{\mu\nu} = \frac{\partial X^\alpha}{\partial x^{\mu'}} \frac{\partial X^\beta}{\partial x^{\nu'}} g_{\alpha\beta}. \quad (3.33)$$

Taking determinant on both sides and solving for $\det(X; \cdot)$,

$$|\det(X; \cdot)| = \sqrt{-g'}/\sqrt{-g}. \quad (3.34)$$

We find an expression for the metric in the primed coordinate system by looking at the line element,

$$ds^2 = dx^\mu g_{\mu\nu} dx^\nu \quad (3.35)$$

$$= (\dot{X}^\mu d\lambda + X_{,i}^\mu d\zeta^i) g_{\mu\nu} (\dot{X}^\nu d\lambda + X_{,j}^\nu d\zeta^j) \quad (3.36)$$

$$= \dot{X}^\mu \dot{X}_\mu d\lambda^2 + \dot{X}_\mu X_{,i}^\mu d\lambda d\zeta^i + \dot{X}_\mu X_{,j}^\mu d\lambda d\zeta^j + X_{,i}^\mu X_{,j}^\mu d\zeta^i d\zeta^j. \quad (3.37)$$

We use the definitions of α , f_{ij} and $v_i \equiv U_\mu X_{,i}^\mu$ to replace

$$\dot{X}^\mu \dot{X}_\mu = -\alpha^2 \quad (3.38)$$

$$\dot{X}_\mu X_{,i}^\mu = \alpha U_\mu X_{,i}^\mu = \alpha v_i \quad (3.39)$$

$$X_{,i}^\mu X_{,j}^\mu = f_{ij} - X_{,i}^\mu U_\mu U_\nu X_{,j}^\nu = f_{ij} - v_i v_j \quad (3.40)$$

in the line element. From the line element, the metric in the primed coordinates can be written in block matrix form,

$$g'_{\mu\nu} = \begin{pmatrix} -\alpha^2 & \alpha v_i \\ \alpha v_j & f_{ij} - v_i v_j \end{pmatrix}. \quad (3.41)$$

Using the formula for the determinant of a block matrix,

$$\det \begin{pmatrix} A & B \\ C & D \end{pmatrix} = \det(A) \det(D - CA^{-1}B), \quad (3.42)$$

we obtain

$$\det(g') = -\alpha^2 f \quad (3.43)$$

where $f = \det(f_{ij})$. The final form of the SEM tensor is

$$T^{\mu\nu}(X(\lambda, \zeta)) = \frac{1}{J} [\rho U^\mu U^\nu + S^{ij} F_i^\mu F_j^\nu] \quad (3.44)$$

where $J \equiv \sqrt{f}/\sqrt{\epsilon}$. The metric ϵ_{ij} gives distances between material points ζ^i in \mathcal{S} when the elastic body is relaxed and f_{ij} gives distances between material points ζ^i in \mathcal{S} when the elastic body is deformed. Therefore, the factor $1/J$ converts energy density per unit undeformed volume to per unit deformed volume. The SEM tensor satisfies local conservation, $\nabla_\mu T^{\mu\nu} = 0$ (Brown (2021)).

CHAPTER

4

NUMERICAL METHOD

In this chapter, we describe the numerical method used to model the motion of a hyperelastic body in curved spacetime.

4.1 Overview

Numerical methods for solving partial differential equations (PDEs) include finite difference (FD), finite volume (FV) and finite element (FE) methods. FE methods are particularly used in solving elasticity problems since they allow boundaries of elastic bodies to be represented more closely using triangular or tetrahedral meshes than the rectangular grid used in FD and FV methods. In FD methods, the PDEs are discretized directly whereas in FV methods, the PDEs are integrated over a volume element and in FE methods, the PDEs are converted to a weak form by multiplying with a basis function and integrating over the domain. Though FD methods might seem simpler to implement, they are known to be less robust than FV methods.

We discretize the action of the elastic body directly instead of using the partial differential equations of motion since this leads to the free surface or natural boundary condition where

variations at the boundary are nonzero, to be trivially implemented via the variational process. We use the discretization of FE methods with basis functions and tetrahedral elements to be able to model elastic bodies of any shape such as spheres or ellipsoids that can describe solid astrophysical objects. We only discretize the action in space and not in time and obtain ordinary differential equations (ODEs) in mass matrix form for which there is a suite of well-tested methods that can be used. Though we use linear tetrahedral elements, we still obtain second order convergence.

We used Matlab's partial differential equation toolbox (The MathWorks Inc. (2021)) to generate a linear tetrahedral mesh for three-dimensional bodies. To be able to utilize computing clusters, we parallelized the algorithm by partitioning the mesh using the software package Metis (Karypis and Kumar (1997)) and used the Message Passing Interface (MPI) to communicate neighbor information.

4.2 Matter space discretization

The matter space \mathcal{S} is divided into non-overlapping elements. Let \mathcal{S}_E for $E = 1, 2, \dots$ denote the elements, that is, \mathcal{S} is the union of the \mathcal{S}_E 's. Let $n = 1, 2, \dots$ label the nodes throughout the body. Each node in the body has a unique index number. Let $\mathcal{N}(E)$ denote the set of nodes in element E . An example of $\mathcal{N}(E)$ is shown in Figure 4.1. Then, for $\zeta^i \in \mathcal{S}_E$, we have

$$X^a(t, \zeta) = \sum_{n \in \mathcal{N}(E)} X_n^a(t) \phi_n^E(\zeta), \quad \zeta^i \in \mathcal{S}_E \quad (4.1)$$

where the sum is over the nodes contained in the element \mathcal{S}_E . Note that the shape functions $\phi_n^E(\zeta)$ depend on the node as well as the element.

4.3 Semi-discretized action

The action in the $\lambda = t$ gauge (Eq. (3.24)) is discretized using Eq. (4.1),

$$S[X] = \int_{t'}^{t''} dt \sum_E \int_{\mathcal{S}_E} d^3\zeta \mathcal{L} \left(\sum_{n \in \mathcal{N}(E)} X_n^a(t) \phi_n^E(\zeta), \sum_{n \in \mathcal{N}(E)} \dot{X}_n^a(t) \phi_n^E(\zeta), \sum_{n \in \mathcal{N}(E)} X_n^a(t) \phi_{n,i}^E \right) \quad (4.2)$$

where the action is a functional of the coordinates of each node, $X_n^a(t)$. We have dropped the explicit time dependence of the Lagrangian density on t in Eq. (4.2) for simplicity.

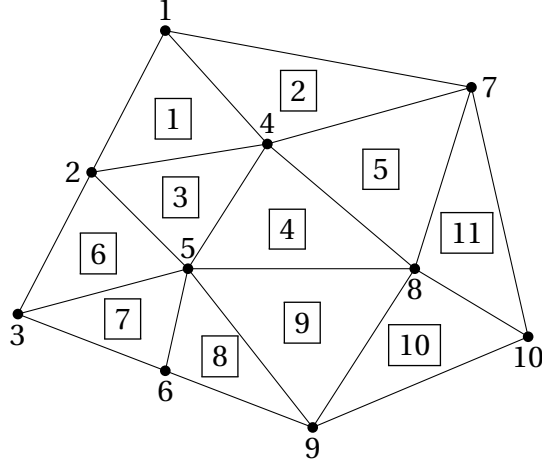


Figure 4.1: Here we are depicting a two-dimensional triangular mesh instead of a tetrahedral mesh for clarity. This figure shows node labels, $n = \{1, 2, \dots, 10\}$ and element labels $E = \{1, 2, \dots, 11\}$ (boxed). The set of nodes in element, $E = 4$, is $\mathcal{N}(4) = \{4, 5, 8\}$. The ring of node, $n = 5$, is $\mathcal{R}(5) = \{3, 4, 6, 7, 8, 9\}$.

We select the element type to be linear tetrahedral elements with nodes at the vertices only. A general tetrahedral element \mathcal{S}_E is transformed into a unit trirectangular tetrahedron \mathcal{T} with coordinates η^i . Let $\zeta_{(\alpha)}^i$ denote the coordinates of the four nodes, for $\alpha = 0, 1, 2, 3$. The transformation is linear, with $\zeta^i = A^{ij}\eta^j + B^i$ where A^{ij} and B^i are constants in each element. Then,

$$B^i = \zeta_{(0)}^i, \quad (4.3)$$

$$A^{i1} = \zeta_{(1)}^i - \zeta_{(0)}^i, \quad (4.4)$$

etc. In the new coordinates, the nodes have coordinates $\eta_{(0)}^i = (0, 0, 0)$, $\eta_{(1)}^i = (1, 0, 0)$, $\eta_{(2)}^i = (0, 1, 0)$, and $\eta_{(3)}^i = (0, 0, 1)$. Figure 4.2 shows the transformation.

Let $\alpha(n)$ map the four node numbers of E to the set $\{0, 1, 2, 3\}$. The shape function defined in terms of the new coordinates η are

$$\bar{\phi}_{\alpha(n)}(\eta) \equiv \phi_n^E(\zeta(\eta)). \quad (4.5)$$

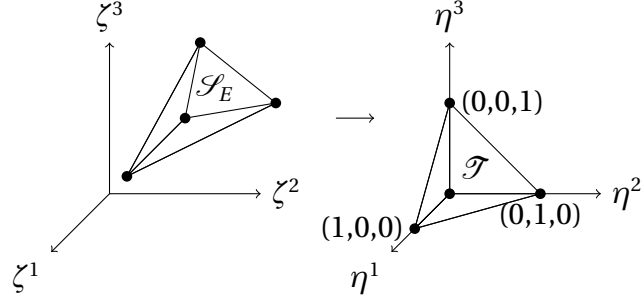


Figure 4.2: A general tetrahedral element \mathcal{S}_E is transformed into a unit trirectangular tetrahedron \mathcal{T} .

Explicitly, the linear shape function are given in Hughes (2012) (Eqs. 3.1.19-3.1.22),

$$\begin{aligned}
\bar{\phi}_0(\eta) &= 1 - \eta^1 - \eta^2 - \eta^3 \\
\bar{\phi}_1(\eta) &= \eta^1 \\
\bar{\phi}_2(\eta) &= \eta^2 \\
\bar{\phi}_3(\eta) &= \eta^3
\end{aligned} \tag{4.6}$$

In the new coordinates, the action is

$$S[X] = \int_{t'}^{t''} dt \sum_E \int_{\mathcal{T}} d^3\eta |J_E| \mathcal{L} \left(\sum_{n \in \mathcal{N}(E)} X_n^a(t) \bar{\phi}_{\alpha(n)}(\eta), \sum_{n \in \mathcal{N}(E)} \dot{X}_n^a(t) \bar{\phi}_{\alpha(n)}(\eta), \sum_{n \in \mathcal{N}(E)} X_n^a(t) \phi_{n,i}^E \right) \tag{4.7}$$

where $|J_E|$ is determinant of the Jacobian of the transformation from ζ^i to η^i for element E . We can pull $|J_E|$ outside the integral since it is independent of η^i . It should be noted that $\phi_{n,i}^E$ are constants, independent of η^i .

We now replace the integral over η^i in each element with a quadrature rule:

$$S[X] = \int_{t'}^{t''} dt \sum_E \sum_{\sigma} w_{\sigma} |J_E| \mathcal{L} \left(\sum_{n \in \mathcal{N}(E)} X_n^a(t) \bar{\phi}_{\alpha(n)}(\eta_{(\sigma)}), \sum_{n \in \mathcal{N}(E)} \dot{X}_n^a(t) \bar{\phi}_{\alpha(n)}(\eta_{(\sigma)}), \sum_{n \in \mathcal{N}(E)} X_n^a(t) \phi_{n,i}^E \right) \tag{4.8}$$

for some set of points $\eta_{(\sigma)}^i$ in \mathcal{T} . We choose the points to coincide with the nodes (vertices)

of the element, and choose weights $w_\sigma = 1/24$ for each node. The weights $w_\sigma = 1/24$ makes the integration of linear functions using the quadrature points at the vertices of the tetrahedron exact. We find $\bar{\phi}_\alpha(\eta_{(\sigma)}) = \delta_{\alpha\sigma}$. Thus,

$$S[X] = \int_{t'}^{t''} dt \sum_E \sum_\sigma w_\sigma |J_E| \mathcal{L} \left(\sum_{n \in \mathcal{N}(E)} X_n^a(t) \delta_{\alpha(n)\sigma}, \sum_{n \in \mathcal{N}(E)} \dot{X}_n^a(t) \delta_{\alpha(n)\sigma}, \sum_{n \in \mathcal{N}(E)} X_n^a(t) \phi_{n,i}^E \right) \quad (4.9)$$

For each value of σ in the sum, the only term in the first argument of \mathcal{L} that is nonzero is the one for which $\alpha(n) = \sigma$. Likewise for the second argument of \mathcal{L} . Thus, we can write this as

$$S[X] = \frac{1}{24} \int_{t'}^{t''} dt \sum_E \sum_{n \in \mathcal{N}(E)} |J_E| \mathcal{L} \left(X_n^a(t), \dot{X}_n^a(t), \sum_{m \in \mathcal{N}(E)} X_m^a(t) \phi_{m,i}^E \right). \quad (4.10)$$

Let $\mathcal{R}(n)$ be the "ring" of n . This is the list of elements (E values) that have n as one of their nodes. An example of $\mathcal{N}(E)$ is shown in Figure 4.1. We isolate the terms that involve the variable X_N^a for some fixed node number N . Let these terms be denoted by S_N :

$$S_N = \frac{1}{24} \int_{t'}^{t''} dt \sum_{E \in \mathcal{R}(N)} \sum_{n \in \mathcal{N}(E)} |J_E| \mathcal{L} \left(X_n^a(t), \dot{X}_n^a(t), \sum_{m \in \mathcal{N}(E)} X_m^a(t) \phi_{m,i}^E \right) \quad (4.11)$$

Only elements in the ring of N depend on the node X_N^a . In the sum over nodes for each element, there are two cases. One case is when the node number n equals N , the other is when it does not equal N . Therefore,

$$S_N = \frac{1}{24} \int_{t'}^{t''} dt \sum_{E \in \mathcal{R}(N)} |J_E| \left\{ \mathcal{L} \left(X_N^a(t), \dot{X}_N^a(t), \sum_{m \in \mathcal{N}(E)} X_m^a(t) \phi_{m,i}^E \right) + \sum_{n \in \mathcal{N}(E), n \neq N} \mathcal{L} \left(X_n^a(t), \dot{X}_n^a(t), \sum_{m \in \mathcal{N}(E)} X_m^a(t) \phi_{m,i}^E \right) \right\}. \quad (4.12)$$

It should be noted that X_N^a occurs in the third argument of \mathcal{L} in both terms.

We now vary S with respect to X_N^a :

$$\delta S = \frac{1}{24} \int_{t'}^{t''} dt \sum_{E \in \mathcal{R}(N)} |J_E| \left\{ \left. \frac{\partial \mathcal{L}}{\partial X^a} \right|_{N,E} \delta X_N^a + \left. \frac{\partial \mathcal{L}}{\partial \dot{X}^a} \right|_{N,E} \delta \dot{X}_N^a + \left. \frac{\partial \mathcal{L}}{\partial X_{,i}^a} \right|_{N,E} \phi_{N,i}^E \delta X_N^a + \sum_{n \in \mathcal{N}(E), n \neq N} \left. \frac{\partial \mathcal{L}}{\partial X_{,i}^a} \right|_{n,E} \phi_{N,i}^E \delta X_N^a \right\} \quad (4.13)$$

where the symbol $|_{n,E}$ indicates that the partial derivatives are evaluated at $X^a = X_n^a$, $\dot{X}^a = \dot{X}_n^a$, and $X_{,i}^a = \sum_{m \in \mathcal{N}(E)} X_m^a(t) \phi_{m,i}^E$. The last two terms in δS can be combined into a single sum over all $n \in \mathcal{N}(E)$. Then the functional derivative (Lagrange's equation) is

$$0 = \frac{\delta S}{\delta X_N^a} = \frac{1}{24} \sum_{E \in \mathcal{R}(N)} |J_E| \left\{ \left. \frac{\partial \mathcal{L}}{\partial X^a} \right|_{N,E} - \frac{d}{dt} \left(\left. \frac{\partial \mathcal{L}}{\partial \dot{X}^a} \right|_{N,E} \right) + \sum_{n \in \mathcal{N}(E)} \left. \frac{\partial \mathcal{L}}{\partial X_{,i}^a} \right|_{n,E} \phi_{N,i}^E \right\} \quad (4.14)$$

Next, we expand the total time derivative.

$$\frac{d}{dt} \left(\left. \frac{\partial \mathcal{L}}{\partial \dot{X}^a} \right|_{N,E} \right) = \left. \frac{\partial^2 \mathcal{L}}{\partial \dot{X}^b \partial \dot{X}^a} \right|_{N,E} \ddot{X}_N^b + \left. \frac{\partial^2 \mathcal{L}}{\partial X^b \partial \dot{X}^a} \right|_{N,E} \dot{X}_N^b + \left. \frac{\partial^2 \mathcal{L}}{\partial X_{,i}^b \partial \dot{X}^a} \right|_{N,E} \sum_{m \in \mathcal{N}(E)} \dot{X}_m^b \phi_{m,i}^E \quad (4.15)$$

Then, the equations of motion are

$$\underbrace{\sum_{E \in \mathcal{R}(n)} |J_E| \left. \frac{\partial^2 \mathcal{L}}{\partial \dot{X}^b \partial \dot{X}^a} \right|_{n,E}}_{(M_{ab})_n} \ddot{X}_n^b = \underbrace{\left\{ \sum_{E \in \mathcal{R}(n)} |J_E| \left. \frac{\partial \mathcal{L}}{\partial X^a} \right|_{n,E} + \sum_{m \in \mathcal{N}(E)} \left. \frac{\partial \mathcal{L}}{\partial X_{,i}^a} \right|_{m,E} \phi_{n,i}^E - \left. \frac{\partial^2 \mathcal{L}}{\partial X^b \partial \dot{X}^a} \right|_{n,E} \dot{X}_n^b - \left. \frac{\partial^2 \mathcal{L}}{\partial X_{,i}^b \partial \dot{X}^a} \right|_{n,E} \sum_{m \in \mathcal{N}(E)} \dot{X}_m^b \phi_{m,i}^E \right\}}_{(F_a)_n}$$

where N has been replaced by n and n by m . For each value of n , the coefficient of \ddot{X}_n^b is a 3×3 matrix in the indices a and b . Denoting the coefficient of \ddot{X}_n^b as $(M_{ab})_n$ and the right hand side of the equation as $(F_a)_n$, a matrix equation can be written for all variables to be evolved, X_n^a and \dot{X}_n^a , for $a = 1, 2, 3$ and $n = 1$ to N_{total} where N_{total} is the total number of

nodes.

$$\underbrace{\begin{bmatrix} 1 & 0 & \dots & \dots & \dots & \dots & \dots & 0 \\ 0 & 1 & \dots & \dots & \dots & \dots & \dots & 0 \\ \vdots & \vdots & \ddots & \dots & \dots & \dots & \dots & 0 \\ \dots & \dots & \dots & (M_{11})_1 & (M_{12})_1 & (M_{13})_1 & \dots & 0 \\ \dots & \dots & \dots & (M_{21})_1 & (M_{22})_1 & (M_{23})_1 & \dots & 0 \\ \dots & \dots & \dots & (M_{31})_1 & (M_{32})_1 & (M_{33})_1 & \dots & 0 \\ \vdots & & & & & & & \\ 0 & \dots & \dots & \dots & \dots & \dots & \dots & \dots \end{bmatrix}}_{\text{mass matrix, } M} \frac{d}{dt} \begin{pmatrix} X_1^1 \\ X_1^2 \\ \vdots \\ \dot{X}_1^1 \\ \dot{X}_1^2 \\ \dot{X}_1^3 \\ \vdots \\ \vdots \end{pmatrix} = \underbrace{\begin{bmatrix} \dot{X}_1^1 \\ \dot{X}_1^2 \\ \vdots \\ (F_1)_1 \\ (F_2)_1 \\ (F_3)_1 \\ \vdots \\ \vdots \end{bmatrix}}_{\text{vector, } F} \quad (4.16)$$

The mass matrix M is pentadiagonal. We use the subroutine DGBSV from the Fortran Linear Algebra Package (LAPACK) which uses lower–upper (LU) decomposition to solve the linear system of equations and obtain the derivatives of the variables to be evolved. We use the fourth order Runge-Kutta scheme to evolve X_n^a and \dot{X}_n^a at discrete values of t . We found numerically that the Courant condition,

$$\Delta t \leq h_{\min}/c_{\max} \quad (4.17)$$

where Δt is the time step size, h_{\min} is the minimum edge length of the tetrahedral elements and c_{\max} is the maximum speed of sound in the material, must be met for stability.

4.4 Code validation

Exact solutions are available for the small oscillations of a free solid elastic sphere treated using nonrelativistic linear elasticity (Eq. (2.63)). Hence, we are able to validate the numerical code against known solutions. We set the metric to be the Minkowski metric in the code. The numerical code is fully relativistic and is based on nonlinear elasticity. To ensure that the discrepancy between the numerical and exact solution is not due to relativistic and nonlinear elasticity effects, we used small amplitudes for the normal modes and small sound speeds. The relativistic terms in the elastic body action are first order and higher in v^2/c^2 where $v^2 = \dot{X}^a \dot{X}_a$ and c is the speed of light. We obtained the maximum value of v^2 from the numerical solution and verified that v^2/c^2 is smaller than machine epsilon for double precision. The nonlinear elasticity terms are first order and higher in $(\xi_i^a)^3$ in

the action. We also obtained the maximum value of X_i^a from the numerical solution and verified that $(X_i^a)^3$ is smaller than machine epsilon.

We choose the analytical solution to be a combination of two normal modes,

$$\begin{aligned}
\vec{\xi}_{\text{analytical}}(t, r, \theta, \phi) &= \vec{\xi}_{020}(t, r, \theta, \phi) + \vec{\xi}_{031}(t, r, \theta, \phi) \\
&= A_{020} \vec{\Xi}_{020}(r, \theta, \phi) \cos(\omega_{02} t + \phi_{020}) \\
&\quad + A_{031} \vec{\Xi}_{031}(r, \theta, \phi) \cos(\omega_{03} t + \phi_{031})
\end{aligned} \tag{4.18}$$

We set X^a for all nodes in the code at the first time step such that their displacement from their relaxed coordinate is equal to Eq. (4.18) evaluated at $t = 0$ and \dot{X}^a is equal to the time derivative of Eq. (4.18) evaluated at $t = 0$. We numerically evolve the coordinates and velocities in time.

We use four mesh refinements with $h_{\text{max}} = [a/4, a/8, a/16, a/32]$ where h_{max} is the maximum edge length of the tetrahedral elements and a is the undeformed radius of the sphere. Figures 4.3 and 4.4 show the analytical and numerical displacement and velocity of a node for the mesh size, $h_{\text{max}} = a/8$ and $h_{\text{max}} = a/16$ as a function of time. Figure 4.5 is the log-log plot of the L2-norm error in the coordinates and velocities at the last time step as function of h_{max} indicating 2^{nd} order convergence of the integration scheme.

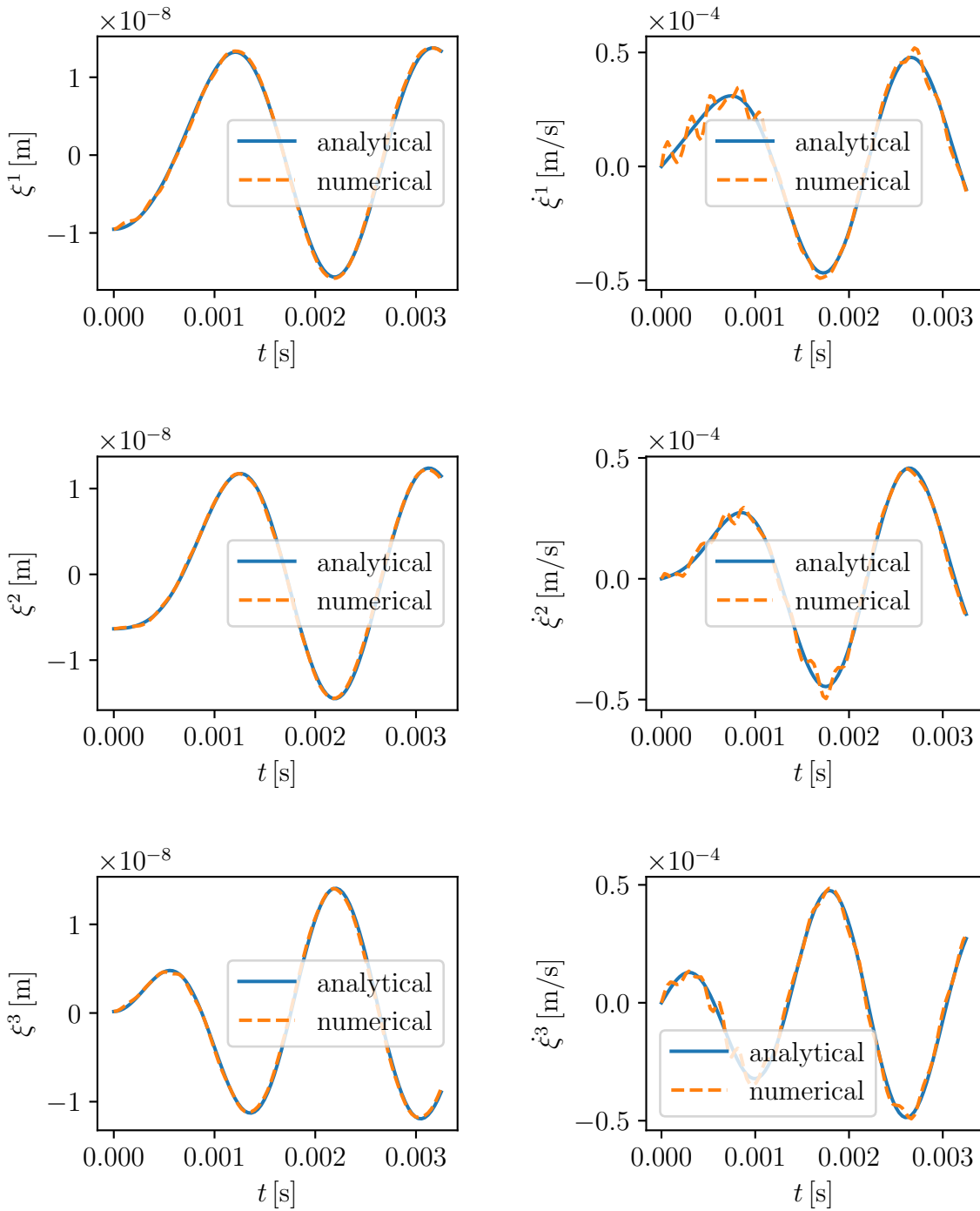


Figure 4.3: Analytical and numerical displacements and velocities for a node as a function of time for $h_{\max} = a/8$.

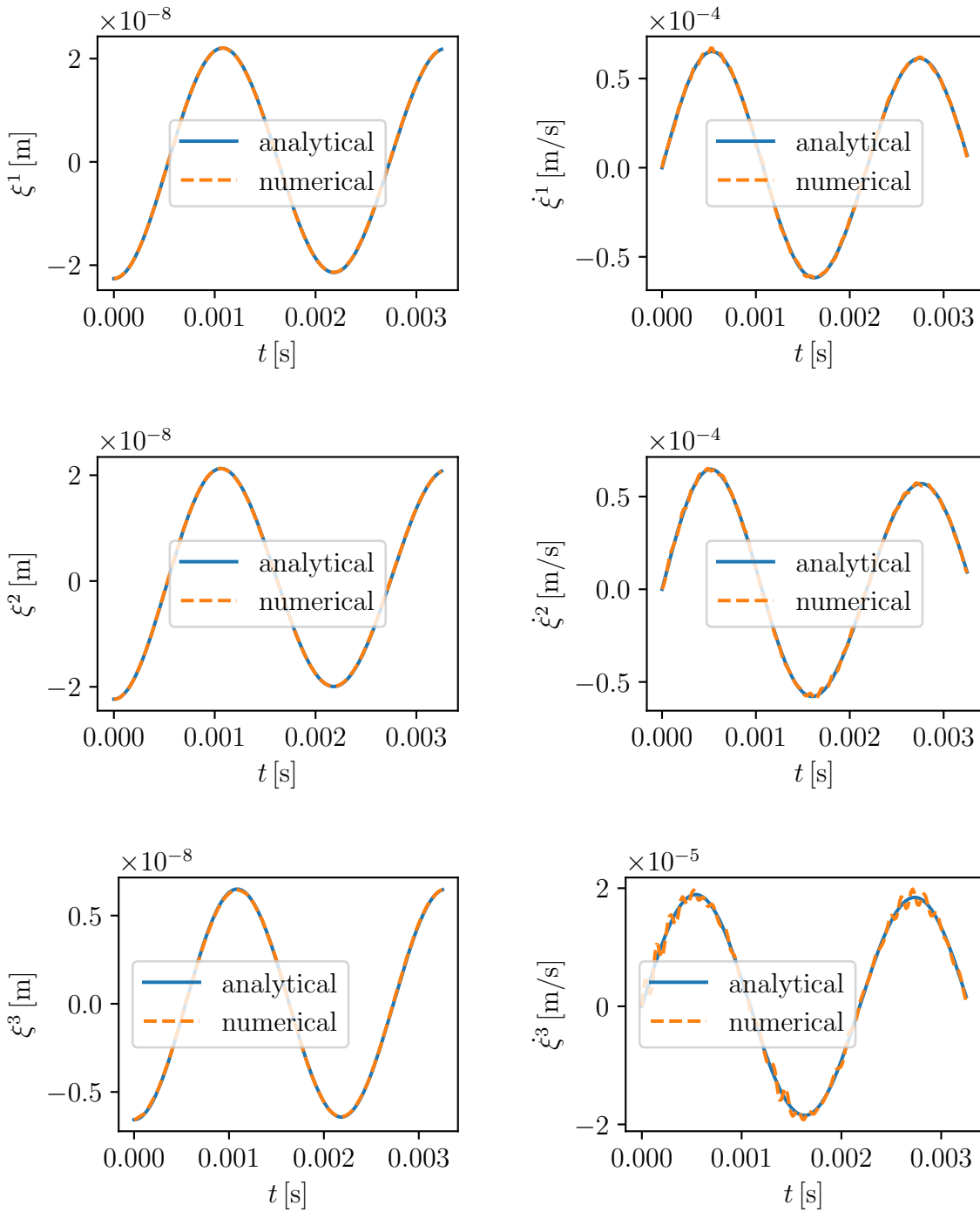


Figure 4.4: Analytical and numerical displacements and velocities for a node as a function of time for $h_{\max} = a/16$.

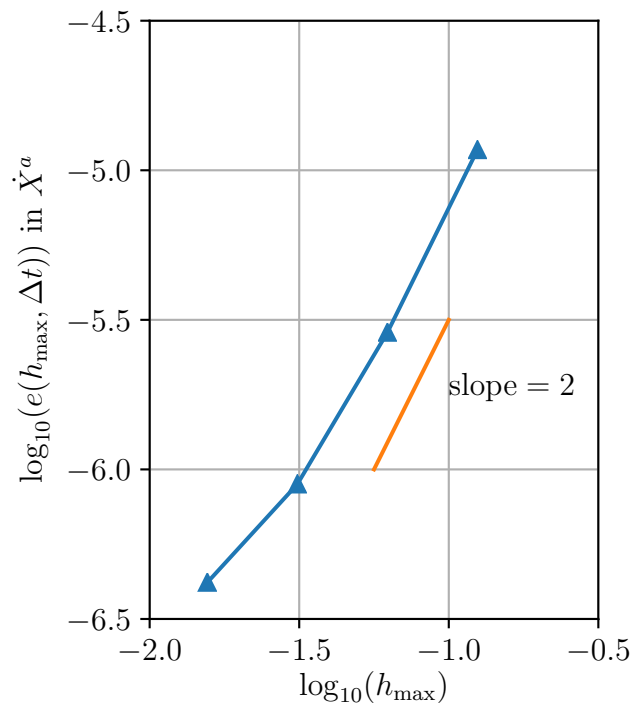
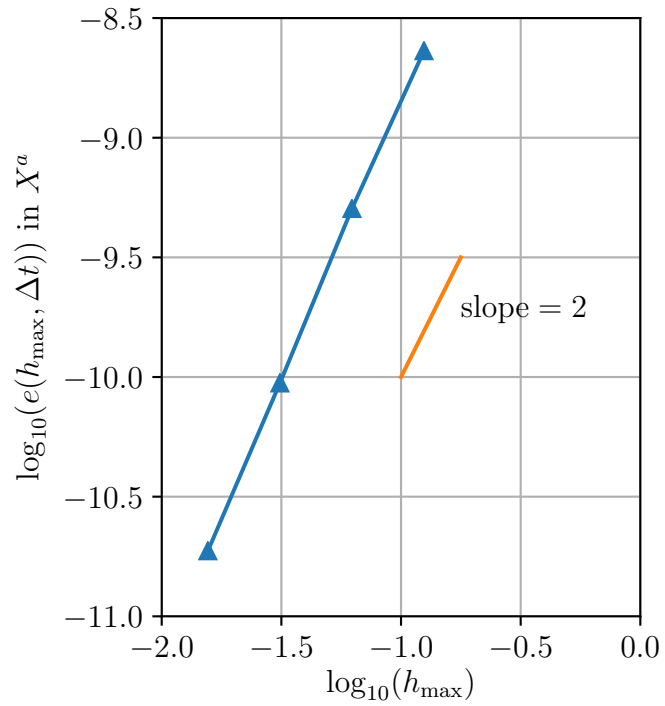


Figure 4.5: Convergence of the algorithm measured in terms of the L2-norm of the error in the coordinates and velocities.

CHAPTER

5

FERMI FRAMES

In this chapter, we describe how we construct Fermi frames about different worldlines after the numerical time evolution of the elastic body is over and how we compute an approximate center of mass of the elastic body.

5.1 Overview

In curved spacetime, for a sufficiently small region around a spacetime event, \mathcal{P} , coordinates can be constructed such that the metric in these coordinates at \mathcal{P} is equal to the Minkowski metric $\eta_{\alpha\beta}$, and all the Christoffel symbols in these coordinates at \mathcal{P} are zero. The coordinates are known as “normal” coordinates. Since the Christoffel symbols vanish at \mathcal{P} , free particles locally move on straight lines and hence the coordinates are said to be locally inertial (Misner et al. (1973)). However, such coordinate systems are only defined at a single spacetime event.

Given a timelike geodesic that may correspond to the worldline of a physical inertial observer, normal coordinates can be constructed valid along the worldline of the observer. One specific way of constructing normal coordinates along a timelike geodesic leads

to coordinates called Fermi-normal coordinates (Manasse and Misner (1963), Ishii et al. (2005)). Fermi-normal coordinates are constructed by defining a tetrad, $e_a^\mu \equiv \{e_0^\mu, e_a^\mu\}$, where $a = 1, 2, 3$, at the spacetime location of the observer. The timelike leg, e_0^μ , is set equal to the four velocity of the observer and the spacelike legs, e_a^μ , are set initially so that $e_a^\mu e_{\mu\beta} = \eta_{\alpha\beta}$. The spacelike legs are orthonormal to the four-velocity and they “infinitesimally” span the rest space of the observer at a point on the worldline. The spacelike legs are evolved using parallel transport along the observer’s worldline. The Fermi-normal coordinates are denoted $\bar{x}^\mu \equiv \{\bar{t}, \bar{x}^a\}$ for $a = 1, 2, 3$. The Fermi-normal coordinate \bar{t} is set equal to the proper time of the observer. Spatial geodesics are emitted from the observer’s worldline orthogonal to it and they reach spacetime events in the region around the worldline uniquely (provided a small enough region around the worldline is chosen so that geodesics do not cross). The spatial Fermi-normal coordinates of these events, \bar{x}^a , are such that $\bar{x}^a \delta_{ab} \bar{x}^b$ is the squared of the distance along the spatial geodesic to the spacetime event.

If the worldline of the observer is not a geodesic and therefore has nonzero four-acceleration, the procedure for constructing Fermi-normal coordinates is modified so that the spacelike tetrad legs are Fermi-Walker transported instead of parallel transported so that they keep being nonrotating (Synge (1960)). The metric in these coordinates evaluated on the worldline is equal to the Minkowski metric, however, not all the Christoffel symbols are zero on the worldline. Hence, these coordinates are not normal coordinates, they are called Fermi coordinates. We will refer to Fermi-normal coordinates as Fermi, as they are a subset of the latter, unless we want to refer only to the “Fermi-normal” property.

We want to define a Fermi frame travelling with the elastic body in which to compute physical quantities of the elastic body and extract useful information from simulations. The Fermi metric closely approximates the flat metric and physical quantities computed in a Fermi frame can be better understood since they correspond to locally observed quantities.

5.2 Numerical evaluation of Fermi coordinates and velocities

We would like to have the Fermi frame attached to an approximate center of mass of the elastic body. We refer to the center of mass as being approximate since center of mass of an extended body is not well-defined in curved spacetime, but we can compute an approximate center of mass when the dimension of the body is small compared to the radius of curvature of the spacetime. However, we first need a Fermi frame travelling with

the body to compute the center of mass.

We will obtain the spacetime coordinates and velocities of all nodes of the elastic body at discrete time steps after the numerical evolution is over. We can pick a node (fiducial node), define the Fermi frame about the node and use this frame to compute the center of mass. We want to compute the deviation of the center of mass from a geodesic and therefore need a Fermi frame about a geodesic. We convert the initial Fermi coordinate and velocity of the center of mass to spacetime coordinate and velocity. We numerically evolve a geodesic with the same initial spacetime coordinate and velocity of the center of mass. We obtain the Fermi frame about the geodesic and compute the center of mass again. We also construct a Fermi frame about the center of mass to compute conserved quantities described in Chapter 6.

We construct three different Fermi frames which we refer to as the “fiducial Fermi frame”, the “geodesic Fermi frame” and the “center of mass Fermi frame”. We will refer to the fiducial node, the geodesic and the center of mass as “observers”. The following subsections (except Subsection 5.2.1) applies to all three Fermi frames.

5.2.1 Choosing the fiducial node

We compute the center of mass of the elastic body when it is relaxed in flat spacetime. We assume that the center of mass lies inside the body or close. After dividing the relaxed elastic body into elements and nodes, we pick the node closest to the center of mass and call it the “fiducial” node.

5.2.2 Choosing the initial spacelike legs of the tetrads

Given the initial spacetime location and velocity of the observer carrying the tetrad, the initial spacelike legs of the tetrad are set, assuming the spacetime metric is diagonal, with

$$e_1^\mu(t=0) = \sqrt{g_{11}}(A\dot{X}^1, \frac{1}{g_{11}} + B(\dot{X}^1)^2, B\dot{X}^1\dot{X}^2, B\dot{X}^1\dot{X}^3) \quad (5.1)$$

$$e_2^\mu(t=0) = \sqrt{g_{22}}(A\dot{X}^2, B\dot{X}^2\dot{X}^1, \frac{1}{g_{22}} + B(\dot{X}^2)^2, B\dot{X}^2\dot{X}^3) \quad (5.2)$$

$$e_3^\mu(t=0) = \sqrt{g_{33}}(A\dot{X}^3, B\dot{X}^3\dot{X}^1, B\dot{X}^3\dot{X}^2, \frac{1}{g_{33}} + B(\dot{X}^3)^2) \quad (5.3)$$

where $A \equiv 1/(\alpha\sqrt{-g_{00}})$ and $B \equiv ((\sqrt{-g_{00}}/\alpha) - 1)/(\dot{X}^a\dot{X}_a)$. All the variables are evaluated at the initial spacetime location of the observer and using the initial velocity of the observer.

The spacelike legs of the tetrad satisfy $e_a^\mu V_\mu = 0$ where V^μ is the four-velocity of the observer and $e_a^\mu e_{\mu b} = \delta_{ab}$.

5.2.3 Fermi-Walker transport of the spatial legs of the tetrads

Fermi-Walker transport of a vector, W^μ , along a worldline with four velocity, U^μ , and four-acceleration, $A^\mu = U^\alpha \nabla_\alpha U^\mu$, where ∇_α denotes covariant derivative, $\nabla_\alpha W^\mu \equiv \partial W^\mu / \partial x^\alpha + \Gamma_{\alpha\beta}^\mu W^\beta$, is given by

$$U^\alpha \nabla_\alpha W^\mu = U^\mu (A_\alpha W^\alpha) - A^\mu (U_\alpha W^\alpha). \quad (5.4)$$

The spacelike legs of the tetrad are orthogonal to the four velocity of the observer hence the Fermi-Walker transport of e_a^μ along the observer's worldline is given by

$$U^\alpha \nabla_\alpha e_a^\mu = U^\mu (A_\alpha e_a^\alpha). \quad (5.5)$$

If $A^\mu = 0$, then Fermi-Walker transport (Eq. (5.4)) is equivalent to parallel transport,

$$U^\alpha \nabla_\alpha W^\mu = 0. \quad (5.6)$$

After computing the initial spacelike legs of the tetrads, we numerically evolve them using the Fermi-Walker equations. We obtain them at the same discrete times as the spacetime coordinates and velocities of the nodes of the elastic body.

5.2.4 Computing Fermi coordinates from spacetime coordinates on discrete $t = \text{const}$ time slices

Let t_- , t_0 and t_+ denote successive $t = \text{const}$ time slices (shown in Figure 5.1). We know the coordinates of each node at times t_- , t_0 and t_+ . The observer carrying the tetrad has coordinates $X_\mathcal{O}^\mu(t_0)$ at time t_0 . A generic node has coordinates $X_\mathcal{G}^a(t_-)$, $X_\mathcal{G}^a(t_0)$, $X_\mathcal{G}^a(t_+)$ at the three successive times. Let \bar{t} be the proper time along the observer's worldline at the event $X_\mathcal{O}^a(t_0)$. The $\bar{t} = \text{const}$ hypersurface is spanned by spatial geodesics that start out orthogonal to the observer's worldline at t_0 . Let \tilde{t} be the coordinate time along the generic node's worldline that is simultaneous (as seen by the observer) with the event $X_\mathcal{O}^a(t_0)$. Assuming

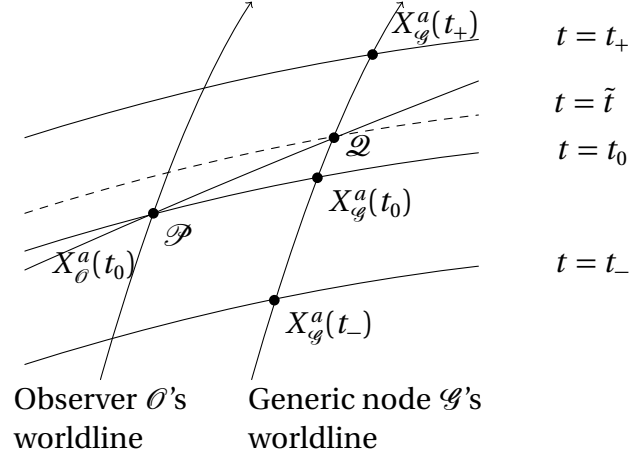


Figure 5.1: $t = \text{const}$ slices. Geodesic at \mathcal{P} orthogonal to the observer's worldline crosses the generic nodes's worldline at \mathcal{Q} .

that $t_- < \tilde{t} < t_+$,

$$\begin{aligned} X_{\mathcal{G}}^a(\tilde{t}) &= X_{\mathcal{G}}^a(t_0) + \dot{X}_{\mathcal{G}}^a(\tilde{t} - t_0) + \frac{1}{2} \ddot{X}_{\mathcal{G}}^a(t_0) (\tilde{t} - t_0)^2 + \dots \\ &= X_{\mathcal{G}}^a(t_0) + \frac{X_{\mathcal{G}}^a(t_+) - X_{\mathcal{G}}^a(t_-)}{2\Delta t} (\tilde{t} - t_0) + \frac{1}{2} \frac{X_{\mathcal{G}}^a(t_+) - 2X_{\mathcal{G}}^a(t_0) + X_{\mathcal{G}}^a(t_-)}{(\Delta t)^2} (\tilde{t} - t_0)^2 + \dots \end{aligned} \quad (5.7)$$

The Fermi coordinates of point \mathcal{Q} (shown in Figure 5.1) are \bar{x}^a and proper time at \mathcal{P} . From the definition of Fermi coordinates (Brown (2019)):

$$X_{(\mathcal{Q})}^{\mu} = X_{(\mathcal{P})}^{\mu} + e_{a(\mathcal{P})}^{\mu} \bar{x}^a - \frac{1}{2} \Gamma_{\alpha\beta}^{\mu}(\mathcal{P}) e_{a(\mathcal{P})}^{\alpha} e_{b(\mathcal{P})}^{\beta} \bar{x}^a \bar{x}^b + \mathcal{O}(3) \quad (5.8)$$

where $e_{a(\mathcal{P})}^{\mu}$ is the spacelike leg of the Fermi-Walker transported tetrad along the observer's worldline and the symbol $\mathcal{O}(3)$ represents terms of third order in \bar{x}^a . The $\mu = 0$ components are

$$\tilde{t} = t_0 + e_a^0(t_0) \bar{x}^a - \frac{1}{2} \Gamma_{\alpha\beta}^0(t_0) e_a^{\alpha}(t_0) e_b^{\beta}(t_0) \bar{x}^a \bar{x}^b + \mathcal{O}(3) \quad (5.9)$$

The $\mu = c$ components are

$$X_{\mathcal{G}}^c(\tilde{t}) = X_{\mathcal{G}}^c(t_0) + e_a^c(t_0) \bar{x}^a - \frac{1}{2} \Gamma_{\alpha\beta}^c(t_0) e_a^{\alpha}(t_0) e_b^{\beta}(t_0) \bar{x}^a \bar{x}^b + \mathcal{O}(3) \quad (5.10)$$

Combining Eqs (5.7), (5.9) and (5.10):

$$\begin{aligned}
& \frac{X_{\mathcal{G}}^c(t_+) - X_{\mathcal{G}}^c(t_-)}{2\Delta t} \underbrace{\left(e_a^0(t_0)\bar{x}^a - \frac{1}{2}\Gamma_{\alpha\beta}^0(t_0)e_a^\alpha(t_0)e_b^\beta(t_0)\bar{x}^a\bar{x}^b \right)}_{\bar{t}-t_0} \\
& + \frac{1}{2} \frac{X_{\mathcal{G}}^c(t_+) - 2X_{\mathcal{G}}^c(t_0) + X_{\mathcal{G}}^c(t_-)}{(\Delta t)^2} \underbrace{\left(e_a^0(t_0)\bar{x}^a - \frac{1}{2}\Gamma_{\alpha\beta}^0(t_0)e_a^\alpha(t_0)e_b^\beta(t_0)\bar{x}^a\bar{x}^b \right)^2}_{\bar{t}-t_0} \\
& = e_a^c(t_0)\bar{x}^a - \frac{1}{2}\Gamma_{\alpha\beta}^c(t_0)e_a^\alpha(t_0)e_b^\beta(t_0)\bar{x}^a\bar{x}^b \tag{5.11}
\end{aligned}$$

The above equations are solved with a nonlinear solver for \bar{x}^a . If t_0 corresponds to the first time step, we then use the values at the t_0 , t_+ and at the 3rd time step t_{++} and a forward finite difference scheme instead of the central finite difference scheme.

5.2.5 Fermi four-velocity of the nodes

Along with the Fermi coordinates of generic nodes, (\bar{t}, \bar{x}^a) , we also need their Fermi four-velocity, \bar{U}^μ , to compute the SEM tensor in the Fermi frame. We compute $X_{\mathcal{G}}^a(\bar{t})$ and $\dot{X}_{\mathcal{G}}^a(\bar{t})$ using the value of \bar{t} solved in Subsection 5.2.4,

$$X_{\mathcal{G}}^a(\bar{t}) \approx X_{\mathcal{G}}^a(t_0) + \frac{X_{\mathcal{G}}^a(t_+) - X_{\mathcal{G}}^a(t_-)}{2\Delta t}(\bar{t} - t_0) + \frac{1}{2} \frac{X_{\mathcal{G}}^a(t_+) - 2X_{\mathcal{G}}^a(t_0) + X_{\mathcal{G}}^a(t_-)}{(\Delta t)^2}(\bar{t} - t_0)^2 \tag{5.12}$$

$$\dot{X}_{\mathcal{G}}^a(\bar{t}) \approx \dot{X}_{\mathcal{G}}^a(t_0) + \frac{\dot{X}_{\mathcal{G}}^a(t_+) - \dot{X}_{\mathcal{G}}^a(t_-)}{2\Delta t}(\bar{t} - t_0) + \frac{1}{2} \frac{\dot{X}_{\mathcal{G}}^a(t_+) - 2\dot{X}_{\mathcal{G}}^a(t_0) + \dot{X}_{\mathcal{G}}^a(t_-)}{(\Delta t)^2}(\bar{t} - t_0)^2. \tag{5.13}$$

and use these values to compute $U^\mu(\bar{t})$. Let the four-velocity and the four acceleration of the observer be denoted by V^μ and A^μ . The Fermi components of the four-acceleration of the observer are:

$$\bar{A}_a = A_\mu e_a^\mu \tag{5.14}$$

$$\bar{A}_t = A_\mu V^\mu = 0. \tag{5.15}$$

The Fermi components of the Riemann tensor on the observer's worldline are, for example,

$$\bar{R}_{tatb}|_0 \equiv R_{\alpha\beta\sigma\rho}|_0 V^\alpha e_a^\beta V^\sigma e_b^\rho \tag{5.16}$$

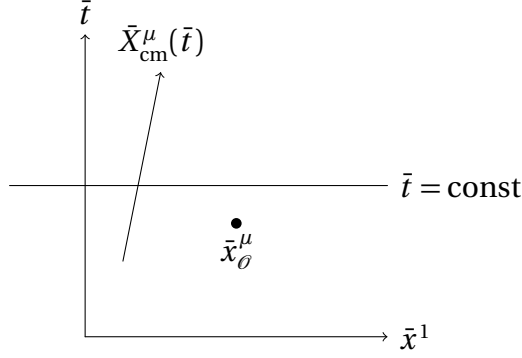


Figure 5.2: The worldline of the center of mass. The event \bar{x}_θ^μ does not lie on the $\bar{t} = \text{const}$ slice.

where $|_0$ means evaluation on the observer's worldline. From the definition of the Fermi coordinates (Eq. (5.8)), the tensor components transformation from spacetime to Fermi coordinates can be obtained. The Fermi components of a vector, ξ^μ , at event $X_{\mathcal{O}}^\mu(\bar{t})$, computed using the tensor components transformation, are given by (Brown (2019)):

$$\begin{aligned} \bar{\xi}^\nu(\bar{t}, \bar{x}) = & -V_\mu \xi^\mu(x)(1 - \bar{A}_a \bar{x}^a) - \xi^\mu(x) \Gamma_{\mu\beta}^\alpha |_0 V_\alpha e_a^\beta \bar{x}^a \\ & - \xi^\mu(x) \left[V_\mu \bar{A}_a \bar{A}_b + \frac{1}{3} \bar{R}_{tabc} e_\mu^c + V_\nu \left(\frac{1}{2} \partial_\mu \Gamma_{\alpha\beta}^\nu - \Gamma_{\mu\beta}^\nu A_\alpha \right) e_a^\alpha e_b^\beta \right] |_0 \bar{x}^a \bar{x}^b \\ & + \mathcal{O}(3) \end{aligned} \quad (5.17)$$

$$\begin{aligned} \bar{\xi}^a(\bar{t}, \bar{x}) = & \xi^\mu(x) e_\mu^a + \xi^\mu(x) \Gamma_{\mu\beta}^\alpha |_0 e_a^\alpha e_b^\beta \bar{x}^b + \frac{1}{3} \xi^\mu(x) \bar{R}^a{}_{cbd} |_0 e_\mu^d \bar{x}^b \bar{x}^c \\ & + \frac{1}{2} \xi^\mu(x) \partial_\mu \Gamma_{\alpha\beta}^\nu |_0 e_\nu^a e_b^\alpha e_c^\beta \bar{x}^b \bar{x}^c + \mathcal{O}(3) \end{aligned} \quad (5.18)$$

5.3 Center of mass and spin

5.3.1 Flat spacetime

In flat spacetime, due to Killing vector fields corresponding to space translations and rotations, total momentum and total angular momentum about a spacetime event are conserved and are independent of the hypersurface used to calculate them (Misner et al. (1973)). Let these quantities be computed by integrating the SEM tensor over the $\bar{t} = \text{const}$ slice in the Fermi frame defined about a non-accelerating observer in flat spacetime. The Fermi metric is equal to the Minkowski metric everywhere. Let the Fermi coordinates of the

event about which the total angular momentum is computed be \bar{x}_θ^μ . The event, \bar{x}_θ^μ , may not necessarily lie on the $\bar{t} = \text{const}$ slice as shown in Figure 5.2. The total momentum and total angular momentum about \bar{x}_θ^μ are computed with

$$\bar{P}^\mu = \int_{\bar{t}=\text{const}} d^3 \bar{x} \bar{T}^{t\mu} \quad (5.19)$$

$$\bar{J}^{\mu\nu} = 2 \int_{\bar{t}=\text{const}} d^3 \bar{x} (\bar{x}^{[\mu} - \bar{x}_\theta^{[\mu}) \bar{T}^{\nu]t}. \quad (5.20)$$

It can be shown that the center of mass and the spin vector can be computed directly from $\bar{J}^{\mu\nu}$ and \bar{P}^μ (Misner et al. (1973)) with

$$\bar{x}_{\text{cm}}^\mu = \bar{x}_\theta^\mu - \frac{1}{\bar{M}^2} \bar{J}^{\mu\nu} \bar{P}_\nu \quad (5.21)$$

$$\bar{S}_\mu = -\frac{1}{2\bar{M}} \bar{\epsilon}_{\mu\alpha\beta\gamma} \bar{J}^{\alpha\beta} \bar{P}^\gamma \quad (5.22)$$

where $\bar{M} = \sqrt{-\bar{P}^\mu \bar{P}_\mu}$ and $\bar{\epsilon}_{\mu\alpha\beta\gamma}$ is the Levi-Civita symbol.

5.3.2 Curved spacetime

In curved spacetime, such as in Schwarzschild spacetime, there is no Killing vector field corresponding to spatial translations, therefore total momentum is not conserved. The computation of the total momentum depends on the choice of hypersurface and also a way to transport the components of $T^{\mu\nu}$ in curved spacetime needs to be chosen.

We assume that the spacetime in the Fermi frame carried by the body is approximately flat and use the equations in Subsection 5.3.1 to compute an approximate center of mass in the Fermi frame. We need to numerically evaluate

$$\bar{P}^\mu = \int_{\bar{t}=\text{const}} d^3 \bar{x} \bar{T}^{t\mu} \quad (5.23)$$

and

$$\bar{J}^{\mu\nu} = 2 \int_{\bar{t}=\text{const}} d^3 \bar{x} (\bar{x}^{[\mu} - \bar{x}_\theta^{[\mu}) \bar{T}^{\nu]t} \quad (5.24)$$

where we choose \bar{x}_θ^μ to be the Fermi coordinates of the observer, $\bar{x}_\theta^\mu = (\bar{t}, 0, 0, 0)$. We first

convert to an integral over the matter space,

$$\bar{P}^\mu = \int_{\mathcal{S}} d^3\zeta \det(\bar{X}_{,i}^a) \bar{T}^{t\mu} \quad (5.25)$$

$$\bar{J}^{\mu\nu} = 2 \int_{\mathcal{S}} d^3\zeta \det(\bar{X}_{,i}^a) (\bar{x}^{[\mu} - \bar{x}_\theta^{[\mu}) \bar{T}^{\nu]t}. \quad (5.26)$$

We then use the Fermi coordinates and four-velocities of nodes as computed using the procedure in 5.2 and apply the discretization in Chapter 4 to numerically compute \bar{P}^μ and $\bar{J}^{\mu\nu}$.

5.3.3 Road map for finding the deviation of the center of mass in the geodesic Fermi frame

Further away from the black hole, in the geodesic Fermi frame, the computation of the center of mass becomes more accurate. We can choose starting and ending points of the simulation far from the black such as in a scattering orbit and obtain accurate values for the deviation of the center of mass from a geodesic due to the encounter. We choose the geodesic that starts out at the same initial spacetime coordinates and initial velocity as the center of mass. The following describes the road map followed to obtain the deviation of the center of mass as measured in the geodesic Fermi frame.

- Define a Fermi frame about the fiducial node and obtain the Fermi coordinates and velocities of all nodes
- Compute the Fermi coordinates of the center of mass, \bar{x}_{cm}^μ in the fiducial Fermi frame using Eq. (5.21).
- Interpolate the value of \bar{x}_{cm}^a at \bar{x}_{cm}^0 using sixth order Lagrange interpolation to obtain its value at the discrete values of \bar{t} .
- Convert the interpolated Fermi coordinates of the center of mass to spacetime coordinates using Eq. (5.8).
- Evolve a geodesic with initial spacetime coordinates and velocity equal to that of the center of mass at $t = 0$.
- Also, evolve a tetrad about the geodesic using parallel transport.

- Define a Fermi frame about the geodesic and compute the Fermi coordinates of all nodes in the geodesic Fermi frame.
- Compute the Fermi coordinates of the center of mass in the geodesic Fermi frame using Eq. (5.21).

CHAPTER

6

CONSERVATION LAWS

In this chapter we consider the conservation laws for an elastic body moving in a spacetime with symmetry. We describe how we compute the conserved quantities in the center of mass Fermi frame.

6.1 Overview

We can use conservation laws to verify the correctness of the simulation as well as to gain insight into the dynamics of an extended body in curved spacetime. Although, the center of mass worldline describes an approximate center of mass, the use of the center of mass Fermi frame does not cause the conserved quantities to be approximate since the computation of the conserved quantity does not depend on the slice of spacetime being used. We use the center of mass Fermi frame to easily identify parts of the conserved angular momentum with orbital angular momentum and with intrinsic angular momentum. We carry the computations to zeroth order in the acceleration of the observer and second order in \bar{x}^a .

6.2 Rest energy

The rest energy of an elastic body is conserved in curved spacetime independent of any symmetry of the spacetime. Extending the mass current for an elastic body in nonrelativistic elasticity (Eq. (2.8)), we can write the rest energy current for an elastic body in relativistic elasticity as

$$\mathcal{J}^\mu(X(\lambda, \zeta)) = \frac{1}{J} \rho_0 U^\mu \quad (6.1)$$

where $J \equiv \sqrt{f}/\sqrt{\epsilon}$. The factor ρ_0/J is the rest energy per unit physical volume of the distorted body. Since, the rest energy is conserved, we can use any slice of spacetime to compute it. We use a slice of constant center of mass Fermi time \bar{t} . The conserved rest energy is

$$E_{\text{rest}} = - \int_{\bar{t}=\text{const}} d^3 \bar{x} \sqrt{\bar{h}}(\rho_0/\bar{J}) \bar{U}^\mu \bar{n}_\mu \quad (6.2)$$

where $\bar{h} \equiv \det(\bar{g}_{ab})$ and \bar{n}_μ is the unit normal to the $\bar{t} = \text{const}$ surface. The Fermi metric components are (Brown (2019)),

$$\bar{g}_{tt}(\bar{t}, \bar{x}) = -(1 + \bar{A}_a \bar{x}^a)^2 - \bar{R}_{tatb} \big|_0 \bar{x}^a \bar{x}^b + \mathcal{O}(3) \quad (6.3)$$

$$\bar{g}_{ta}(\bar{t}, \bar{x}) = \frac{2}{3} \bar{R}_{abct} \big|_0 \bar{x}^b \bar{x}^c + \mathcal{O}(3) \quad (6.4)$$

$$\bar{g}_{ab}(\bar{t}, \bar{x}) = \delta_{ab} - \frac{1}{3} \bar{R}_{acbd} \big|_0 \bar{x}^c \bar{x}^d + \mathcal{O}(3). \quad (6.5)$$

The components of the unit normal are,

$$\bar{n}_t(\bar{t}, \bar{x}) = -1 - \bar{A}_a \bar{x}^a - \frac{1}{2} \bar{R}_{tatb} \big|_0 \bar{x}^a \bar{x}^b + \mathcal{O}(3) \quad (6.6)$$

$$\bar{n}_a(\bar{t}, \bar{x}) = 0. \quad (6.7)$$

We replace the unit normal components and move the quantities evaluated on the worldline of the observer outside of the integral,

$$E_{\text{rest}} = \int_{\bar{t}=\text{const}} d^3 \bar{x} \left(\sqrt{\bar{h}}(\rho_0/\bar{J}) \bar{U}^t \right) + \bar{A}_a \int_{\bar{t}=\text{const}} d^3 \bar{x} \left(\sqrt{\bar{h}}(\rho_0/\bar{J}) \bar{U}^t \bar{x}^a \right) + \frac{1}{2} \bar{R}_{tatb} \big|_0 \int_{\bar{t}=\text{const}} d^3 \bar{x} \left(\sqrt{\bar{h}}(\rho_0/\bar{J}) \bar{U}^t \bar{x}^a \bar{x}^b \right) + \mathcal{O}(3). \quad (6.8)$$

Though the center of mass has nonzero four-acceleration, we found that the acceleration of the center of mass was small enough so that terms with acceleration in the conserved quantity can be ignored. To numerically compute the rest energy in the Fermi frame, we convert to an integral over matter space,

$$E_{\text{rest}} = \int_{\mathcal{S}} d^3\zeta \left(\det(\bar{X}_{,i}^a) \sqrt{\bar{h}}(\rho_0/\bar{J}) \bar{U}^t \right) + \frac{1}{2} \bar{R}_{tatb} \Big|_0 \int_{\mathcal{S}} d^3\zeta \left(\det(\bar{X}_{,i}^a) \sqrt{\bar{h}}(\rho_0/\bar{J}) \bar{U}^t \bar{x}^a \bar{x}^b \right) + \mathcal{O}(A^1, \bar{x}^3) \quad (6.9)$$

where $\mathcal{O}(A^1, \bar{x}^3)$ denotes terms first order and higher in the acceleration of the center of mass and third order and higher in \bar{x}^a . We then use the Fermi coordinates and velocities computed as described in Chapter 5, the spatial Fermi metric components (Eq. (6.5)) and the discretization in Chapter 4.

6.3 Spacetime with symmetry

A spacetime with symmetry has a Killing vector field ξ^μ . Using the Killing equation $\nabla_\mu \xi_\nu + \nabla_\nu \xi_\mu = 0$, $\nabla_\mu T^{\mu\nu} = 0$ and $T^{\mu\nu} = T^{\nu\mu}$, it can be shown that $\nabla_\mu (T^{\mu\nu} \xi_\nu) = 0$. It follows that

$$Q = \int_{\Sigma} d^3\sigma \sqrt{h} n_\mu T^{\mu\nu} \xi_\nu \quad (6.10)$$

is conserved, where Σ is a spacelike surface with future pointing unit normal, n^μ , and $d^3\sigma \sqrt{h}$ is the volume element on Σ . Therefore, Q is independent of the spacelike surface Σ . Since we can evaluate this conserved quantity using any slice, we use a slice of constant center of mass Fermi coordinate time \bar{t} ,

$$Q = \int_{\bar{t}=\text{const}} d^3\bar{x} \sqrt{\bar{h}} \bar{n}_\mu \bar{T}^{\mu\nu} \bar{\xi}_\nu \quad (6.11)$$

6.3.1 Conservation of energy

The timelike Killing vector field in Schwarzschild coordinates is $\xi^\mu = (1, 0, 0, 0)$. The total conserved energy computed in the Fermi frame is

$$E_{\text{tot}} = \int d^3\bar{x} \bar{n}_\mu \bar{T}^{\mu\nu} \bar{\xi}_\nu \quad (6.12)$$

We subtract the rest energy (Equation 6.2) from the total conserved energy,

$$E_{\text{tot}} - E_{\text{rest}} = \int d^3 \bar{x} \bar{n}_\mu [\bar{T}^{\mu\nu} \bar{\xi}_\nu + (\rho_0 / \bar{J}) \bar{U}^\mu] \quad (6.13)$$

We replace the expression for the SEM tensor of the elastic body $T^{\mu\nu} = 1/J[(\rho_0 + W)U^\mu U^\nu + S^{ij} F_i^\mu F_j^\nu]$ in the conserved energy, $E_{\text{tot}} - E_{\text{rest}}$, and separate it into three parts,

$$\begin{aligned} E_{\text{tot}} - E_{\text{rest}} = & \underbrace{\int d^3 \bar{x} \sqrt{\bar{h}} (\rho_0 / \bar{J}) \bar{n}_\mu \bar{U}^\mu [\bar{U}^\nu \bar{\xi}_\nu + 1]}_{\Sigma(T_{\text{orb}} + T_{\text{int}} + U_{\text{orb}})} \\ & + \underbrace{\int d^3 \bar{x} \sqrt{\bar{h}} (\bar{W} / \bar{J}) \bar{n}_\mu \bar{U}^\mu \bar{U}^\nu \bar{\xi}_\nu}_{\Sigma(U_{\text{int}})} \\ & - \underbrace{\int d^3 \bar{x} \sqrt{\bar{h}} (\bar{S}^{ij} / \bar{J}) \bar{n}_\mu \bar{F}_i^\mu \bar{F}_j^\nu \bar{\xi}_\nu}_{\Sigma(E_{\text{rel}})}. \end{aligned} \quad (6.14)$$

The first part denoted by $\Sigma(T_{\text{orb}} + T_{\text{int}} + U_{\text{orb}})$ is the sum of the orbital and internal kinetic energies and the orbital potential energy of the pieces of the elastic body. The second part, $\Sigma(U_{\text{int}})$ is the sum of the internal potential energy of the pieces of the elastic body. The third part, $\Sigma(E_{\text{rel}})$, is the contribution of spatial stress to the energy.

We can further separate, $\Sigma(T_{\text{orb}} + T_{\text{int}} + U_{\text{orb}})$ into the orbital energies and the internal kinetic energy. We considered three ways of defining the orbital energies. The first way is to consider the deformed elements of the elastic body as point particles with rest energy equal to the rest energy of the deformed elements moving along different worldlines. For a point particle of rest energy, m_0 , and four-velocity, U^μ , the “energy-at-infinity” is $-m_0 U^\mu \xi_\mu$ (Misner et al. (1973)). For a particle following a geodesic, this is a constant and for a particle following a parabolic geodesic $-U^\mu \xi_\mu = 1$. On a Fermi $\bar{t} = \text{const}$ slice, we can compute $-U^\mu \xi_\mu$ for the deformed elements and sum them, we can also do the computation in the Fermi frame. For the first way, we define the orbital energies of the elastic body as

$$\Sigma(T_{\text{orb}} + U_{\text{orb}}) = - \int d^3 \bar{x} \left(\sqrt{\bar{h}} (\rho_0 / \bar{J}) \bar{U}^\mu \bar{\xi}_\mu \right) - E_{\text{rest}}. \quad (6.15)$$

The second way is to consider a point particle of rest energy equal to the elastic body’s rest energy and moving along the worldline of the center of mass of the elastic body. We

compute orbital energies of the center of mass point particle on the Fermi $\bar{t} = \text{const}$ slice with

$$T_{\text{cm}} + U_{\text{cm}} = E_{\text{rest}}(-V^\mu \bar{\xi}_\mu - 1). \quad (6.16)$$

This way of computing the orbital energies is to assume that the orbital energy of an extended body is due to a representative point on the extended body and to consider the remaining energy as internal.

The third way is to consider each deformed piece of the elastic body as point particles and compute their total momentum by approximating the center of mass Fermi metric as flat. Then, we compute the scalar product of the timelike Killing vector evaluated at the center of mass worldline with the total momentum and subtract the rest energy,

$$T_{\text{p}} + U_{\text{p}} = -\bar{\xi}_\mu|_0 \int d^3 \bar{x} \left(\sqrt{\bar{h}}(\rho_o/J) \bar{U}^\mu \right) - E_{\text{rest}}. \quad (6.17)$$

To numerically evaluate Eq. (6.14), we need the Fermi components of the Killing covector $\bar{\xi}_\mu$. The Fermi components of a vector on the Fermi $\bar{t} = \text{const}$ slice given the spacetime components are

$$\begin{aligned} \bar{\xi}^t(\bar{t}, \bar{x}) &= -V_\mu \bar{\xi}^\mu(x) - \bar{\xi}^\mu(x) \Gamma_{\mu\beta}^\alpha|_0 V_\alpha e_a^\beta \bar{x}^a \\ &\quad - \bar{\xi}^\mu(x) \left[\frac{1}{3} \bar{R}_{tabc} e_\mu^c + \frac{1}{2} V_\nu \partial_\mu \Gamma_{\alpha\beta}^\nu e_a^\alpha e_b^\beta \right] \Big|_0 \bar{x}^a \bar{x}^b \\ &\quad + \mathcal{O}(A^1, \bar{x}^3) \end{aligned} \quad (6.18)$$

$$\begin{aligned} \bar{\xi}^a(\bar{t}, \bar{x}) &= \bar{\xi}^\mu(x) e_\mu^a + \bar{\xi}^\mu(x) \Gamma_{\mu\beta}^\alpha|_0 e_\alpha^a e_b^\beta \bar{x}^b \\ &\quad + \bar{\xi}^\mu(x) \left[\frac{1}{3} \bar{R}^a{}_{cbd} e_\mu^d + \frac{1}{2} \partial_\mu \Gamma_{\alpha\beta}^\nu e_\nu^a e_b^\alpha e_c^\beta \right] \Big|_0 \bar{x}^b \bar{x}^c + \mathcal{O}(3) \end{aligned} \quad (6.19)$$

We use the Fermi metric Eqs. (6.3)-(6.5) at the location of the vector to lower the index,

$$\bar{\xi}_t(\bar{t}, \bar{x}) = \bar{g}_{tt}(\bar{t}, \bar{x}) \bar{\xi}^t(\bar{t}, \bar{x}) + \bar{g}_{ta} \bar{\xi}^a(\bar{t}, \bar{x}) \quad (6.20)$$

$$\bar{\xi}_a(\bar{t}, \bar{x}) = \bar{g}_{ta}(\bar{t}, \bar{x}) \bar{\xi}^t(\bar{t}, \bar{x}) + \bar{g}_{ab} \bar{\xi}^b(\bar{t}, \bar{x}), \quad (6.21)$$

and obtain

$$\begin{aligned}\bar{\xi}_t(\bar{t}, \bar{x}) &= V_\mu \xi^\mu(x) + \xi^\mu(x) \Gamma_{\mu\beta}^\alpha \Big|_0 V_\alpha e_a^\beta \bar{x}^a \\ &\quad + \xi^\mu(x) \left[\bar{R}_{tabc} e_\mu^c + \frac{1}{2} V_\nu \partial_\mu \Gamma_{\alpha\beta}^\nu e_a^\alpha e_b^\beta + V_\mu \bar{R}_{tatb} \right] \Big|_0 \bar{x}^a \bar{x}^b \\ &\quad + \mathcal{O}(A^1, \bar{x}^3)\end{aligned}\tag{6.22}$$

$$\begin{aligned}\bar{\xi}_a(\bar{t}, \bar{x}) &= \xi^\mu(x) e_{\mu a} + \xi^\mu(x) \Gamma_{\mu\beta}^\alpha \Big|_0 e_{aa} e_b^\beta \bar{x}^b \\ &\quad + \xi^\mu(x) \left[\frac{2}{3} \bar{R}_{abcd} e_\mu^d + \frac{1}{2} \partial_\mu \Gamma_{\alpha\beta}^\nu e_{\nu a} e_b^\alpha e_c^\beta - \frac{2}{3} V_\mu \bar{R}_{abct} \right] \Big|_0 \bar{x}^b \bar{x}^c \\ &\quad + \mathcal{O}(A^1, \bar{x}^3).\end{aligned}\tag{6.23}$$

After replacing $\bar{\xi}_t$ and $\bar{\xi}_a$ using Eqs. (6.22) and (6.23) in the integral (Eq. (6.14)), since the timelike Killing vector field is $\xi^\mu = (1, 0, 0, 0)$, we move terms such as $V_\mu \xi^\mu(x)$, $\xi^\mu(x) \Gamma_{\mu\beta}^\alpha \Big|_0 V_\alpha e_a^\beta$, etc, out of the integral.

6.3.2 Conservation of angular momentum

The Killing vector field corresponding to spatial rotations in Schwarzschild isotropic coordinates is $\xi^\mu = (0, -y, x, 0)$. Since the spacetime components of the rotational Killing vector field are not constant, we cannot use the procedure described for the timelike Killing vector field. We use the Fermi components of a covector (Brown (2019)),

$$\begin{aligned}\bar{\xi}_t(\bar{t}, \bar{x}) &= V^\mu \xi_\mu \Big|_0 + V^\mu \nabla_\alpha \xi_\mu \Big|_0 e_a^\alpha \bar{x}^a + \frac{1}{2} V^\mu \nabla_\alpha \nabla_\beta \xi_\mu \Big|_0 e_a^\alpha e_b^\beta \bar{x}^a \bar{x}^b + \frac{1}{2} \xi_\nu \Big|_0 R^\nu{}_{abt} \Big|_0 \bar{x}^a \bar{x}^b \\ &\quad + \mathcal{O}(A^1, \bar{x}^3)\end{aligned}\tag{6.24}$$

$$\begin{aligned}\bar{\xi}_c(\bar{t}, \bar{x}) &= e_c^\mu \xi_\mu \Big|_0 + e_c^\mu \nabla_\alpha \xi_\mu \Big|_0 e_a^\alpha e_b^\beta \bar{x}^a \bar{x}^b + \frac{1}{2} e_c^\mu \nabla_\alpha \nabla_\beta \xi_\mu \Big|_0 e_a^\alpha e_b^\beta \bar{x}^a \bar{x}^b + \frac{1}{6} \xi_\nu \Big|_0 R^\nu{}_{abc} \Big|_0 \bar{x}^a \bar{x}^b \\ &\quad + \mathcal{O}(A^1, \bar{x}^3).\end{aligned}\tag{6.25}$$

We replace the Fermi components of the unit normal and the Killing vector field in the conserved charge and separate it into 6 parts,

$$\begin{aligned}
-Q \equiv J_{\text{tot}} = & \underbrace{V^\mu \xi_\mu|_0 \int d^3 \bar{x} \sqrt{\bar{h}} \bar{T}^{tt}}_{J_1} \\
& \underbrace{\xi_\mu|_0 e_a^\mu \int d^3 \bar{x} \sqrt{\bar{h}} \bar{T}^{ta}}_{J_2} \\
& \underbrace{V^\mu \nabla_\alpha \xi_\mu|_0 e_a^\alpha \int d^3 \bar{x} \sqrt{\bar{h}} \bar{x}^a \bar{T}^{tt}}_{J_3} \\
& \underbrace{\nabla_\alpha \xi_\mu|_0 e_a^\mu e_b^\alpha \int d^3 \bar{x} \sqrt{\bar{h}} \bar{x}^b \bar{T}^{ta}}_{J_4} \\
& \underbrace{\frac{1}{2} \left(V^\mu \nabla_\alpha \nabla_\beta \xi_\mu e_b^\beta e_a^\alpha + R^{\nu}{}_{abt} \xi_\nu + \bar{R}_{tatb} V^\mu \xi_\mu \right) \Big|_0 \int d^3 \bar{x} \sqrt{\bar{h}} \bar{x}^a \bar{x}^b \bar{T}^{tt}}_{J_5} \\
& \underbrace{\left(\frac{1}{2} \nabla_\alpha \nabla_\beta \xi_\mu e_a^\mu e_c^\alpha e_b^\beta + \frac{1}{6} R^{\nu}{}_{bca} \xi_\nu + \frac{1}{2} \bar{R}_{tbtc} \xi_\mu e_a^\mu \right) \Big|_0 \int d^3 \bar{x} \sqrt{\bar{h}} \bar{x}^b \bar{x}^c \bar{T}^{ta}}_{J_6} \\
& + \mathcal{O}(A^1, \bar{x}^3). \tag{6.26}
\end{aligned}$$

Since we are computing the quantities in Fermi frame about the approximate center of mass, J_2 and J_3 should be close to zero. We identify J_1 as the orbital angular momentum and J_4 as the spin (intrinsic angular momentum),

$$J_{\text{orbit}} = J_1 \tag{6.27}$$

$$J_{\text{spin}} = J_4. \tag{6.28}$$

In Minkowski spacetime, J_5 and J_6 are zero and the change in the orbital angular momentum is equal to the change in the spin angular momentum. In curved spacetime, with a rotational Killing vector field, the change in the orbital angular momentum is accompanied by a change in the spin angular momentum as well a change in the angular momentum due to second order moments of the SEM tensor, J_5 and J_6 .

CHAPTER

7

MOTION OF A HYPERELASTIC SPHERE IN SCHWARZSCHILD SPACETIME

In this Chapter, we describe the numerical modeling of a hyperelastic sphere in close encounter orbits around a Schwarzschild black hole. We express dimensional quantities in terms of the black hole mass, M .

7.1 Overview

The equations of motion for a hyperelastic sphere in Schwarzschild spacetime depend on four dimensionless parameters: the longitudinal and transverse sound speeds in the elastic body, C_L and C_T ,

$$C_L = \sqrt{\frac{\lambda + 2\mu}{\rho_0}} \quad (7.1)$$

$$C_T = \sqrt{\frac{\mu}{\rho_0}}, \quad (7.2)$$

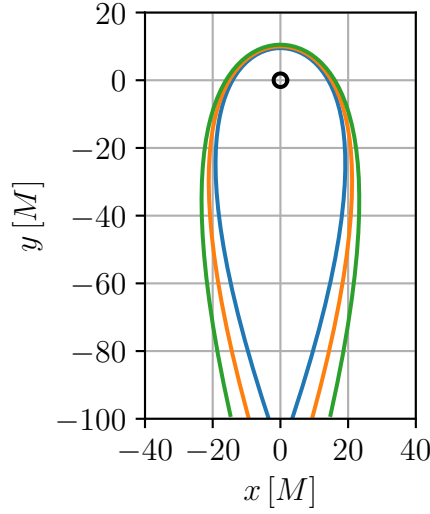


Figure 7.1: Schwarzschild coordinates of the center of mass of the hyperelastic sphere for $\tilde{R}_p = [9.5, 10, 10.5]$. The orbits are anticlockwise in the equatorial plane.

the radius of the sphere, $\tilde{a} = a/M$, and the periastron distance for a chosen parabolic geodesic that we use to obtain initial data, $\tilde{R}_p = R_p/M$. We fix the values of the sound speeds and radius of the sphere to $C_L = 0.01$, $C_T = C_L/\sqrt{3}$ and $\tilde{a} = 0.09976$ and we investigate the effect of closer encounters. For stars, the strength of a tidal encounter is characterized by a dimensionless parameter, η , defined as the ratio of the duration of periastron passage to the hydrodynamic time of the star (Press and Teukolsky (1977), Cheng and Evans (2013)). For an elastic sphere, we define η to be the ratio of the duration of periastron passage to the period of the spheroidal $n = 0, \ell = 2$ oscillation,

$$\eta = \left(\sqrt{R_p^3/M} \right) (\omega_{02}/2\pi). \quad (7.3)$$

Smaller values of η correspond to stronger encounters. Three orbits with $\tilde{R}_p = [9.5, 10, 10.5]$ (shown in Figure 7.1) corresponding to $\eta = [0.71, 0.77, 0.83]$ are simulated. The initial areal radius of the geometric center of the sphere is $100 M$. We use four mesh refinements with $h_{\max} = [a/4, a/8, a/16, a/32]$ to make sure the results have converged.

7.2 Initial data

We consider flat spacetime and a frame in which the elastic body is at rest and relaxed. The elastic body is a sphere in this frame and we find the point which is equidistant from all points on the surface, the geometric center point, C . We assume that point C corresponds to the material point with matter space coordinates $\zeta^i = (0, 0, 0)$. We discretize the matter space assuming that the sphere is relaxed in physical flat spacetime, with the matter space metric equal to the relaxed metric ϵ_{ij} .

At initial time the sphere is at a large areal distance ($100M$) from the black hole and is moving towards it. We assume that the spacetime coordinates and velocity of point C at $t = 0$ correspond to those of a parabolic geodesic. Given a periastron distance R_p and an initial areal radius r , the initial velocity of the parabolic geodesic, dr/dt and $d\phi/dt$, are computed using (Cheng and Evans (2013)):

$$p = \frac{2R_p}{M} \tag{7.4}$$

$$\tilde{L}^2 = \frac{p^2 M^2}{p-4}, \quad \tilde{E} = 1 \tag{7.5}$$

$$f(r) = 1 - \frac{2M}{r}, \quad V(r) = f(r)\left(1 + \frac{\tilde{L}^2}{r^2}\right) \tag{7.6}$$

$$\frac{dt}{d\tau} = \frac{\tilde{E}}{f(r)}, \quad \frac{d\phi}{d\tau} = \frac{\tilde{L}}{r^2}, \quad \frac{dr}{d\tau} = \sqrt{\tilde{E}^2 - V(r)} \tag{7.7}$$

We evolve the spacetime coordinates and velocity of point C for a number of time steps with a very small time step size using the geodesic equations and obtain a Fermi-normal frame carried by point C . A plausible initial condition is that the elastic sphere is in quasistatic equilibrium under elastic and tidal forces in the Fermi-normal frame. The nonrelativistic solution for an elastic sphere in static equilibrium under tidal forces and when the deformation is small is given in Subsection 2.5.2. We compute the displacements for the static solution (Eq. (2.78)), $\vec{\xi}_s(\bar{t}, \zeta)$, for the radius and parameters of the sphere and for each value of the numerically evolved areal radius and angle ϕ of point C . We rotate the displacements so that they correspond to the geometric center of the sphere being located on the x-y plane and at angle ϕ instead of on the z-axis.

We set the spatial Fermi-normal coordinate of each node equal to their relaxed spatial Fermi coordinate plus the displacement,

$$\bar{X}^a(\zeta, \bar{t}) = \bar{X}_R^a(\zeta) + \xi_s^a(\bar{t}, \zeta). \tag{7.8}$$

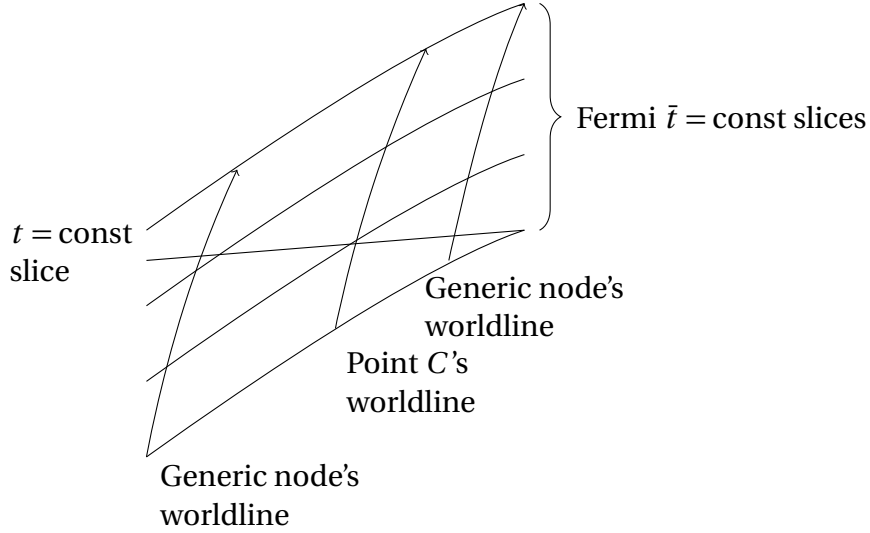


Figure 7.2: Worldline of point C which is a geodesic and of two generic nodes, Fermi $\bar{t} = \text{const}$ slices and a $t = \text{const}$ slice that crosses the worldline of the generic nodes.

We convert the Fermi-normal coordinates on the $\bar{t} = \text{const}$ slices (shown in Figure 7.2) to spacetime coordinates using Eq. (5.8). We then find a $t = \text{const}$ slice that crosses the worldlines of all nodes and find the spacetime coordinates and velocities on this slice by interpolation and finite difference of the closest known spacetime coordinate values and use the values on the $t = \text{const}$ slice as initial coordinate and velocities for the evolution.

7.3 Deformation of sphere as seen in the Fermi frame

As the sphere approaches the black hole, it is stretched in the direction of the black hole and compressed in the transverse direction. As it moves away from the black hole, it oscillates and also has some spin. Figure 7.4 shows snapshots of the spatial Fermi coordinates of the sphere in the fiducial Fermi frame at different points along the orbit for the $\tilde{R}_p = 9.5$ orbit. (Note: the Fermi frame is initially aligned with the black hole frame but slowly rotates with respect to the latter as it is Fermi-Walker transported along the orbit.) We also made these snapshots in the center of mass Fermi frame but there is no visible difference with the snapshots in the fiducial Fermi frame. There is a lag between the direction of the tidal field and direction of the bulge on the sphere (see snapshot (3) in Figure 7.4). We colored cells on surface of the sphere in red and observed that the colored cells do not return to their original $\bar{\phi}$ angle after oscillations. Figure 7.5 shows the angle in the fiducial Fermi

frame for two different nodes for the $\tilde{R}_p = 9.5$ orbit.

7.4 Deviation of the center of mass

As the extended body approaches the black hole it is deformed and its second mass moment couples with the octupole tide causing the center of mass to deviate from a geodesic (Cheng and Evans (2013)). We observe that the center of mass (computed using the procedure in 5.3.3) deviates in the \tilde{x}^1 and \tilde{x}^2 directions in the geodesic Fermi frame (shown for the three orbits on Figure 7.6). As \tilde{R}_p decreases, the deviation increases in an almost quadratic way. For the $\tilde{R}_p = 9.5$ orbit, the deviation in the \tilde{x}^1 at the end is about one tenth of the radius of the sphere.

7.5 Energy

We first compute the rest energy in the center of mass Fermi frame using the procedure described in Section 6.2. We found that the rest energy (Figure 7.7) is conserved to 9 orders of magnitude close to periastron ($-50 M < \tilde{t} < 50 M$) and to 13 orders of magnitude further from the black hole. We obtain less orders of magnitude of conservation close to periastron due to ignoring higher order terms in \tilde{x}^a and in the acceleration of the center of mass in computing the Fermi quantities.

As described in Subsection 6.3.1, total energy is conserved due to the timelike Killing vector field in Schwarzschild spacetime. The total energy in the simulation is conserved to 9 orders of magnitude at the of the simulation as shown in Figure 7.8. We subtract the rest energy from the total energy and separate it into three parts as explained in Subsection 6.3.1. Figure 7.10 shows fractional change in total energy minus the rest energy from initial time showing to its numerical conservation. Figure 7.11 shows the three parts of $E_{\text{tot}} - E_{\text{rest}}$ computed in the center of mass Fermi frame for the $\tilde{R}_p = 9.5$ orbit. The contribution of the spatial stress to the energy, $\sum(E_{\text{rel}})$, is observed to be very small. The decrease in the orbital energies plus internal kinetic energies, $\sum(T_{\text{orb}} + T_{\text{int}} + U_{\text{orb}})$, is accompanied by an increase in the internal potential energy of the elastic sphere. The internal potential energy, $\sum(U_{\text{int}})$ is initially close to zero, as the elastic sphere is tidally deformed it increases to maximum value and then decreases and has an average positive shift from zero as the sphere moves away from the black hole. The elastic sphere has a ellipsoidal shape, with the bulge rotating counter-clockwise in the $x y$ plane. Since it is always deformed after moving away from the

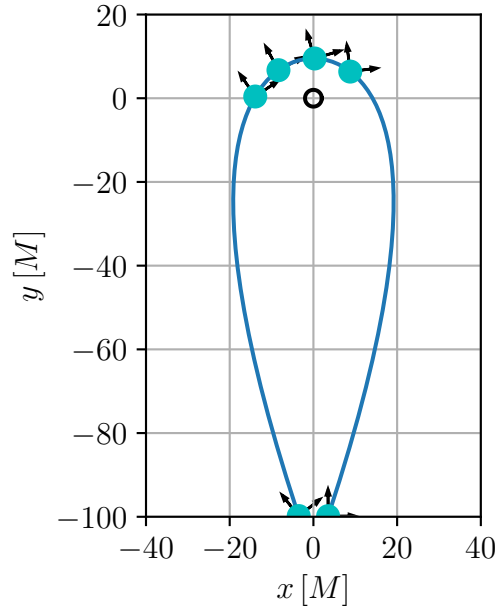
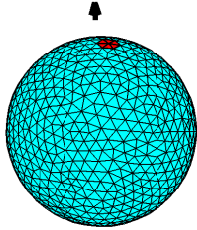
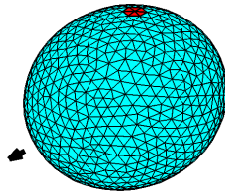


Figure 7.3: Points along the orbit at which the spatial Fermi coordinates of the sphere are plotted. The Fermi frame directions are also shown.

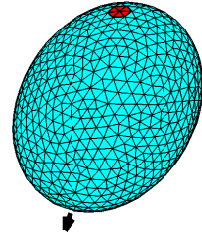
(1) $\bar{t} = -551.7 M$



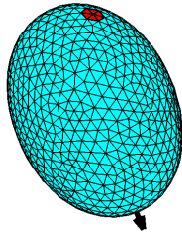
(2) $\bar{t} = -19 M$



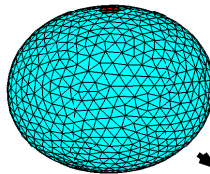
(3) $\bar{t} = -0.5 M$



(4) $\bar{t} = 17.9 M$



(5) $\bar{t} = 37.2 M$



(6) $\bar{t} = 551.5 M$

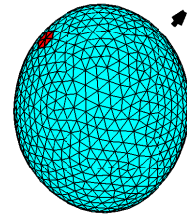


Figure 7.4: Top view in the Fermi frame. (1) to (6) correspond to successive points marked along the orbit. (2) to (5) are at constant intervals of t . The period of $n = 0, \ell = 2$ analytical normal modes is $41.2M$. Between (5) and (6), the sphere undergoes about 12 oscillations. The arrow shows the direction to the black hole.

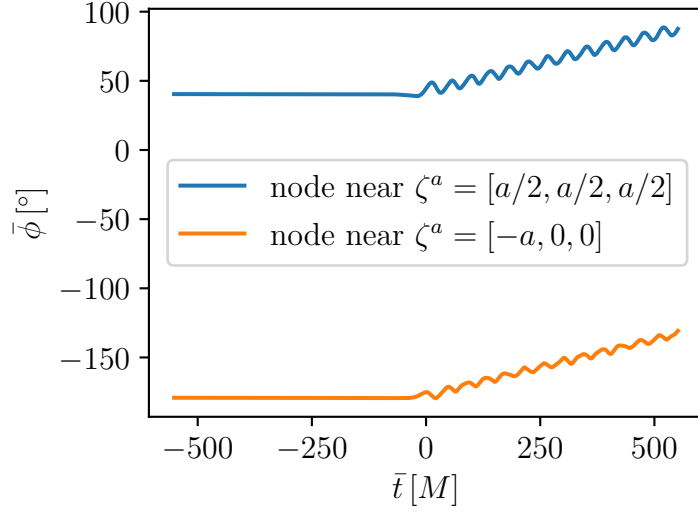


Figure 7.5: Angle of two nodes in the fiducial Fermi frame for the $\tilde{R}_p = 9.5$ orbit.

black hole, this explains the average positive shift from zero of $\sum(U_{\text{int}})$.

We further separate $\sum(T_{\text{orb}} + T_{\text{int}} + U_{\text{orb}})$ as described in Subsection 6.3.1 into orbital energies and internal kinetic energy of the elastic sphere. Figures 7.12, 7.13 and 7.14 show the results of the three ways of carrying out the separation by identifying orbital energies, as $\sum(T_{\text{orb}} + U_{\text{orb}})$ using Equation 6.15, $T_{\text{cm}} + U_{\text{cm}}$ using Equation 6.16 and $T_p + U_p$ using Eq. (6.17). All three ways agree further way from periastron.

Further away they show that the resulting internal kinetic energy of the sphere has an average positive shift equal to that of the internal potential energy. The almost constant kinetic energy that does not go to zero is understood better after decomposing the deformation of the sphere into normal modes (in Section 7.7) and finding that the oscillation of the sphere is the result of the $n = 0, \ell = 2, m = -2$ and the $n = 0, \ell = 2, m = 2$ modes with almost the same amplitude at 90° phase difference. The virial theorem applied to a harmonic oscillator with potential $(1/2)kx^2$, implies that the average kinetic energy is equal to the average potential energy. We observe that the internal potential energy of the sphere has about the same positive shift as the internal kinetic energy and therefore the internal potential energy function of the sphere has the same form as the harmonic oscillator. The small and opposite wiggles in the internal kinetic and potential energies visible on the plots are perhaps due to the amplitude of these modes being slightly different.

Using the average change in angle $\bar{\phi}$ of the nodes as a function \bar{t} in the fiducial Fermi

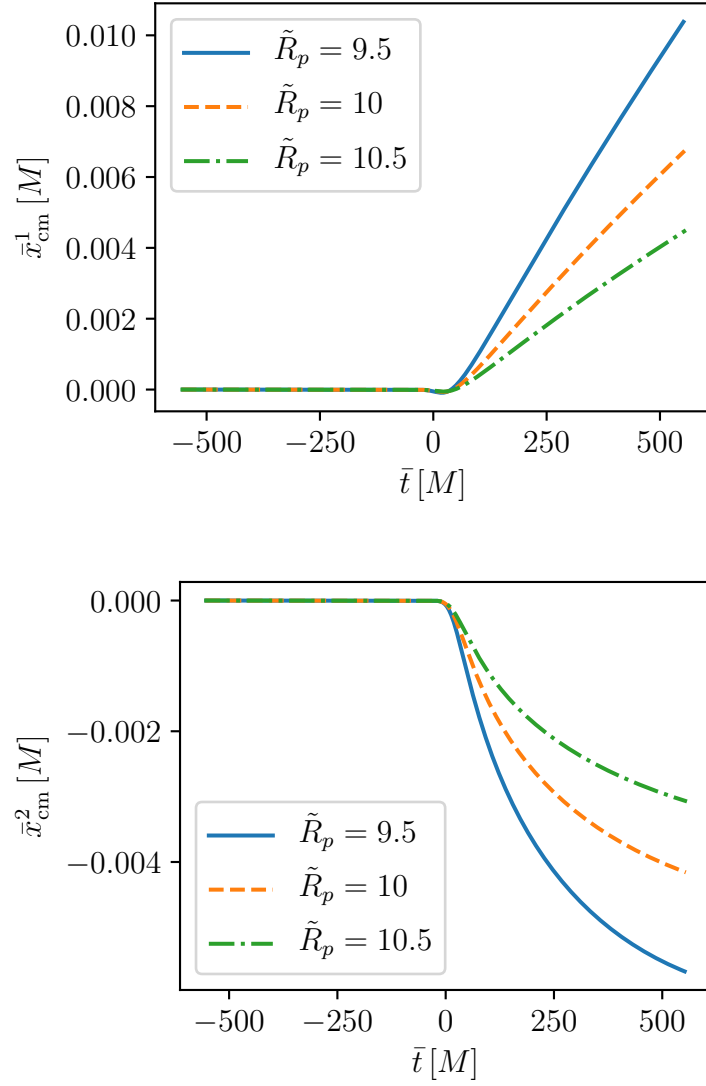


Figure 7.6: Deflection of the center of mass in the \tilde{x}^1 and \tilde{x}^2 directions in the geodesic Fermi frame for $\tilde{R}_p = [9.5, 10, 10.5]$.

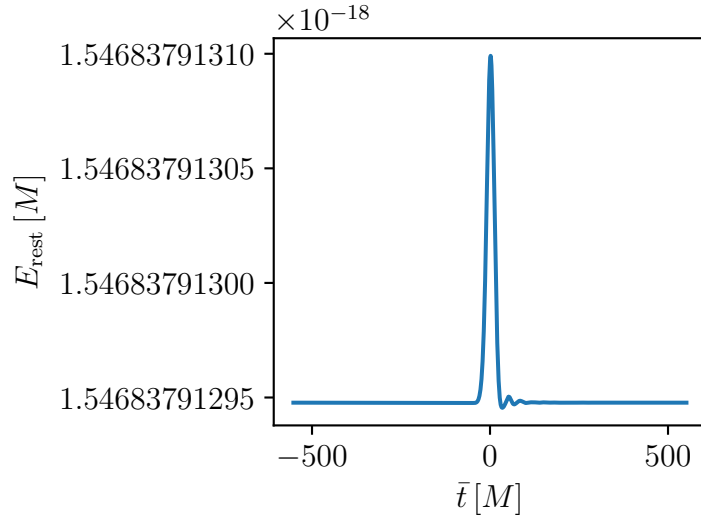


Figure 7.7: The rest energy, E_{rest} , is conserved to 9 orders of magnitude close to periastron and 13 orders of magnitude far from the black hole for $\tilde{R}_p = 9.5$ and for the mesh refinement $h_{\text{max}} = a/16$.

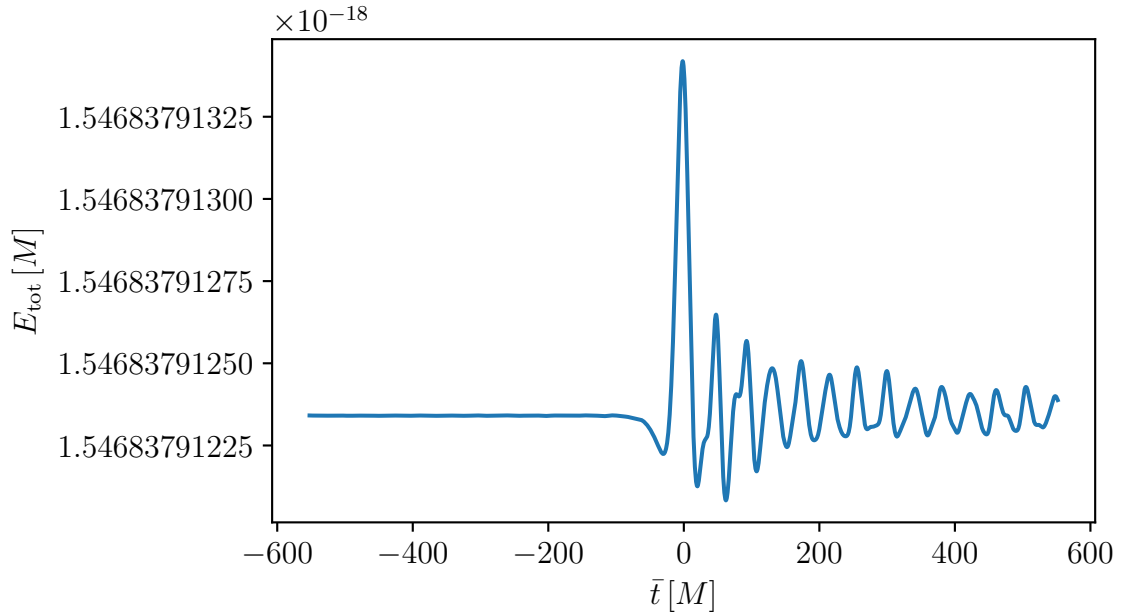


Figure 7.8: The total energy, E_{tot} , (using Equation 6.12), is conserved to 9 orders of magnitude at the end of the simulation. This shows the result for $\tilde{R}_p = 9.5$ and for the mesh refinement $h_{\text{max}} = a/16$.

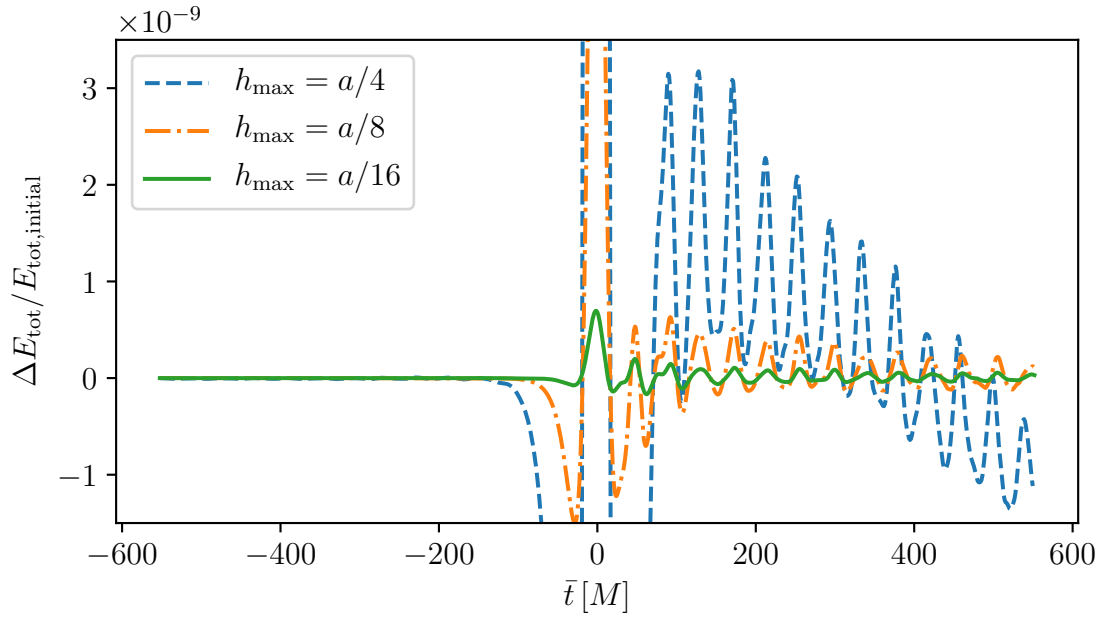


Figure 7.9: The fractional change in the theoretically conserved total energy, E_{tot} , from initial time for three different mesh refinements. This is a plot zoom to focus on the behaviour away from periastron.

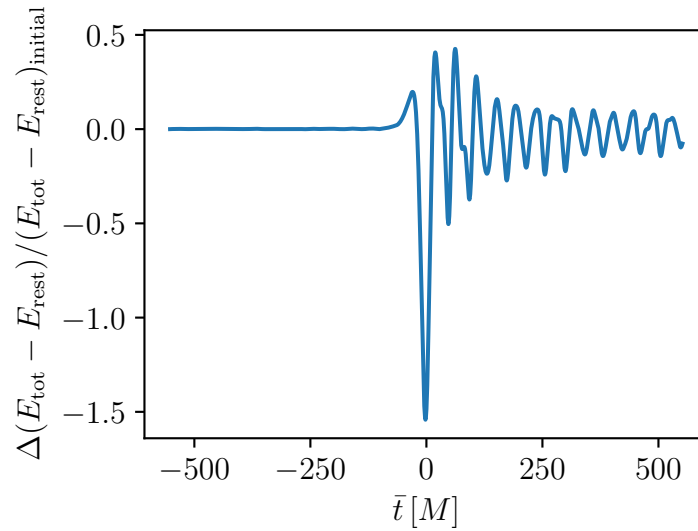


Figure 7.10: The fractional change in the theoretically conserved energy, $E_{\text{tot}} - E_{\text{rest}}$, from initial time for $h_{\text{max}} = a/16$.

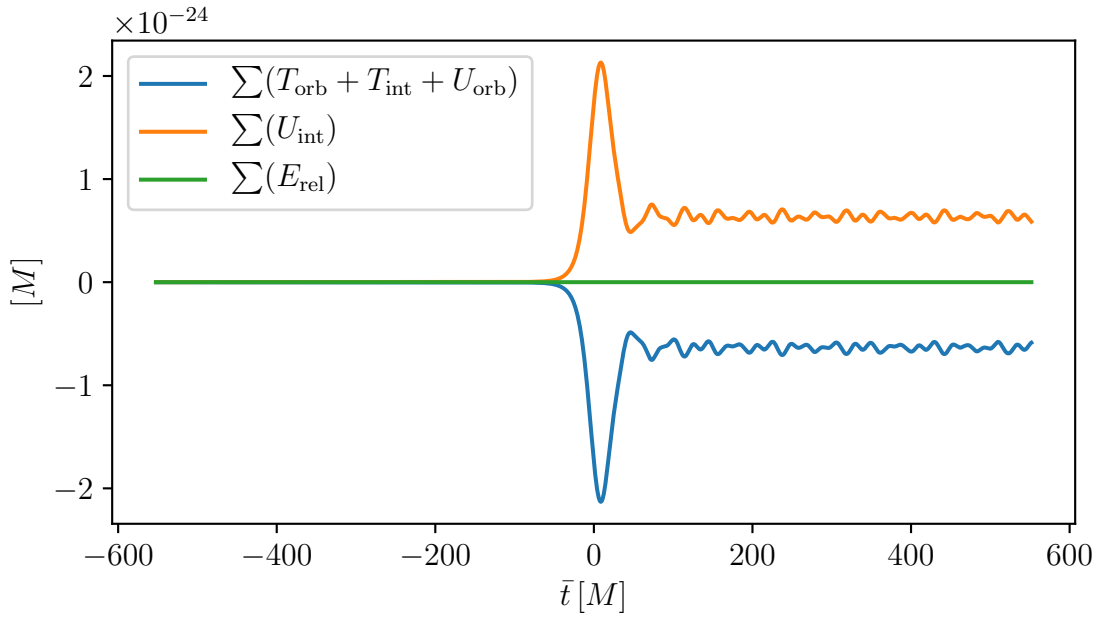


Figure 7.11: Separation of the conserved energy, $E_{\text{tot}} - E_{\text{rest}}$, into three parts for the $\tilde{R}_p = 9.5$ orbit.

frame after the encounter, we compute the average angular frequency and estimate the Newtonian rotational kinetic energy for the $\tilde{R}_p = 9.5$ orbit to be around $6 \times 10^{-27} M^2$ and therefore rotational kinetic energy contributes a very small amount to the observed internal kinetic energy.

The increase in the internal kinetic and potential energy is at the expense of the orbital energy which becomes negative. The orbit changes from a unbound parabolic orbit to a closed orbit.

The three ways of computing the orbital energies lead to different values of the internal kinetic energy close to periastron. The method that leads to an internal energy of the elastic sphere that is always positive is using $\sum(T_{\text{orb}} + U_{\text{orb}})$. Using $T_{\text{cm}} + U_{\text{cm}}$, the orbital energies display less oscillations around $\bar{t} = 70 M$.

7.6 Angular momentum

The deviation of the center of mass in the geodesic Fermi-normal frame implies a change in the orbital angular momentum of the elastic sphere. As described in Subsection 6.3.2, total

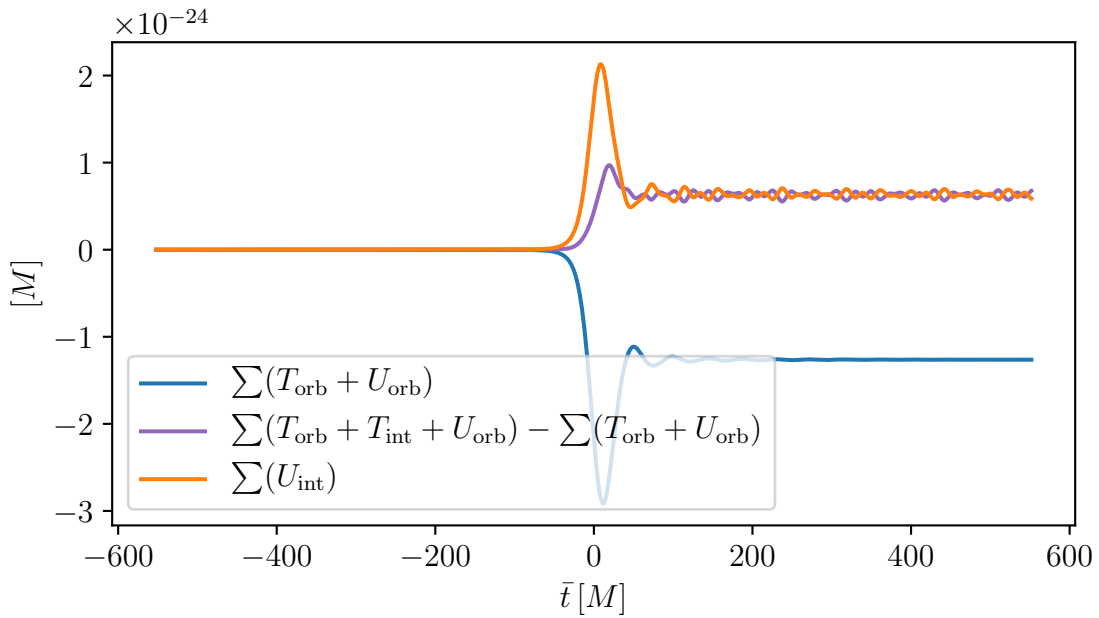


Figure 7.12: First way of computing the orbital energies of the elastic sphere as $\sum(T_{\text{orb}} + U_{\text{orb}})$ and subtracting $\sum(T_{\text{orb}} + U_{\text{orb}})$ from $\sum(T_{\text{orb}} + T_{\text{int}} + U_{\text{orb}})$ to obtain the internal kinetic energy. The plot shows the results for $\tilde{R}_p = 9.5$.

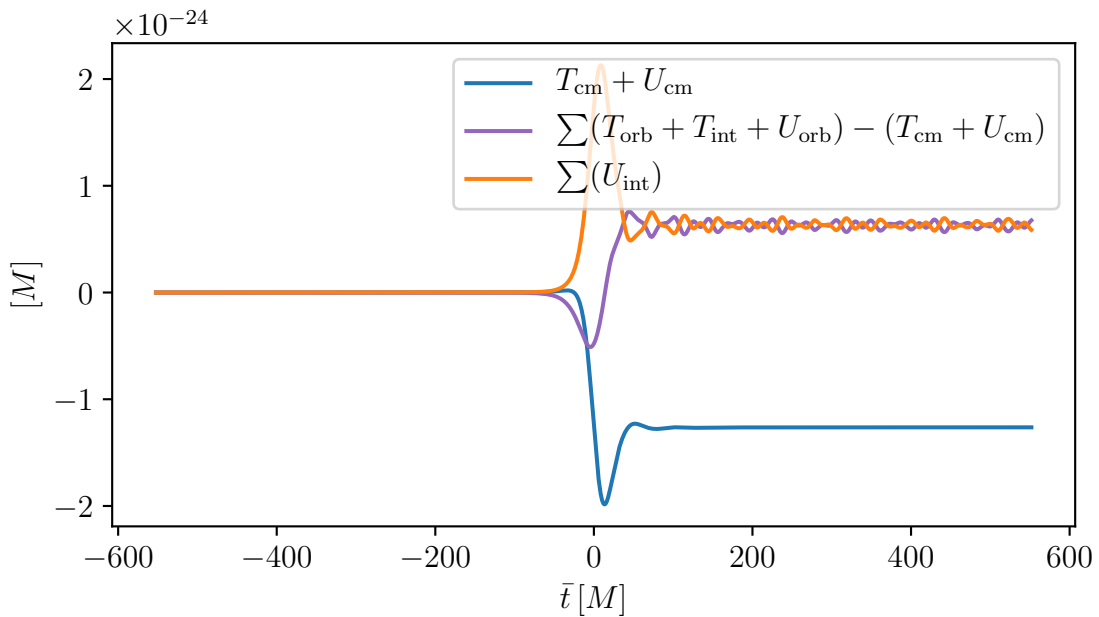


Figure 7.13: Second way of computing the orbital energies of the elastic sphere as $\sum(T_{\text{cm}} + U_{\text{cm}})$ and subtracting $\sum(T_{\text{cm}} + U_{\text{cm}})$ from $\sum(T_{\text{orb}} + T_{\text{int}} + U_{\text{orb}})$ to obtain the internal kinetic energy. The plot shows the results for $\tilde{R}_p = 9.5$.

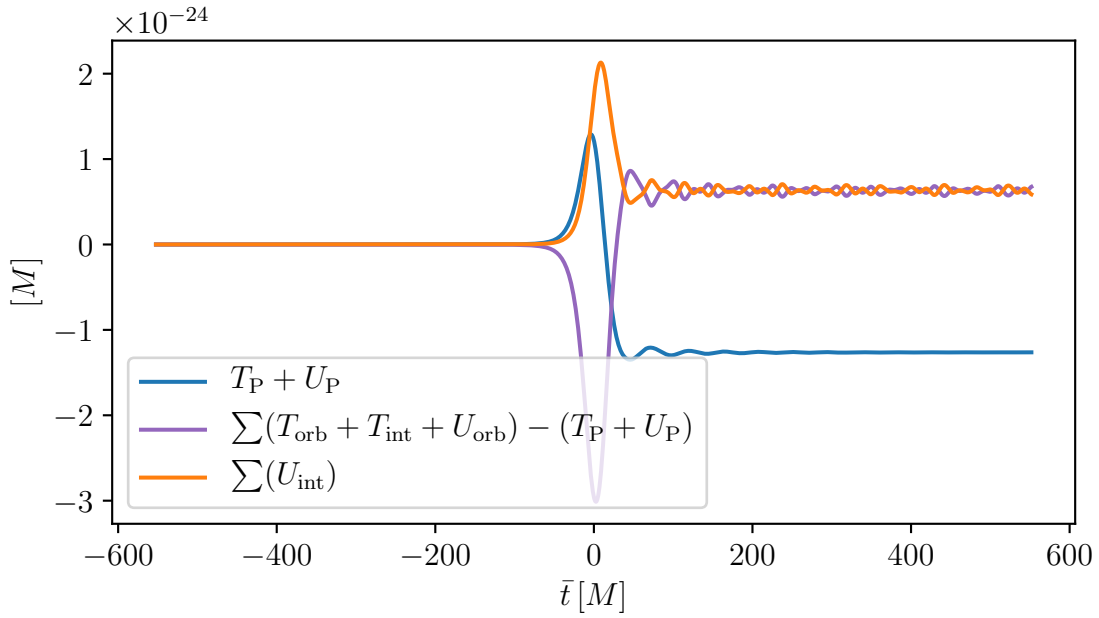


Figure 7.14: Third way of computing the orbital energies of the elastic sphere as $\sum(T_P + U_P)$ and subtracting $\sum(T_P + U_P)$ from $\sum(T_{\text{orb}} + T_{\text{int}} + U_{\text{orb}})$ to obtain the internal kinetic energy. The plot shows the results for $\tilde{R}_p = 9.5$.

angular momentum is conserved in Schwarzschild spacetime because of the Killing vector field corresponding to rotations. The total angular momentum is conserved numerically to 7 orders of magnitude as shown in Figure 7.15. We compute the parts of conserved angular momentum in Eq. (6.26) in the center of mass Fermi frame using the procedure described in Subsection 6.3.2. The different parts of J_{tot} are shown in Figure 7.17. As expected, since the computation is in the center of mass Fermi frame, J_2 and J_3 both remained close to zero. We observed that J_6 was also very small. We observed J_5 to acquire a small negative value close to periastron, which goes to zero as the elastic sphere moves away from the black hole. The spin of the elastic sphere, J_{spin} is initially close to zero, increases rapidly as it moves to the periastron, then decreases rapidly and settles on a constant value as the sphere moves away from the black hole. The change in spin is due to the misalignment of the direction of the deformation of the sphere and the direction to the black hole (Cheng and Evans (2013)) (as seen on snapshot (3) in Figure 7.4), which results in a torque on the sphere.

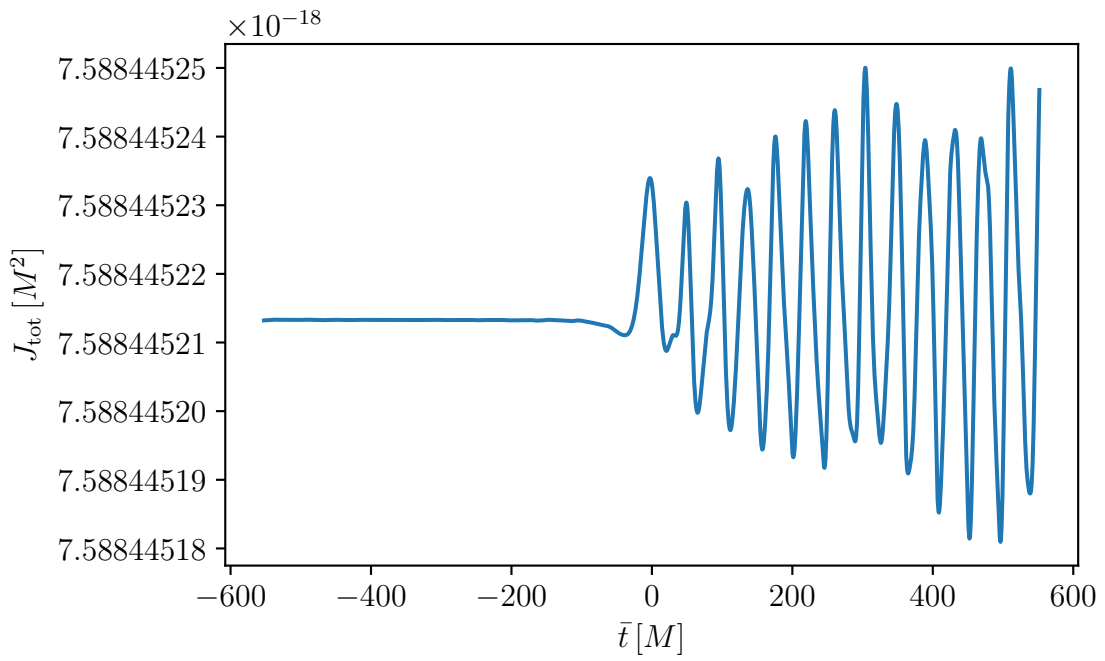


Figure 7.15: The total angular momentum J_{tot} (using Equation 6.26) computed in the center of mass Fermi frame is conserved to 7 orders of magnitude. This shows the result for the $\tilde{R}_p = 9.5$ orbit and for the mesh refinement $h_{\text{max}} = a/16$.

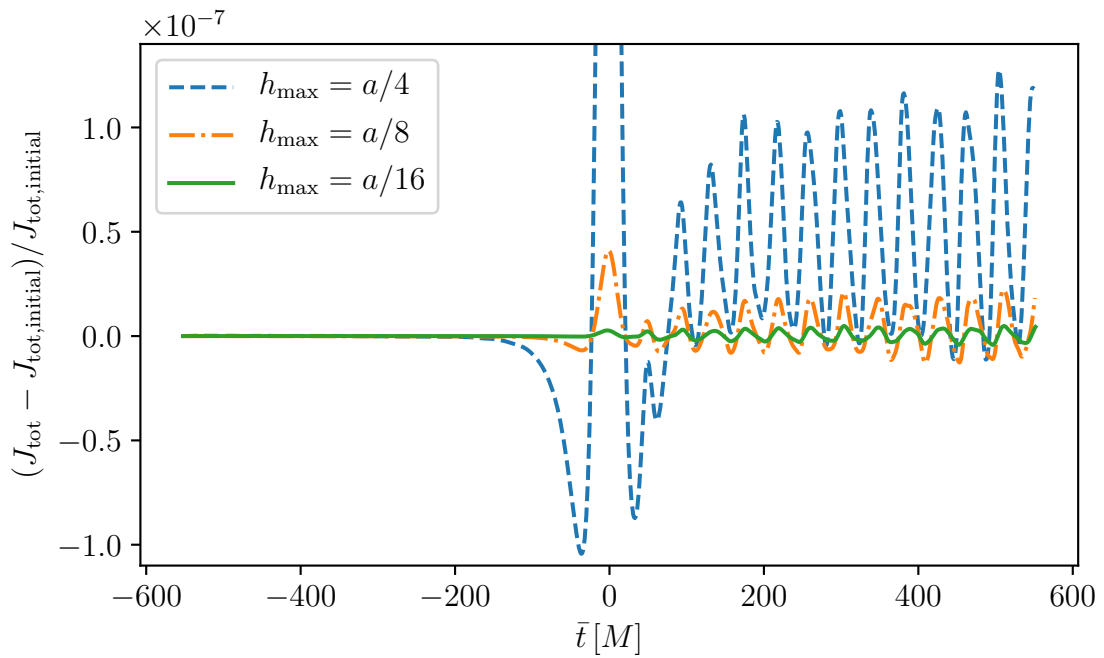


Figure 7.16: The fractional change in the total angular momentum, J_{tot} , from initial time for three different mesh refinements. This is a plot zoom to focus on the behaviour away from periastron.

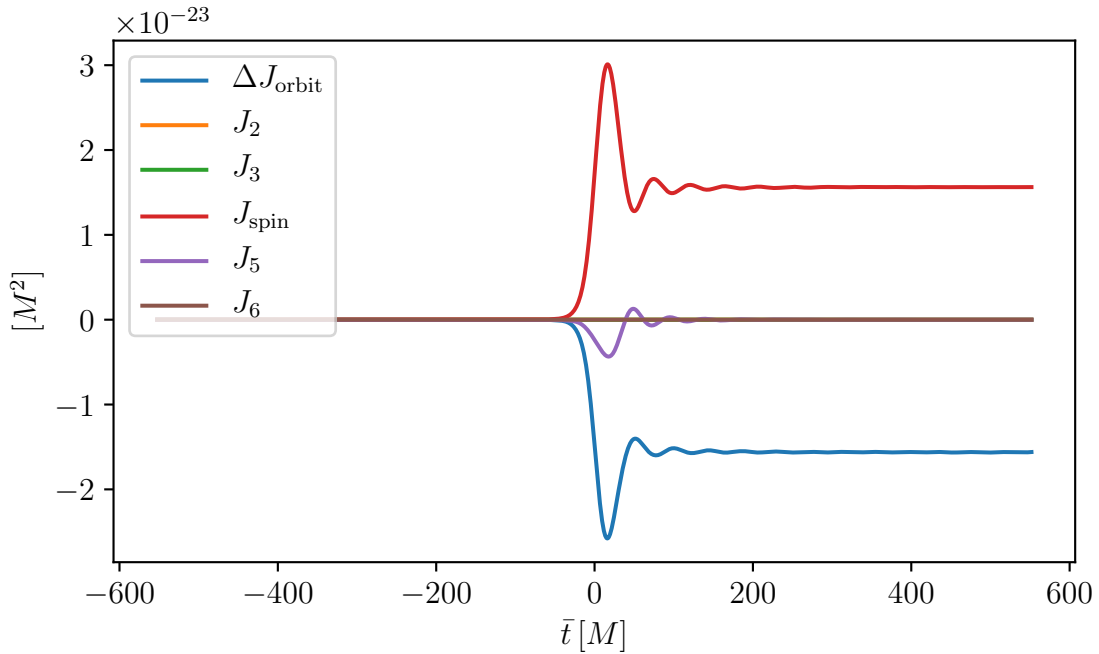


Figure 7.17: Parts of the conserved angular momentum computed in the center of mass Fermi frame for the $\tilde{R}_p = 9.5$ orbit. For J_{orbit} , we plot the change from the initial value.

7.7 Decomposition into normal modes

The deformation of the sphere can be observed in Figure 7.4. For snapshot (5), the length of the longest principle axis of the ellipsoid is around $0.215M$ which gives a deformation of about 7.8 per cent. With this value of the deformation we expect to see some nonlinear effects when analysing the oscillations of the sphere using the small deformation normal mode oscillations.

The average frequency of rotation of the sphere in the Fermi frame is around 0.009 times the nonrelativistic $n = 0, \ell = 2$ analytical spheroidal mode oscillation frequency. Since the sphere is spinning very slowly, we estimate that Coriolis and centrifugal forces will be very small. However, if we obtain the displacement of a node from its relaxed position in the fiducial Fermi frame, we find that the displacement keeps increasing with time due to the rotation. Therefore, we compute the displacements in a Fermi frame rotating with the elastic sphere. We compute the average change in $\bar{\phi}$ angle in the fiducial Fermi frame at each time step and rotate the fiducial Fermi frame by this angle to obtain a rotating Fermi frame.

The spatial part of the nonrelativistic normal modes of a free solid elastic sphere (which can be divided into spheroidal and torsional modes), described in Subsection 2.5.1, can be used as a basis to express a generic spatial displacement field. We focus on the spheroidal modes. The observed displacements of the nodes in the rotating fiducial frame at time \bar{t} can be expanded as

$$\vec{\xi}(\bar{t}, \zeta) = \sum_{n\ell m} C_{n\ell m}(\bar{t}) \vec{\Xi}_{n\ell m}(\zeta) + \dots \quad (7.9)$$

where $\vec{\Xi}_{n\ell m}(\zeta)$ are spatial part of the spheroidal normal and have been normalized such that

$$\int_S d^3\zeta \sqrt{\epsilon} \vec{\Xi}_{n\ell m} \cdot \vec{\Xi}_{n'\ell'm'} = \delta_{nn'} \delta_{\ell\ell'} \delta_{mm'}. \quad (7.10)$$

At each Fermi time step, we numerically evaluate the following integral to obtain the time dependent decomposition coefficients, $C_{n\ell m}(\bar{t})$, for each spheroidal mode,

$$C_{n\ell m}(\bar{t}) = \int_S d^3\zeta \sqrt{\epsilon} \vec{\xi}(\bar{t}, \zeta) \cdot \vec{\Xi}_{n\ell m}(\zeta). \quad (7.11)$$

Away from the black hole, $C_{n\ell m}(\bar{t})$ for most modes have a sinusoidal variation in time with frequencies close to the analytical frequencies.

7.7.1 $n = 0, \ell = 0$ and $n = 0, \ell = 2, m = [0, \pm 2]$

The four modes having the highest amplitude for the decomposition coefficient are the $n = 0, \ell = 2, m = [0, \pm 2]$ and the $n = 0, \ell = 0$ modes (Figure 7.18). The $n = 0, \ell = 0$ and $n = 0, \ell = 2, m = 0$ oscillations are observed to occur about an equilibrium which is positively shifted from zero. $C_{00} > 0$ corresponds to the sphere being radially compressed and $C_{020} > 0$ corresponds to the sphere having a prolate shape. Expansion of the Newtonian potential in terms of spherical harmonics starts at $\ell = 2$ and if the amplitude of the oscillations were small, then the $\ell = 0$ mode would not be excited. Since the sphere has a large deformation in the $n = 0, \ell = 2, m = \pm 2$ modes, the nonlinear elasticity terms induce a constant radial compression and prolate shape of the sphere which explains the positive shift. C_{022} and C_{02-2} have a 90° phase difference corresponding to circular polarization which rotates counterclockwise.

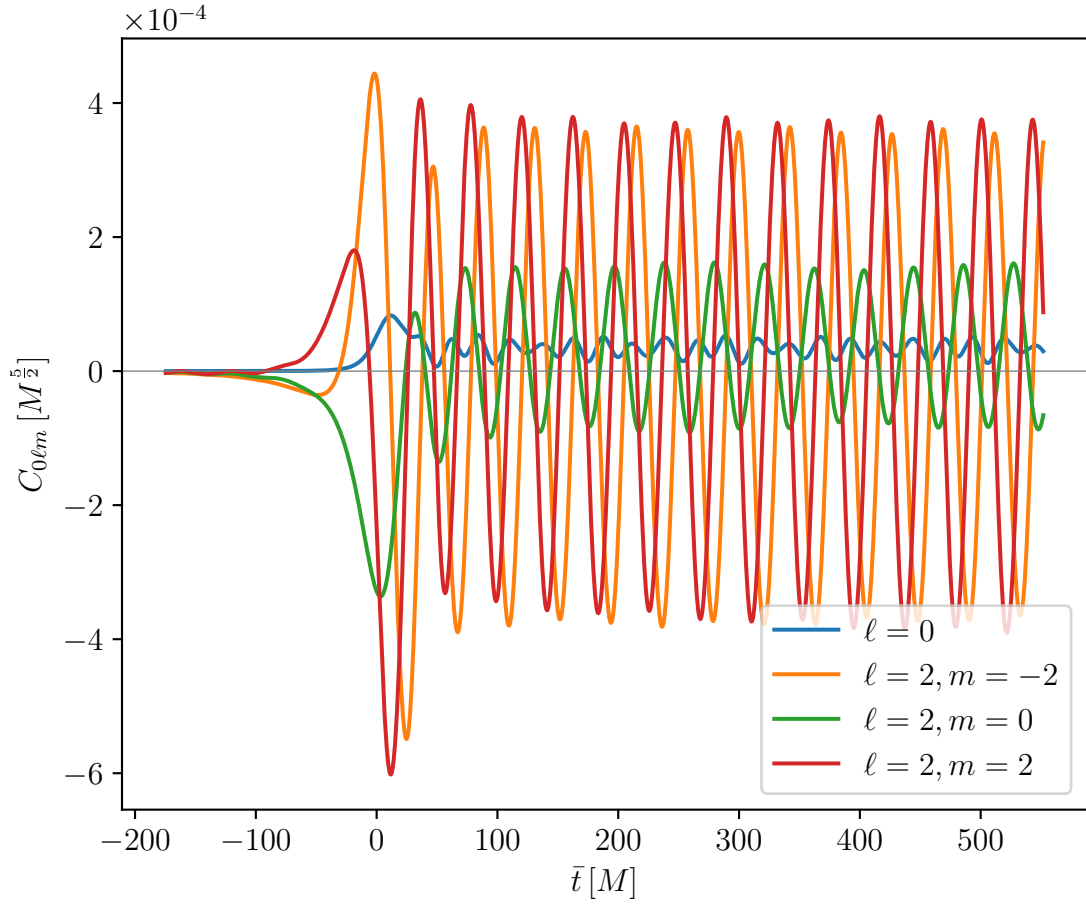


Figure 7.18: Decomposition coefficient as a function of proper time of the fiducial node, $\tilde{R}_p = 9.5$, $n = 0, \ell = 0$ and $n = 0, \ell = 2, m = [0, \pm 2]$.

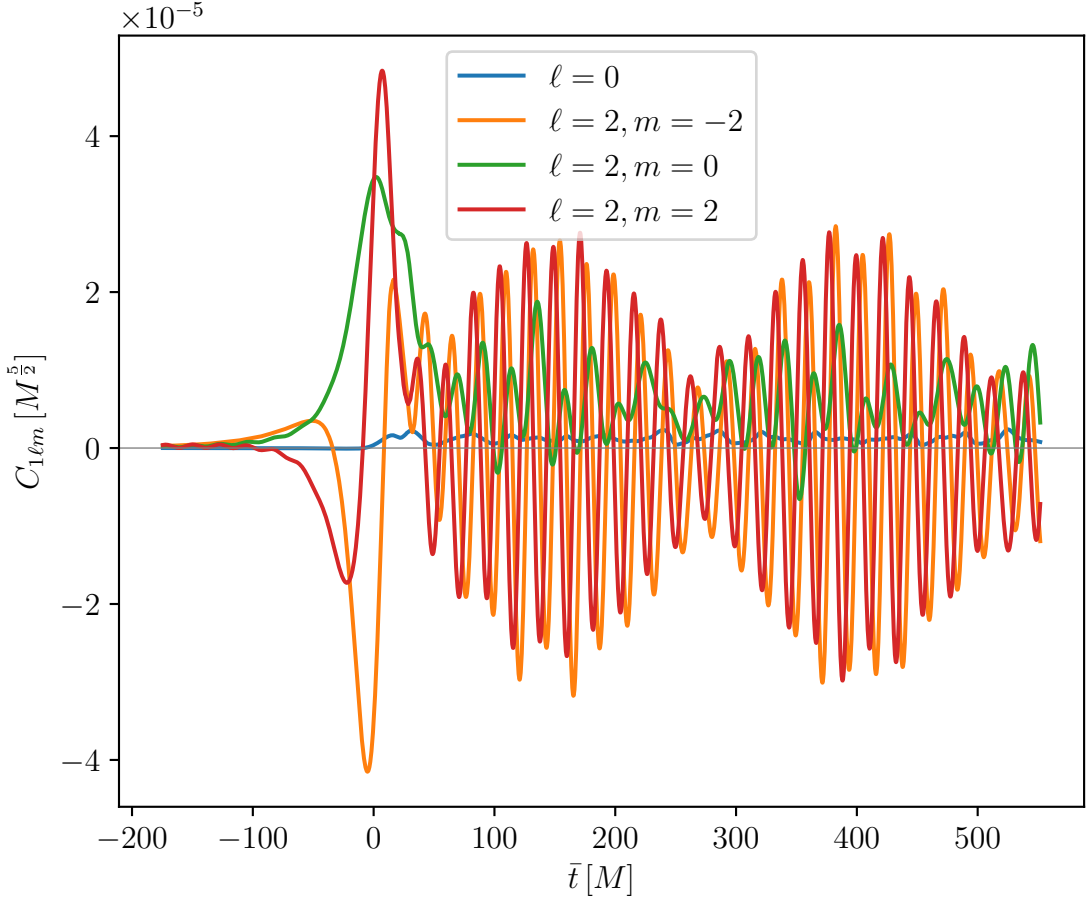


Figure 7.19: Decomposition coefficient as a function of proper time of the fiducial node, $\tilde{R}_p = 9.5$, $n = 1, \ell = 0$ and $n = 1, \ell = 2, m = [0, \pm 2]$.

7.7.2 $n = 1, \ell = 0$ and $n = 1, \ell = 2, m = [0, \pm 2]$

The decomposition coefficients for the $n = 1, \ell = 0$ and the $n = 1, \ell = 2, m = [0, \pm 2]$ modes are about 10 times smaller than the $n = 0$ modes (Figure 7.19). The $n = 1, \ell = 2, m = \pm 2$ oscillations also display an envelope. We performed a test in flat spacetime, with the nodes of the sphere having initial displacements and velocities corresponding to the normal modes in Figures 7.18 and 7.19 and also observed an envelope for $n = 1, \ell = 2, m = \pm 2$ mode decomposition coefficients. However, we noticed that there is no envelope if we do not include the $n = 0, \ell = 2, m = 0$ mode initially. Hence we conclude that the envelope is caused by nonlinear coupling between the $n = 0, \ell = 2, m = 0$ and $n = 1, \ell = 2, m = \pm 2$ modes.

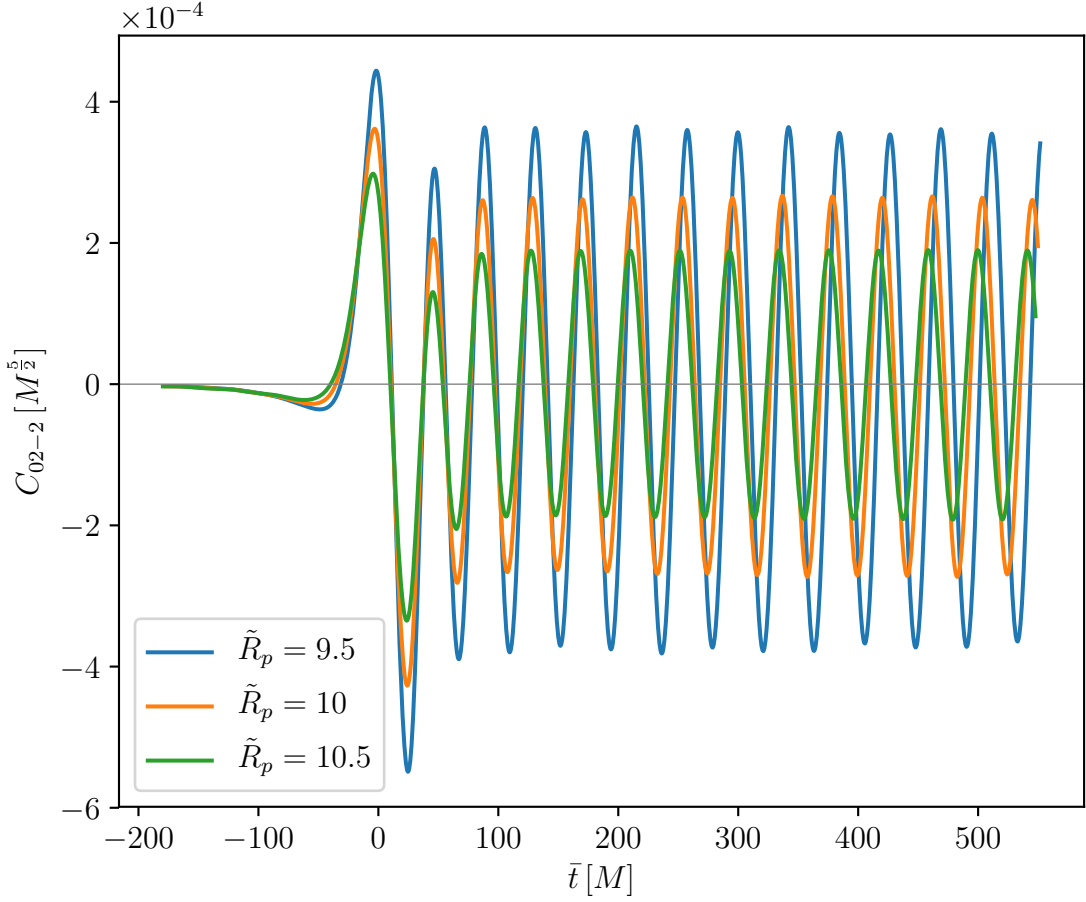


Figure 7.20: Decomposition coefficient for $n = 0, \ell = 2, m = -2$ as a function of proper time of the fiducial node for the three orbits, $\tilde{R}_p = [9.5, 10, 10.5]$.

7.7.3 $\tilde{R}_p = [9.5, 10, 10.5]$

Figures 7.20, 7.21 and 7.22 show C_{02-2} , C_{12-2} and C_{03-3} respectively for linear decreases in \tilde{R}_p . The increase in the maximum value of C_{02-2} going from $\tilde{R}_p = 10$ to $\tilde{R}_p = 9.5$ is 1.3 times the increase going, from $\tilde{R}_p = 10.5$ to $\tilde{R}_p = 10$. However, for C_{12-2} , the increase is 2.1 times. $C_{03\pm 3}$ (shown for $m = -3$ in Figure 7.22) are 2 orders of magnitude smaller than $C_{12\pm 2}$ and 3 orders of magnitude times smaller than $C_{02\pm 2}$.

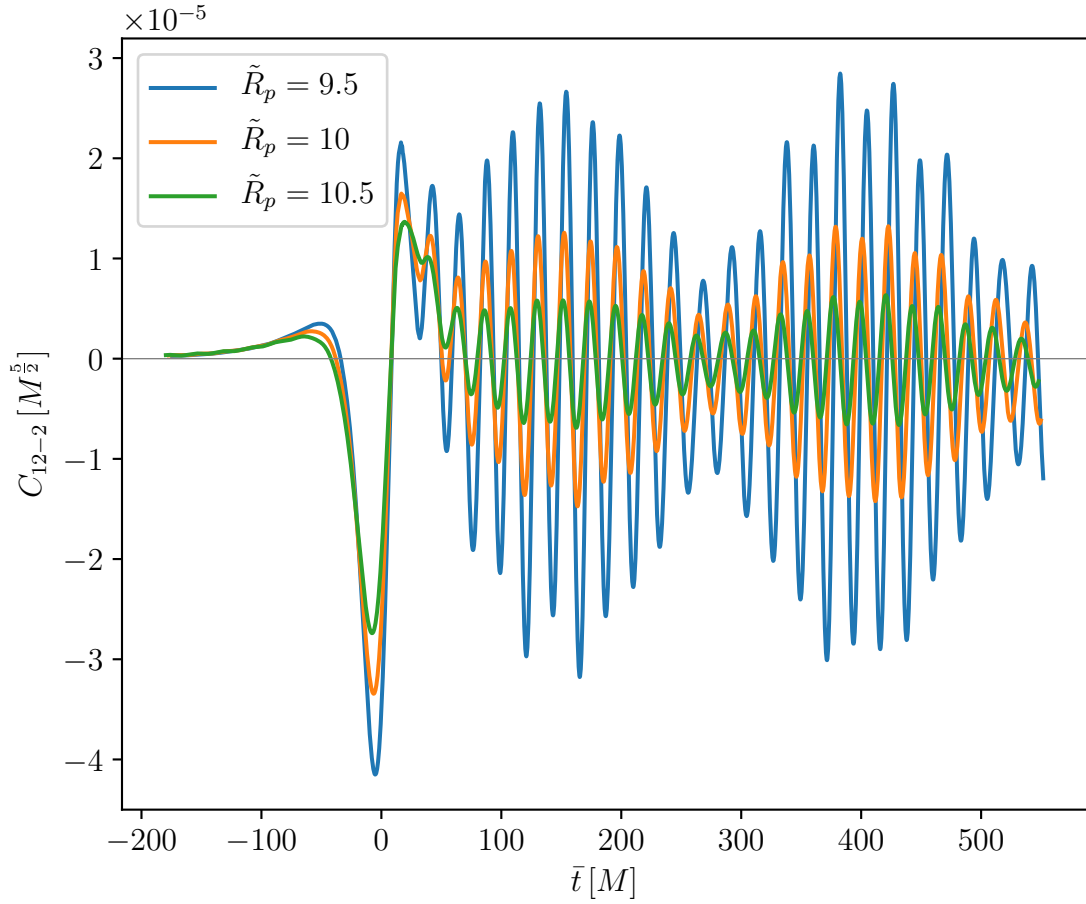


Figure 7.21: Decomposition coefficient for $n = 1, \ell = 2, m = -2$ as a function of proper time of the fiducial node for the three orbits, $\tilde{R}_p = [9.5, 10, 10.5]$.

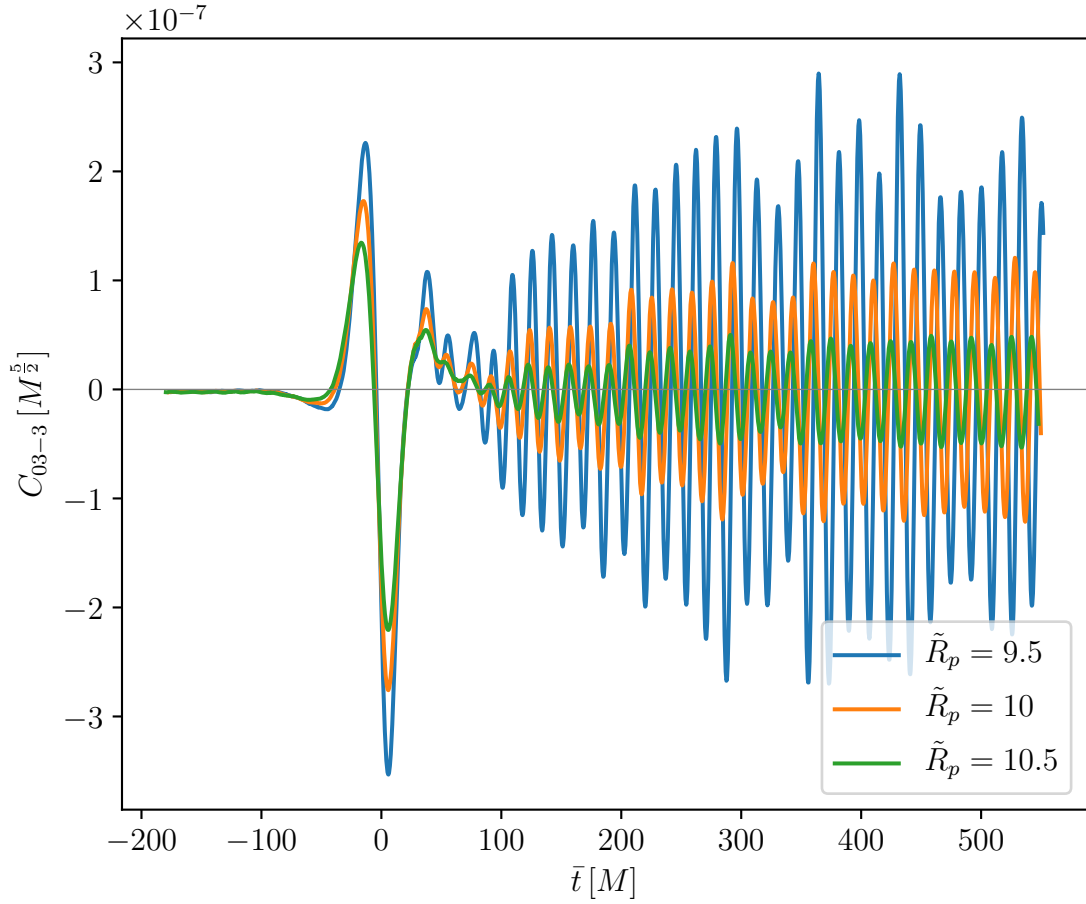


Figure 7.22: Decomposition coefficient for $n = 0, \ell = 3, m = -3$ as a function of proper time of the fiducial node for $\tilde{R}_p = [9.5, 10, 10.5]$.

CHAPTER

8

CONCLUSIONS

In this chapter, we summarize the work in this thesis and describe future work.

8.1 Summary

In this thesis, we have presented a numerical framework for modeling solid extended bodies using elasticity theory in general relativity. We make the simplifying assumption that the metric is not affected by the SEM tensor of the extended body. The numerical method described can be used to model solid bodies of any shape, for any hyperelastic potential energy models and any spacetime metric. We have focused mainly on the free boundary condition and have not investigated further on the difficulty of implementing other boundary conditions within the numerical framework described. We have also described a method using Fermi frames to extract information from the simulations. Moreover, we outlined a procedure to decompose the deformation of a spherical elastic body into the normal modes.

We used the framework developed to model the motion of a $0.1 M$ radius solid sphere in close encounter orbits around a Schwarzschild black hole. We constructed initial data

so that the sphere is initially in quasistatic equilibrium with the local $\ell = 2$ tidal field. This ensured that the sphere does not immediately oscillate at the start of the simulation. We were also careful to ensure that the sphere is initially non-spinning.

We used several Fermi frames to compute an approximate center of mass and the conserved quantities of the body and to visualize its deformation. The total energy and angular momentum computed in the Fermi frame, which are theoretically conserved for Schwarzschild spacetime, displayed numerical conservation of 9 orders of magnitude for the total energy at the end of the simulation and 7 orders of magnitude for the total angular momentum for the next to highest mesh refinement. This validates the numerical simulation in curved spacetime. We obtained the amount the center of mass of the body deviates from a geodesic that starts with the same initial conditions as the center of mass. We also evaluated the increase in spin of the sphere at the end of the simulation. We were able to find some terms which had a contribution to the angular momentum due to the second order moments of the SEM tensor. We obtained detailed information on the modes excited in the elastic sphere. We found that there was coupling between the $n = 0, \ell = 2, m = 0$ and $n = 1, \ell = 2, m = \pm 2$ spheroidal modes due to the nonlinear deformation of the sphere.

8.2 Future work

In the future, we plan to use the numerical framework developed to simulate a spheroidal body that is initially spinning. We identified two cases of particular interest. The first case is when the body is slowly spinning but is significantly deformed. This cannot be modeled accurately within the framework of the MPD equations that also include quadrupole terms. The second case is when the body is spinning very fast but has a negligible deformation. In the second case, we are interested in comparing with the MPD equations to pole-dipole order that prescribe the motion of spinning particles in general relativity. Our numerical framework does not need a spin supplementary condition as in the MPD equations and we are interested in figuring out the limitations and validity of the spin supplementary conditions and the MPD equations.

Furthermore, we are interested in modeling the motion of a solid sphere in Kerr spacetime to study the effects of the black hole's spin on the body. We are also interested in analysing carefully the effects of nonlinear deformation and of Coriolis and centrifugal forces on the normal modes excited. Finally, we are interested in cases that can cause torsional modes to be excited.

REFERENCES

- Abbott, B. P. et al. (2017). Gw170817: Observation of gravitational waves from a binary neutron star inspiral. *Phys. Rev. Lett.*, 119:161101.
- Alho, A., Natário, J., Pani, P., and Raposo, G. (2022). Compact elastic objects in general relativity. *Phys. Rev. D*, 105:044025.
- Beig, R. and Schmidt, B. G. (2017). Celestial mechanics of elastic bodies II. *Classical and Quantum Gravity*, 34(8):085001.
- Brown, J. D. (2019). Fermi normal coordinates. unpublished.
- Brown, J. D. (2021). Elasticity theory in general relativity. *Classical and Quantum Gravity*, 38(8):085017.
- Brown, J. D. (n.d.). Elastic body-small oscillations. unpublished.
- Brown, J. D. and Marolf, D. (1996). Relativistic material reference systems. *Phys. Rev. D*, 53:1835–1844.
- Camisassa, María E., Althaus, Leandro G., Córscico, Alejandro H., De Gerónimo, Francisco C., Miller Bertolami, Marcelo M., Novarino, María L., Rohrmann, René D., Wachlin, Felipe C., and García-Berro, Enrique (2019). The evolution of ultra-massive white dwarfs. *A&A*, 625:A87.
- Carter, B. and Quintana, H. (1972). Foundations of general relativistic high-pressure elasticity theory. *Proceedings of the Royal Society of London. Series A, Mathematical and Physical Sciences*, 331(1584):57–83.
- Chamel, N. and Haensel, P. (2008). Physics of neutron star crusts. *Living Reviews in relativity*, 11:1–182.
- Cheng, R. M. and Evans, C. R. (2013). Relativistic effects in the tidal interaction between a white dwarf and a massive black hole in fermi normal coordinates. *Phys. Rev. D*, 87:104010.
- Costa, L. F. O. and Natário, J. (2015). Center of mass, spin supplementary conditions, and the momentum of spinning particles. *Fund. Theor. Phys.*, 179:215–258.
- De, S., Finstad, D., Lattimer, J. M., Brown, D. A., Berger, E., and Biwer, C. M. (2018). Tidal deformabilities and radii of neutron stars from the observation of gw170817. *Phys. Rev. Lett.*, 121:091102.
- DeWitt, B. S. (1962). The quantization of geometry. In *Gravitation: An Introduction to Current Research*. Wiley.

- Dixon, W. G. and Bondi, H. (1970). Dynamics of extended bodies in general relativity. i. momentum and angular momentum. *Proceedings of the Royal Society of London. A. Mathematical and Physical Sciences*, 314(1519):499–527.
- Dixon, W. G. and Hewish, A. (1970). Dynamics of extended bodies in general relativity - ii. moments of the charge-current vector. *Proceedings of the Royal Society of London. A. Mathematical and Physical Sciences*, 319(1539):509–547.
- Dixon, W. G. and Hewish, A. (1974). Dynamics of extended bodies in general relativity iii. equations of motion. *Philosophical Transactions of the Royal Society of London. Series A, Mathematical and Physical Sciences*, 277(1264):59–119.
- Einstein, A. and Grommer, J. (1927). Allgemeine Relativitätstheorie und Bewegungsgesetz. *Sitzungsberichte der Preussischen Akademie der Wissenschaften, Physikalisch-Mathematische Klasse*, 2(13).
- Frankel, T. (2011). *The Geometry of Physics: An Introduction*. Cambridge University Press, 3 edition.
- Gundlach, C., Hawke, I., and Erickson, S. J. (2011). A conservation law formulation of nonlinear elasticity in general relativity. *Classical and Quantum Gravity*, 29.
- Herglotz, G. (1911). Über die mechanik des deformierbaren körpers vom standpunkte der relativitätstheorie. *Annalen der Physik*, 341(13):493–533.
- Hughes, T. (2012). *The Finite Element Method: Linear Static and Dynamic Finite Element Analysis*. Dover Civil and Mechanical Engineering. Dover Publications.
- Ishii, M., Shibata, M., and Mino, Y. (2005). Black hole tidal problem in the fermi normal coordinates. *Phys. Rev. D*, 71:044017.
- Karlovini, M. and Samuelsson, L. (2003). Elastic stars in general relativity: I. foundations and equilibrium models. *Classical and Quantum Gravity*, 20(16):3613.
- Karlovini, M. and Samuelsson, L. (2004). Elastic stars in general relativity: Iii. stiff ultrarigid exact solutions. *Classical and Quantum Gravity*, 21(19):4531.
- Karlovini, M. and Samuelsson, L. (2007). Elastic stars in general relativity: Iv. axial perturbations. *Classical and Quantum Gravity*, 24(13):3171.
- Karlovini, M., Samuelsson, L., and Zarroug, M. (2004). Elastic stars in general relativity: Ii. radial perturbations. *Classical and Quantum Gravity*, 21(6):1559.
- Karypis, G. and Kumar, V. (1997). Metis—a software package for partitioning unstructured graphs, partitioning meshes and computing fill-reducing ordering of sparse matrices.
- Kijowski, J. and Magli, G. (1992). Relativistic elastomechanics as a lagrangian field theory. *Journal of Geometry and Physics*, 9(3):207–223.

- Kyrian, K. and Semerák, O. (2007). Spinning test particles in a Kerr field – II. *Monthly Notices of the Royal Astronomical Society*, 382(4):1922–1932.
- Lamb, H. S. (1881). On the vibrations of an elastic sphere. *Proceedings of The London Mathematical Society*, pages 189–212.
- Lanczos, C. (1949). *The Variational Principles of Mechanics*. Heritage Series. University of Toronto Press.
- Landau, L. and Lifshitz, E. (1951). *The Classical Theory of Fields*. Pergamon, Oxford.
- Love, A. (1892). *A Treatise on the Mathematical Theory of Elasticity*. Number v. 1 in A Treatise on the Mathematical Theory of Elasticity. University Press.
- Madore, J. (1969). The equations of motion of an extended body in general relativity. *Annales de l'institut Henri Poincaré. Section A, Physique Théorique*, 11(2):221–237.
- Manasse, F. K. and Misner, C. W. (1963). Fermi Normal Coordinates and Some Basic Concepts in Differential Geometry. *Journal of Mathematical Physics*, 4(6):735–745.
- Marsden, J. and Hughes, T. (1994). *Mathematical Foundations of Elasticity*. Dover Civil and Mechanical Engineering Series. Dover.
- Mathisson, M. (1937). Neue mechanik materieller systemes. *Acta Phys. Polon.*, 6:163–200.
- Misner, C., Thorne, K., and Wheeler, J. (1973). *Gravitation*. W. H. Freeman.
- Papapetrou, A. (1951). Spinning test-particles in general relativity. i. *Proceedings of the Royal Society of London. Series A, Mathematical and Physical Sciences*, 209(1097):248–258.
- Pirani, F. A. (1956). On the physical significance of the riemann tensor. *Acta Physica Polonica*, 15:389–405.
- Press, W. H. and Teukolsky, S. A. (1977). On formation of close binaries by two-body tidal capture. *Astrophysical Journal*, 213:183–192.
- Steinhoff, J. and Puetzfeld, D. (2012). Influence of internal structure on the motion of test bodies in extreme mass ratio situations. *Phys. Rev. D*, 86:044033.
- Synge, J. (1960). *Relativity: The General Theory*. Number v. 1 in North-Holland series in physics. North-Holland Publishing Company.
- The MathWorks Inc. (2021). Partial Differential Equation Toolbox.
- Thorne, K. and Blandford, R. (2017). *Modern Classical Physics: Optics, Fluids, Plasmas, Elasticity, Relativity, and Statistical Physics*. Princeton University Press.
- Tulczyjew, W. (1959). Motion of multipole particles in general relativity theory. *Acta Phys. Pol*, 18(393):94.

Witzany, V., Steinhoff, J., and Lukes-Gerakopoulos, G. (2019). Hamiltonians and canonical coordinates for spinning particles in curved space-time. *Classical and Quantum Gravity*, 36(7):075003.